A&A 571, A6 (2014)
DOI: 10.1051/0004-6361/201321570

Astronomy & Astrophysics
Special feature

Planck 2013 results

Planck 2013 results. VI. High Frequency Instrument data processing

Planck Collaboration: P. A. R. Ade[86], N. Aghanim[59], C. Armitage-Caplan[90], M. Arnaud[73], M. Ashdown[70,6], F. Atrio-Barandela[19], J. Aumont[59], C. Baccigalupi[85], A. J. Banday[93,10], R. B. Barreiro[67], E. Battaner[95], K. Benabed[60,92], A. Benoît[57], A. Benoit-Lévy[25,60,92], J.-P. Bernard[93,10], M. Bersanelli[35,50], P. Bielewicz[93,10,85], J. Bobin[73], J. J. Bock[68,11], J. R. Bond[9], J. Borrill[14,87], F. R. Bouchet[60,92,⋆], F. Boulanger[59], J. W. Bowyer[55], M. Bridges[70,6,64], M. Bucher[1], C. Burigana[49,33], J.-F. Cardoso[74,1,60], A. Catalano[75,72], A. Chamballu[73,16,59], R.-R. Chary[56], X. Chen[56], H. C. Chiang[28,7], L.-Y Chiang[63], P. R. Christensen[81,38], S. Church[89], D. L. Clements[55], S. Colombi[60,92], L. P. L. Colombo[24,68], C. Combet[75], F. Couchot[71], A. Coulais[72], B. P. Crill[68,82], A. Curto[6,67], F. Cuttaia[49], L. Danese[85], R. D. Davies[69], R. J. Davis[69], P. de Bernardis[34], A. de Rosa[49], G. de Zotti[45,85], J. Delabrouille[1], J.-M. Delouis[60,92], F.-X. Désert[53], C. Dickinson[69], J. M. Diego[67], H. Dole[59,58], S. Donzelli[50], O. Doré[68,11], M. Douspis[59], J. Dunkley[90], X. Dupac[41], G. Efstathiou[64], T. A. Enßlin[78], H. K. Eriksen[65], F. Finelli[49,51], O. Forni[93,10], M. Frailis[47], A. A. Fraisse[28], E. Franceschi[49], S. Galeotta[47], K. Ganga[1], M. Giard[93,10], G. Giardino[42], D. Girard[75], Y. Giraud-Héraud[1], J. González-Nuevo[67,85], K. M. Górski[68,96], S. Gratton[70,64], A. Gregorio[36,47], A. Gruppuso[49], J. E. Gudmundsson[28], F. K. Hansen[65], D. Hanson[79,68,9], D. Harrison[64,70], G. Helou[11], S. Henrot-Versillé[71], O. Herent[60], C. Hernández-Monteagudo[13,78], D. Herranz[67], S. R. Hildebrandt[11], E. Hivon[60,92], M. Hobson[6], W. A. Holmes[68], A. Hornstrup[17], Z. Hou[29], W. Hovest[78], K. M. Huffenberger[26], G. Hurier[59,75], A. H. Jaffe[55], T. R. Jaffe[93,10], W. C. Jones[28], M. Juvela[27], E. Keihänen[27], R. Keskitalo[22,14], T. S. Kisner[77], R. Kneissl[40,8], J. Knoche[78], L. Knox[29], M. Kunz[18,59,3], H. Kurki-Suonio[27,43], G. Lagache[59], J.-M. Lamarre[72], A. Lasenby[6,70], R. J. Laureijs[42], C. R. Lawrence[68], M. Le Jeune[1], R. Leonardi[41], C. Leroy[59,93,10], J. Lesgourgues[91,84], M. Liguori[32], P. B. Lilje[65], M. Linden-Vørnle[17], M. López-Caniego[67], P. M. Lubin[30], J. F. Macías-Pérez[75], C. J. MacTavish[70], B. Maffei[69], N. Mandolesi[49,5,33], M. Maris[47], F. Marleau[62], D. J. Marshall[73], P. G. Martin[9], E. Martínez-González[67], S. Masi[34], M. Massardi[48], S. Matarrese[32], F. Matthai[78], P. Mazzotta[37], P. McGehee[56], P. R. Meinhold[30], A. Melchiorri[34,52], F. Melot[75], L. Mendes[41], A. Mennella[35,50], M. Migliaccio[64,70], S. Mitra[54,68], M.-A. Miville-Deschênes[59,9], A. Moneti[60], L. Montier[93,10], G. Morgante[49], D. Mortlock[55], S. Mottet[60], D. Munshi[86], J. A. Murphy[80], P. Naselsky[81,38], F. Nati[34], P. Natoli[33,4,49], C. B. Netterfield[20], H. U. Nørgaard-Nielsen[17], C. North[86], F. Noviello[69], D. Novikov[55], I. Novikov[81], F. Orieux[60], S. Osborne[89], C. A. Oxborrow[17], F. Paci[85], L. Pagano[34,52], F. Pajot[59], R. Paladini[56], D. Paoletti[49,51], F. Pasian[47], G. Patanchon[1], O. Perdereau[71], L. Perotto[75], F. Perrotta[85], F. Piacentini[34], M. Piat[1], E. Pierpaoli[24], D. Pietrobon[68], S. Plaszczynski[71], E. Pointecouteau[93,10], G. Polenta[4,46], N. Ponthieu[59,53], L. Popa[61], T. Poutanen[43,27,2], G. W. Pratt[73], G. Prézeau[11,68], S. Prunet[60,92], J.-L. Puget[59], J. P. Rachen[21,78], B. Racine[1], W. T. Reach[94], R. Rebolo[66,15,39], M. Reinecke[78], M. Remazeilles[69,59,1], C. Renault[75], S. Ricciardi[49], T. Riller[78], I. Ristorcelli[93,10], G. Rocha[68,11], C. Rosset[1], G. Roudier[1,72,68], M. Rowan-Robinson[55], B. Rusholme[56], L. Sanselme[75], D. Santos[75], A. Sauvé[93,10], G. Savini[83], D. Scott[23], E. P. S. Shellard[12], L. D. Spencer[86], J.-L. Starck[73], V. Stolyarov[6,70,88], R. Stompor[1], R. Sudiwala[86], F. Sureau[73], D. Sutton[64,70], A.-S. Suur-Uski[27,43], J.-F. Sygnet[60], J. A. Tauber[42], D. Tavagnacco[47,36], S. Techene[60], L. Terenzi[49], M. Tomasi[50], M. Tristram[71], M. Tucci[18,71], G. Umana[44], L. Valenziano[49], J. Valiviita[43,27,65], B. Van Tent[76], L. Vibert[59], P. Vielva[67], F. Villa[49], N. Vittorio[37], L. A. Wade[68], B. D. Wandelt[60,92,31], S. D. M. White[78], D. Yvon[16], A. Zacchei[47], and A. Zonca[30]

(Affiliations can be found after the references)

Received 26 March 2013 / Accepted 22 July 2014

ABSTRACT

We describe the processing of the 531 billion raw data samples from the High Frequency Instrument (HFI), which we performed to produce six temperature maps from the first 473 days of *Planck*-HFI survey data. These maps provide an accurate rendition of the sky emission at 100, 143, 217, 353, 545, and 857 GHz with an angular resolution ranging from 9.′7 to 4.′6. The detector noise per (effective) beam solid angle is respectively, 10, 6 , 12, and 39 μK in the four lowest HFI frequency channels (100−353 GHz) and 13 and 14 kJy sr^{-1} in the 545 and 857 GHz channels. Relative to the 143 GHz channel, these two high frequency channels are calibrated to within 5% and the 353 GHz channel to the percent level. The 100 and 217 GHz channels, which together with the 143 GHz channel determine the high-multipole part of the CMB power spectrum ($50 < \ell < 2500$), are calibrated relative to 143 GHz to better than 0.2%.

Key words. methods: data analysis – cosmic background radiation – cosmology: observations – surveys

1. Introduction

This paper, one of a set associated with the 2013 release of data from the *Planck*[1] mission (Planck Collaboration I 2014–Planck Collaboration XXXI 2014), describes the processing of data from the *Planck* High Frequency Instrument (HFI) to produce calibrated and characterized maps. HFI (Lamarre et al. 2010; Planck HFI Core Team 2011a) observes in the 100, 143, 217, 353, 545, and 857 GHz bands with bolometers cooled to 0.1 K. The HFI instrument comprises 50 signal bolometers, as

⋆ Corresponding author: F. R. Bouchet, e-mail: bouchet@iap.fr

[1] *Planck* (http://www.esa.int/Planck) is a project of the European Space Agency (ESA) with instruments provided by two scientific consortia funded by ESA member states (in particular the lead countries France and Italy), with contributions from NASA (USA) and telescope reflectors provided by a collaboration between ESA and a scientific consortium led and funded by Denmark.

well as two dark bolometers, 16 thermometers, a resistor, and a capacitor used for monitoring and housekeeping. The count of 50 bolometers includes 12 polarization sensitive bolometer (PSB) pairs, four each at 100−353 GHz; the rest are unpolarized spider-web bolometers (SWBs). We describe the steps taken by the HFI data processing centre (DPC) to transform the packets sent by the satellite into sky maps at HFI frequencies, with the help of ancillary data, for example, from ground calibration. These are temperature maps alone, as obtained from the beginning of the first light survey on 13 August 2009, to the end of the nominal mission on 27 November 2010.

Planck defines a sky survey as the time over which the spin axis rotates by 180°, a period close to six months in duration in which about 95% of the sky is covered at each frequency. During routine operations, *Planck* scans the sky by spinning in circles with an angular radius of roughly 85°. The spin axis follows a cycloidal path on the sky by periodic step-wise displacements of 2′, resulting in typically 40 (35 to 70) circles of typical duration 46 minutes, constituting a *stable pointing period* between repointings. The scanning strategy is discussed in more detail in Tauber et al. (2010), Planck Collaboration I (2011), and Planck Collaboration I (2014). The 15.5 months of nominal mission survey data then provide 2.5 sky surveys, and maps are provided for the first two sky surveys separately, as well as for the complete nominal mission. As a means to estimate aspects of the noise distribution, we also deliver "half-ring" maps made out of the first and second half of each stable pointing period. Maps are produced for individual detectors, as well as for averages over each band and for selected detector sets defined within each band (see Table 1).

The next section provides an overview of HFI data processing. Section 3 is devoted to the processing of time-ordered information (TOI) from individual detectors to produce cleaned timelines. These timelines are used to estimate the temporal noise properties in Sect. 3.10 and to determine the detector pointings and beams in Sects. 4 and 5. Section 6 discusses the creation of maps and their photometric calibration, while Sect. 7 presents tests applied to assess the consistency and accuracy of the products. For completeness, component separation and further processing are briefly described in Sect. 7.5. Section 8 concludes with a summary of the characteristics of the HFI data delivered, as currently processed.

Some of the specific processing steps for HFI data are described more fully elsewhere: Planck Collaboration VII (2014) discusses the transfer function and beams; Planck Collaboration VIII (2014) the calibration of HFI detectors; Planck Collaboration IX (2014) the determination of the spectral bands for each detector and their combination; and Planck Collaboration X (2014) the effect of so-called "glitches" such as cosmic-ray hits on the detectors. The processing of data from the Low Frequency Instrument (LFI) is discussed in Planck Collaboration II (2014). Technical details of specific data products are discussed in Planck Collaboration (2013). We have applied to the delivered data products many consistency and validation tests to assess their quality (see in particular Planck Collaboration IX 2014; Planck Collaboration XII 2014; Planck Collaboration XV 2014; Planck Collaboration XVI 2014). While the products meet a very high standard, as described here, we did find limitations. Their mitigation, and related data products, are left to future releases. In particular, HFI analysis revealed that nonlinear effects in the on-board analogue-to-digital converters (ADC) modified the recovered bolometer signal. In situ observations over 2012−2013 are measuring this effect, and algorithms have been developed to explicitly account for it in the data analysis. However, the first-order effect of the ADC nonlinearity mimics a gain variation in the bolometers, which the current release measures and removes as part of the calibration procedures. This is discussed further in Sects. 6.2 and 7.2.1.

The mapmaking procedure uses the full intensity and polarization information from the HFI bolometers. The current analysis cannot guarantee that the large-scale polarization signal is free from systematic effects. However, the preliminary analysis shows that the small-scale maps have the expected CMB content at high signal-to-noise, as discussed in Sect. 6.7 below, and in Planck Collaboration I (2014) and Planck Collaboration XVI (2014). Although we do not use these maps for cosmological measurements, future work will use them for investigations of the properties of polarized emission of the Galaxy.

Finally, since the March 2013 data release, we have found strong evidence that the $\ell \simeq 1800$ dip in some 217 GHz detector cross-spectra is stronger in the first six-month survey than in subsequent surveys and that its amplitude may be reduced by additional data flagging targeting electromagnetic interference from the ^{4}He-JT (hereafter 4 K) cooler drive and read-out electronics (see Sect. 3.6). This dip is therefore likely to be a (small) residual systematic effect in the data, which we show has little impact on cosmological parameter determination (Planck Collaboration XV 2014; Planck Collaboration XVI 2014), but which contributes to the weak detection of a feature in the power spectrum reconstruction done in Planck Collaboration XXII (2014).

2. HFI data processing overview

The processing of HFI data proceeds according to a series of levels, shown schematically in Fig. 1. Level 1 (L1) creates a database of the raw satellite data as a function of time (TOI objects). The full set of TOI comprises the signals from each HFI bolometer, ancillary information (e.g., pointing data), and associated housekeeping data (e.g., temperature monitors). Level 2 (L2), the subject of this paper, uses these data to build a model of the HFI instrument, the Instrument Model (IMO), produces cleaned, calibrated timelines for each detector, and combines these into aggregate products such as maps at each frequency. Level 3 (L3) takes these instrument-specific results and derives various products: component-separation algorithms transform the maps at each frequency into maps of separate astrophysical components; source detection algorithms create catalogues of Galactic and extragalactic objects; finally, a likelihood code assesses the match between a cosmological and astrophysical model and the frequency maps.

Of course, these processing steps are not done completely sequentially: HFI data are processed iteratively. In many ways, the IMO is the main internal data product from *Planck*, and the main task of the HFI DPC is its iterative updating. Early versions of the IMO were derived from pre-launch data, and from the first-light survey of the last two weeks of August 2009. Further revisions of the IMO, and of the pipelines themselves, were derived after the completion of successive passes through the data. These new versions included expanded information about the HFI instrument: for example, the initial IMO contained only coarse information about the shape of the detector angular response (i.e., the full-width at half-maximum of an approximating Gaussian); subsequent revisions included full measured harmonic-space window functions.

In somewhat more detail, L1 software fills the database and updates, daily, the various TOI objects. Satellite attitude data, sampled at 8 Hz during science data acquisition and at 4 Hz

Table 1. Detector sets ("ds") used in this data release.

Set name	Frequency [GHz]	Type	Detectors in the set	Weights in the set	Products
100-ds0	100	MIX	All 8 detectors	0.33, 0.44, 1.50, 0.76 2.08, 1.40, 0.97, 0.52	N, B, F, H, S1, S2, HR1, HR2 Z-N, Z-S1, Z-S2
100-ds1	100	PSB	1a+1b + 4a+4b	0.58, 0.78, 1.71, 0.93	C
100-ds2	100	PSB	2a+2b + 3a+3b	1.05, 0.53, 1.45, 0.98	C
143-ds0	143	MIX	11 detectors	1.04, 0.44, 1.06, 0.93, 0.88, 0.94 0.80, 0.66, 1.32, 1.27, 1.66	N, B, F, H, S1, S2, HR1, HR2 Z-N, Z-S1, Z-S2
143-ds1	143	PSB	1a+1b + 3a+3b	1.26, 0.53, 1.06, 1.15	C
143-ds2	143	PSB	2a+2b + 4a+4b	1.23, 1.08, 0.92, 0.76	C
143-ds3	143	SWB	143-5		C
143-ds4	143	SWB	143-6		C
143-ds5	143	SWB	143-7		C
217-ds0	217	MIX	All 12 detectors	1.54, 1.44, 1.62, 1.83, 0.60, 0.77 0.62, 0.67, 0.81, 0.85, 0.64, 0.59	N, B, F, H, S1, S2, HR1, HR2 Z-N, Z-S1, Z-S2
217-ds1	217	PSB	5a+5b + 7a+7b	0.79, 1.02, 1.07, 1.12	C
217-ds2	217	PSB	6a+6b + 8a+8b	0.98, 1.06, 1.01, 0.94	C
217-ds3	217	SWB	217-1		C
217-ds4	217	SWB	217-2		C
217-ds5	217	SWB	217-3		C
217-ds6	217	SWB	217-4		C
353-ds0	353	MIX	All 12 detectors	2.45, 2.38, 0.44, 0.65, 0.61, 0.57 0.64, 0.64, 0.31, 0.34, 1.62, 1.35	N, B, F, H, S1, S2, HR1, HR2 Z-N, Z-S1, Z-S2
353-ds1	353	PSB	3a+3b + 5a+5b	0.75, 1.09, 1.09, 1.07	
353-ds2	353	PSB	4a+4b + 6a+6b	1.33, 1.25, 0.68, 0.73	
353-ds3	353	SWB	353-1		
353-ds4	353	SWB	353-2		
353-ds5	353	SWB	353-7		
353-ds6	353	SWB	353-8		
545-ds0	545	SWB	3 detectors (1, 2, 4)	0.94, 1.10, 0.96	N, B, F, H, S1, S2, HR1, HR2 Z-N, Z-S1, Z-S2
857-ds0	857	SWB	All 4 detectors	1.14, 1.11, 1.15, 0.60	N, B, F, H, S1, S2, HR1, HR2 Z-N, Z-S1, Z-S2

Notes. Unpolarized SWBs are used alone, while PSBs (with individual bolometers denoted "a" and "b") are used by pair; "MIX" denotes a combination of detector types. Here we consider only the temperature map extracted from the analysis of four bolometers (two pairs of PSBs). The weights indicate the relative weighting used in producing maps out of the TOI of several detectors. The relative weights in a set are given in the numerical order of each detector (e.g., 1a, 1b, 2a, 2b, 3a, 3b, ... for the 100-ds0 set). The last column details the specific products created for each set. "B": beam information; "C": detector-set spectra, corrected for the beam transfer function, for the detector sets used in the high-ℓ likelihood; "F": frequency band information; "H": pixel hit-count maps; "HR1", "HR2": maps made from the first or second half of each ring; "N": nominal mission maps; "S1", "S2": survey maps generated from the data collected during the first six months or the next six months; and "Z": ZLE/FSL-corrected maps.

otherwise, are resampled by interpolation to the 180.37370 Hz (hereafter 180.4 Hz) acquisition frequency of the detectors, corresponding to the integration time for a single data sample; further information on L1 steps was given in Planck HFI Core Team (2011b). Raw timelines and housekeeping data are then processed by L2 to compensate for the instrumental response and to remove estimates of known artefacts. The various steps in TOI processing are discussed in Sect. 3. First, the raw timeline voltages are demodulated, deglitched, and corrected for the bolometer nonlinearity and for temperature fluctuations of the environment using correlations with the signal TOI from the two dark bolometers that serve as bolometer plate temperature monitors. Narrow lines in the TOI frequency spectra caused by the ^{4}He-JT (4 K) cooler are also removed before deconvolving the temporal response of the instrument. Finally, various flags are set to mark unusable samples.

Further use of the data requires knowledge of the pointing for individual detectors, as discussed in Sect. 4. During a single *stable pointing period*, *Planck* spins around an axis pointing towards a fixed direction on the sky (up to an accounted-for wobbling), repeatedly scanning approximately the same circle (Planck Collaboration I 2014). The satellite is re-pointed so that the spin axis follows the Sun, and the observed circle sweeps through the sky at approximately one degree per day. Assuming a focal plane geometry, i.e., a set of relations between the satellite pointing and that of each of the detectors, we build *rings* of data derived by analysing the data acquired by a detector during each stable pointing period ("ring" refers to the data obtained during a single stable pointing period). This redundancy permits averaging of the data on rings to reduce instrument noise. The resulting estimate of the sky signal can then be subtracted from the timeline to estimate the temporal noise power spectral density, a useful characterization of the detector data after TOI processing. This noise may be described as a white noise component, dominating at intermediate temporal frequencies, plus additional low- and high-frequency noise. The effect on maps

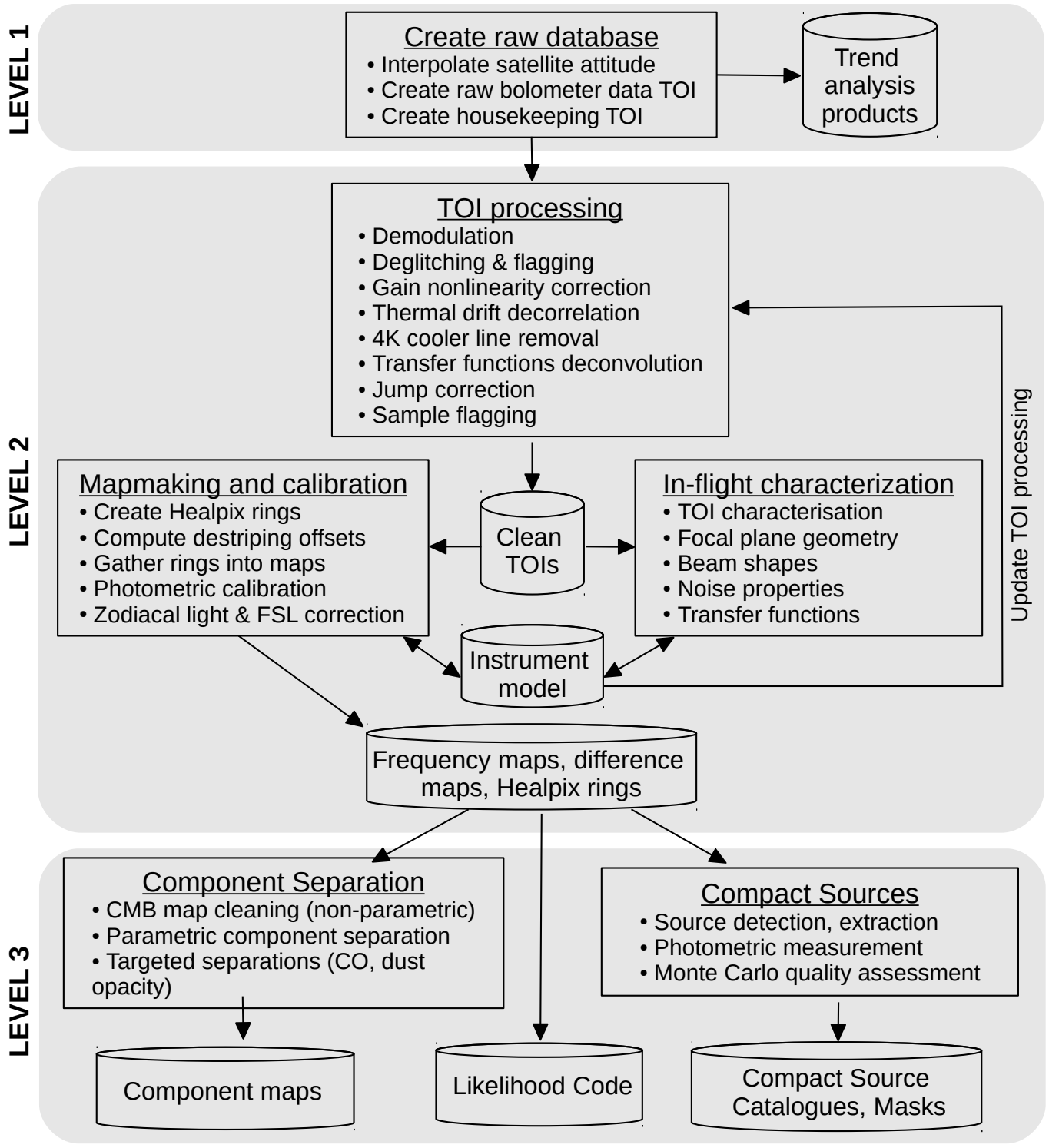

Fig. 1. Overview of the data flow and main functional tasks of the HFI Data Processing Centre. Level 1 creates a database of the raw satellite data as a function of time. Level 2 builds a data model and produces sky maps at the six frequency of the instrument. This flow diagram illustrates the crucial role of the Instrument Model (IMO), which is both an input and an output of many tasks, and is updated iteratively during successive passes of the data. Level 3 takes these instrument-specific products and derives final astrophysical products. This paper is mostly concerned with Level 2 processing and its validation.

of the low-frequency part of the noise can be partially mitigated by determining an offset for each ring. These so-called "destriping" offsets are obtained by requiring that the difference between intersecting rings be minimized. Once the offsets are removed from each ring, the rings are co-added to produce sky maps.

As explained in Sect. 6, a complication arises from the fact that the detector data include both the contribution from the *solar* dipole induced by the motion of the Solar System through the CMB (sometimes referred to as the "cosmological" dipole), and the *orbital* dipole induced by the motion of the satellite within

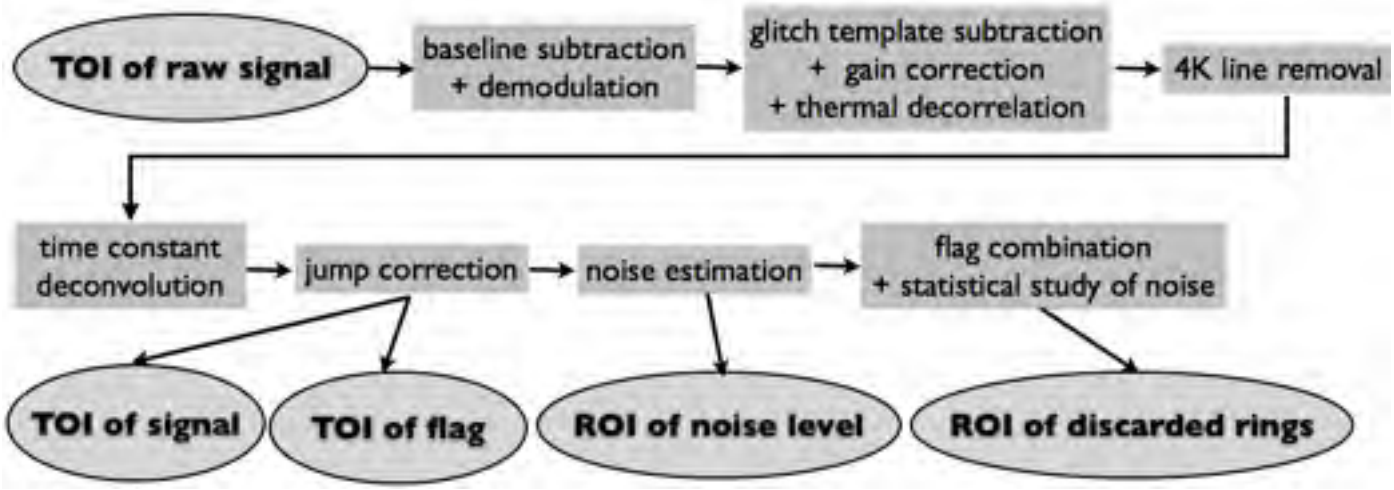

Fig. 2. Main TOI processing steps. Pipeline modules are represented as filled squares. TOI: time ordered information. ROI: ring ordered information (i.e., one piece of information per stable pointing period). Ring: data obtained during a stable pointing period (typically 40 satellite revolutions of one minute each).

the Solar System, which is not constant on the sky and must therefore be removed from the rings before creating the sky map. The solar dipole is used as a calibration source at lower HFI frequencies, and bright planet fluxes at higher frequencies. Since we need this calibration to remove the orbital dipole contribution to create the maps themselves, the maps and their calibrations are obtained iteratively. The dipoles are computed in the non-relativistic approximation. The resulting calibration coefficients are also stored in the IMO, which can then be used, for instance, to express noise spectra in noise-equivalent temperature (NET) units. The destriping offsets, once obtained through a global solution, are also used to create local maps around planets. As described in Sect. 4 these are used to improve our knowledge of the focal plane geometry stored in the previous version of the IMO and to improve measurements of the "scanning" beam (defined as the response to a point source of the full optical and electronic system, *after* the filtering done during the TOI processing step, described in Sect. 5).

The ring and mapmaking stages allow us to generate many different maps, e.g., using different sets of detectors, the first or second halves of the data in each ring, or data from different sky surveys. Null tests using difference maps of the same sky area observed at different times, in particular, have proved extremely useful in characterizing the map residuals, described in Sect. 7.

3. TOI processing

In the L1 stage of processing (previously described in Sect. 3 of Planck HFI Core Team 2011b), the raw telemetry TOI are unfolded into one time series for each bolometer. The signal is regularly sampled at 180.4 Hz. We denote as *TOI processing* the transformation of the TOI coming from L1 into clean TOI objects, which can be used for mapmaking after focal plane geometry reconstruction and photometric calibration have been performed. The general philosophy of the TOI processing is to modify the timelines as little as possible, and therefore to flag regions contaminated by systematic effects (e.g., cosmic-ray glitches). We deal with each bolometer signal separately. Aside from allowing the possible flagging of known bright sources, the only pointing information that is used in the main TOI processing is the phase (see Sect. 3.3), so the TOI processing assumes perfect redundancy of the data within a given pointing period. The output of TOI processing is not only a set of clean TOI but also accompanying qualifying flags and trend parameters used internally for detailed statistics. Moreover, all data samples are processed, although only clean samples will be projected on maps. For beam measurement (see Sect. 5), specific processing is performed on pointing periods that are close to Mars, Jupiter or Saturn (see Sect. 3.11).

A flow diagram is shown in Fig. 2, illustrating the TOI processing steps detailed in the following subsections. Section 4 of Planck HFI Core Team (2011b) presents the early version of the TOI processing. The pipeline has changed sufficiently since then to warrant a self-contained global description of the TOI processing. We refer the reader to Planck Collaboration (2013) and the various companion papers mentioned above for more details. The changes mostly reflect the improvement in performance and in our understanding of the underlying effects. The TOI are not delivered in the present data release, but their processing is an essential, though hidden, ingredient in the delivered maps. Some of the systematic effects arising in the map analysis can only be understood by referring to the bolometer timeline behaviour and processing.

It was recently realised that some apparent gain variations, spotted comparing identical pointing circles one-year apart, actually originate in nonlinearities in the bolometer readout system ADCs. Note that the ADC nonlinearity is not explicitly corrected for in the TOI processing, but rather as an equivalent gain variation at the mapmaking level (see Sect. 6.2 and Sect. 7.2.1).

3.1. Input flags

Strong signal gradients can adversely affect some stages of TOI processing. We flag the data expected to have strong gradients using only the pointing information, exclusively in the intermediate stages and not for mapmaking. We also flag data where the pointing is known to be unstable. Input flags come from the following.

1. A *point-source* flag. This is based on the locations of sources in the *Planck* Early Release Compact Source Catalog (ERCSC; see Planck Collaboration VII 2011). A mask map is generated around each of them from which flag TOI objects are created using the pointing information.

2. A *Galactic* flag. This is based on *IRAS* maps with a threshold that depends on the frequency.
3. A *BigPlanet* flag. Any sample that falls within a given distance of Mars, Jupiter, or Saturn is flagged.
4. An *Unstable pointing* flag (see Sect. 4). This accounts for depointings between stable pointing periods and other losses of pointing integrity.

Flagged data are either processed separately or ignored, depending on the specific analysis. The flags are described in more detail in Planck Collaboration (2013).

3.2. Demodulation

The bolometers are AC square-wave modulated to put the acquisition electronics $1/f$ noise at high temporal frequencies (Lamarre et al. 2010). The modulation frequency is $f_{\rm mod} = f_{\rm acq}/2 = 90.18685$ Hz. A demodulation step is done as follows. First a one-hour running average of the modulated timeline is computed, known as the AC offset baseline. This is carried out by excluding data that are masked due to glitches (see below) or by the Galactic flag (see above). Once the AC offset baseline is subtracted from the raw timeline, a simple $(+,-)$ demodulation is applied. The overall sign of the signal is set to obtain a positive signal on point sources and Galaxy crossings. This AC offset baseline removal is needed in order to correct for the slow drift of the zero level of the electronics. Any possible drift of the baseline on a timescale smaller than one hour is dealt with at the filtering stage (see below). The baseline varies very smoothly over the mission and fluctuates by less than ten minimum resolution units from the middle of the range of 65 536 values allowed by the on-board ADC, discussed in greater detail in Sect. 7.2.1.

3.3. Deglitching and gap-filling

The timelines are affected by obvious "glitches" (cosmic ray hits and other large excursions) at a rate of about one per second. This generates a huge Poisson noise if not dealt with. Such glitches are detected as a large positive signal followed by a roughly exponential tail. There are three basic classes of glitches affecting bolometers. The statistical and physical understanding of the different populations is given by Planck HFI Core Team (2011b), and revised and expanded by Planck Collaboration X (2014). Here we present the general algorithm.

The type of TOI used in the deglitching is slightly different from the one used in the main processing described in the following sections. Before deglitching, the timeline is demodulated and digitally filtered with a three-point (0.25, 0.5, 0.25) moving kernel. Linear interpolation is performed on those parts of the timeline when the bolometer pointing nears Mars, Jupiter or Saturn, as determined by the *BigPlanet* flag (see Sect. 3.1). This step is done to treat the pointing periods containing a planet crossing whose large gradients would otherwise be confused with glitches.

The algorithm also requires an estimate of the sky signal in order to assess the magnitude of excursions about the mean. It relies on the fact that the signal component of the timeline is periodic within a stable pointing period (up to the slight wobbling of the satellite spin axis). We construct a phase-binned ring (PBR), a useful estimate of the sky signal obtained by averaging the unflagged TOI samples in bins of constant satellite rotation phase. The phase of a sample is given by the pointing reconstruction pipeline and varies continuously from 0 to 2π for each scan circle (about one minute). The bin size is about the width of a single sample, i.e., 1.′7, and the definition of the zero of the phase is irrelevant.

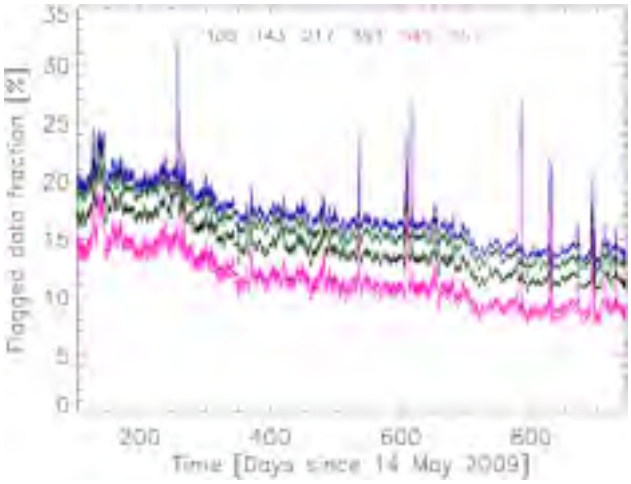

Fig. 3. Evolution of the fraction of the flagged data per bolometer averaged over a channel for the six HFI channels. A running average over 31 pointing periods (approximately a day) is shown. The general decrease of the fraction of flagged data comes from the increase in the solar activity and the correlated decrease of the cosmic ray flux. The sharp peaks are due to solar flares.

The algorithm treats each pointing period separately and one bolometer at a time. The localization of glitches is performed with a sigma-clipping method applied to the sky-subtracted TOI. A template fitting method is used to identify the type of each glitch. After masking and subtracting the series of fitted glitches from the original timeline, the PBR is then recomputed as the average of unflagged samples. Several iterations (generally six) are performed until the variation of χ^2 becomes negligible. The spike part of each glitch is flagged and the exponential tail, below the 3.3σ level, is subtracted using the last iteration of the glitch template fitting process.

Most of the samples flagged by this process are due to cosmic ray hits. Figure 3 shows the mean evolution per channel of the fraction of flagged samples over the full mission. More glitch statistics are given in Planck Collaboration X (2014) and Planck Collaboration (2013).

All gaps due to flagged samples within a ring of data are replaced with an estimate of the signal given by the PBR. For samples around planets, we fill the timeline with the values read from a frequency map (made by excluding planets) from a previous iteration of the data processing at the corresponding pointing coordinates.

3.4. Bolometer nonlinearity correction

If the environment of a bolometer changes, its response will change accordingly. The extreme thermal stability of *Planck* is shown by the measured total power level, which is seen as almost constant (see the next paragraph). Nevertheless, the timelines must be corrected to account for the slightly varying power absorbed by the bolometer coming from the sky load and 100 mK bolometer plate temperature fluctuations. For that purpose, the voltage-to-power conversion step is assumed to be a simple second-order polynomial applied to the timeline:

$$P = \frac{v}{S_0}\left(1 + \frac{v}{v_0}\right), \quad (1)$$

where v is the out-of-balance demodulated voltage (i.e., the voltage difference between the square-wave compensating input voltage and the total bolometer voltage), and S_0 is the responsivity (typically of order 10^9 V W^{-1}) for the fiducial $v = 0$ voltage. It is measured on ground-based I-V curves, but its exact value is unimportant as it is calibrated out. The parameter v_0 is determined for each bolometer from measurements made during the calibration and performance verification (CPV) phase. In general the v_0 values (5 to 200 mV) are equal to or larger than expected using a static bolometer model. The main reason is that a TOI sample is an average of 40 on-board measurements (half a modulation period), which includes an electronic transient (Catalano et al. 2010). The non-linearity correction, as measured by v/v_0 in Eq. (1), is static and accurate for a slowly varying signal, in particular for dipole calibration. The term v/v_0 is at most 10^{-3}, the effect being largest in the 100 GHz band.

During the mission, the drift of the zero level (as measured by v/S_0) is at most roughly 7 fW for bolometers up to the 353 GHz channels, and 50 fW for the 545 and 857 GHz channels, such that the nonlinearity correction implies a drift in the gain of typically 10^{-3} at most, for all detectors. The correction has a relative precision better than 10%, so that the gain uncertainty is at the 10^{-4} level. The effective gain and uncertainty is, however, further affected by the offset in the ADC electronics, discussed in Sect. 7.2.1**.** The dynamical bolometer nonlinearity on very strong sources (Jupiter and the Galactic centre) is not corrected in the nominal TOI.

In addition, there are limits associated with the saturation of the ADC. As discussed in Planck Collaboration (2013), Jupiter and the Galactic centre are the only signals on the sky strong enough to trigger this effect.

3.5. Thermal drift decorrelation

The removal of the common mode due to temperature fluctuations of the 100 mK cooler stage is based on measured coupling coefficients between the bolometers and the bolometer plate temperature. The coefficients were measured during the CPV phase (typically 50 pW K^{-1} for bolometers up to the 353 GHz channel, and 300 pW K^{-1} for the 545 and 857 GHz channels). The two dark bolometers are used as a proxy for the bolometer plate temperature fluctuations, as HFI 100 mK thermometers have too many cosmic ray hits to be used. The two dark bolometer timelines are deglitched (in the same way as the other bolometers) then smoothed with a one minute flat kernel. From each bolometer timeline, a linear combination of the two smoothed dark timelines is subtracted. During this stage, the timelines of all signal bolometers are flagged during periods where any of the dark bolometers is flagged for at least 30 s. This is done in order to suppress the impact of large glitches happening on the bolometer plate. We found empirically that this method automatically excludes the worst solar flares and in particular the rising common mode induced by massive cosmic ray events. Note that the total range of the temperature fluctuations of the bolometer plate is less than 80 μK, except for some strong solar flares. As shown in Fig. 6 of Planck HFI Core Team (2011a), the temperature fluctuations of the 1.6 K and 4 K stages have a negligible influence on the TOI noise properties.

3.6. 4 K cooler line removal

Electromagnetic interference (by conduction) from the drive electronics of the 4 K cooler can affect the HFI data. The 4 K cooler main frequency (40 Hz) is an harmonic of the signal sample frequency; it leads to very narrow lines in the power spectral density (PSD) of the signal. In system tests before launch, the design of the grounding system of this part was found to be out of specification, but could not be corrected without unacceptable cost and delay. For a given stable 4 K cooler line, only one frequency is affected in the PSD, i.e., a narrow line is produced, only broadened by the limit on the pointingline period integration time. Nine individual frequencies are detectable, each of which can be traced to some 4 K cooler harmonic unfolded by the AC modulation. In the signal domain, they are at 10, 20, 30, 40, 50, 60, 70, 80, and 17 Hz, which are these fractions of the modulation frequency: 1/9, 2/9, 3/9, 4/9, 5/9, 6/9, 7/9, 8/9, 5/27. The modulation frequency itself is filtered out (see Sect. 3.7). Some thermal instability in the service module makes the line properties change on time scales larger than ten minutes.

We now describe the method used to correct the 4 K cooler line contamination in the timelines. In order to prepare the data from which to compute the Fourier coefficients, we build an intermediate set of of TOI, denoted TOI4K, containing the original TOI except in glitch-flagged areas which are noise-filled, and for Solar System objects (SSO) where the signal is estimated from SSO-free maps.

Then, we measure the cosine and sine Fourier coefficients on the TOI4K for each of the nine lines, once per pointing period. We thus neglect variations of these components within the duration of a pointing period.

We can then subtract from the original TOI objects a timeline made of the nine reconstructed Fourier components. This notch filter scheme produces ripples around strong point sources (see Planck HFI Core Team 2011b). The origin of this problem lies in the position of the 4 K cooler line frequencies with respect to the harmonics of the spin frequency. Most of the time (typically 90% of the pointing periods), a given 4 K cooler line does not overlap with any spin frequency harmonics and thus does not affect the signal at all. The spin frequency is very stable within a pointing period and varies from one pointing period to another by a factor of at most 10^{-4}. Hence, in so-called resonant pointing periods, a 4 K cooler line overlaps one harmonic of the spin frequency. Operationally, overlap is declared when the 4 K cooler line frequency is within twice the reciprocal of the pointing period duration of one of the spin frequency harmonics. In the resonant rings, the Fourier coefficients are perturbed by the signal and no longer represent the systematic effect alone, hence resulting in ripples around point sources. For those pointing periods only, we interpolate the Fourier coefficients from adjacent non-resonant pointing periods and subtract the systematic timeline from the original TOI objects in the same way as the other pointing periods.

While tests with simulations (described in Planck Collaboration 2013) demonstrate that any residual 4 K line contamination is reduced to less than 3% of other sources of noise, these lines also affect our ability to characterize and remove the ADC nonlinearity (discussed in Sect. 7.2.1), and are thus still a subject of active analysis.

The efficiency of our removal procedure may be judged by comparing map power spectra with this step switched on or off. It is found that the affected multipoles are at $\ell \simeq 60\,(f/1\,\mathrm{Hz})$, i.e., 600, 1020, 1200, 1800, ... When the module is switched on, the line residuals amount to no more than 2.5% of the noise level at those multipoles and much less elsewhere (see Planck Collaboration 2013).

3.7. Fourier transform processing

The bolometer response suffers from time-constant effects, which must be corrected. These effects, modelled as a complex transfer function whose parameters are determined on planet data (see Sect. 3.11), are deconvolved at the end of TOI processing. An additional filter is applied in order to avoid a large increase in noise (without much signal) produced by the deconvolution in the last 20 Hz near the modulation frequency. This filter has a perfect zero at the modulation frequency. We refer the reader to a dedicated accompanying paper for a complete description (Planck Collaboration VII 2014). Filtering and deconvolution are performed during the same Fourier and inverse Fourier transform stage. Chunks of 2^{19} samples are used at a time, with a standard fast-Fourier transform (FFT) and inverse. The deconvolved and filtered data are then computed and saved for the middle 2^{18} samples. The process is continued by shifting the input samples by 2^{18} until the end of the timeline. This ensures continuity in the recovered final timelines.

For the 545 and 857 GHz channels, the filtering is digital and consists of a simple local smoothing kernel: 0.25, 0.5, 0.25. For these channels, the filtering is applied first, then the deconvolution is done with the FFT module.

3.8. Jump corrections

We now build another set of intermediate *signal-removed* TOI from the deconvolved data. These consist mostly of noise, except in regions of strong gradients, for example near the Galactic plane. Some pointing periods are seen to be affected by a sudden jump (either positive or negative) in the *signal-removed* TOI. We therefore correct for that jump by subtracting a piecewise-constant template from the timeline, while preserving the mean level. Since the exact jump location cannot be determined very precisely, the TOI are flagged around the recovered position with 100 samples on each side.

We find on average 17 jumps per day, over all bolometers, with jumps affecting a single bolometer at a time. Hence, a fraction less than 10^{-5} of data is lost in the flagging process. The jump rate fluctuates during the mission, with a peak-to-peak variation of nine jumps per day. So far, there is no real explanation for these events, although we suspect violent cosmic ray hits on the warm electronics.

We have checked the jump correction process on simulated jumps of various intensities added to pointing periods without jumps. All jumps above half the local standard deviation of the *signal-removed* TOI are found.

3.9. Flagging samples

We now build a total flag out of several flags in order to qualify the TOI for mapmaking. A sample with any of the following flags is considered *invalid data.*

1. The *unstable pointing* flag described in Sect. 3.1 (see also Planck Collaboration I 2014), typically accounting for three minutes per pointing period (roughly 7% of data).
2. The *missing or compression error* data flag, discarding a fraction of 10^{-9} of the whole mission (see Planck HFI Core Team 2011a).
3. The *bolometer plate temperature fluctuation* flag (see Sect. 3.5). One to two percent of the data are flagged this way depending on time.
4. The *glitch* flag. Typically between 8 and 20% of the data are flagged depending on the time and the bolometer (Planck Collaboration X 2014). For PSBs, both detectors are flagged even if, in a few cases, only one of them exhibits the glitch.
5. The *jump* flag. Two hundred samples per jump are flagged, a fraction less than 10^{-5} (see Sect. 3.8).
6. The Solar System object (*SSO*) flag. A zone of exclusion is defined around Mars, Jupiter, Saturn, Uranus, Neptune, and around the 24 asteroids detected at 857 GHz (see the complete discussion of asteroids in Appendix A of Planck Collaboration XIV 2014). The coordinates of the objects are obtained from the JPL Horizons database[2] (Chamberlin et al. 1997), which uses the actual position of the *Planck* satellite in its orbit around the L2 point. As the Solar System objects are moving in celestial coordinates, the data (although valid) must be discarded and this masking must be done in the time domain. One survey map thus has up to 35 holes, which are filled by information from other surveys. Overall, the final maps have almost no holes: less than 10^{-5} of pixels are missing.

3.10. TOI qualification

On top of flagged samples in the TOI, we show now that some flagging also has to be done at the pointing period level (i.e., considering entire rings of data).

We will later make maps by projecting the PBR into sky coordinates. We therefore base our criteria for the acceptance or rejection of a given pointing period for mapmaking by using the statistics of only the *signal-removed* TOI as an estimate of the noise. Hence, the qualification is minimally biased by the variation of the signal itself.

This noise estimate timeline is first analysed in the Fourier domain. In Planck HFI Core Team (2011b) we described how the detector white noise level (equivalently, the NET) is determined from noise periodograms in the frequency region beyond the low frequency excess noise component and before the increase introduced by the time-constant deconvolution. Planck HFI Core Team (2011b) describes other properties of the noise for each detector, including the knee frequency and estimated spectral index of the $1/f^{\alpha}$ noise component.

This white noise level differs from that deduced directly from the maps. We have therefore adopted a method for determining the "total" noise: this is derived directly from the standard deviation of the *signal-removed* TOI after flagging the Galactic plane and point sources for each pointing period. The standard deviation is then corrected upward by a term that depends on the duration of the pointing period. This term has the form $\sqrt{fd/(fd-1)}$, where d is the pointing period duration in minutes and f is the fraction of valid data within a pointing period (typically 0.8). It accounts for the fact that a fraction of the noise remains in the PBR, and that fraction is smaller in longer pointing periods, where the signal is better estimated. The final value of this total noise level for each detector (third column of Table 2) is then taken to be the peak of the distribution of the root-mean-square (rms) noise of the valid pointing periods. The typical bolometer NETs, measured on the deconvolved TOI between 0.6 and 2.5 Hz, are also given in Table 2 (second column). The total noise can be viewed as proportional to the square root of the integral of the square of the noise-equivalent temperature across the total frequency bandpass (including filtering effects) from 0 to 91 Hz. It is normalized to one second of integration

[2] http://ssd.jpl.nasa.gov/

Table 2. Noise characteristics.

Band	NET	Total noise	Goal	Units
100P	71	132	100	$\mu K_{CMB}\ s^{1/2}$
143P	58	65	82	$\mu K_{CMB}\ s^{1/2}$
143S	45	49	62	$\mu K_{CMB}\ s^{1/2}$
217P	88	101	132	$\mu K_{CMB}\ s^{1/2}$
217S	74	66	91	$\mu K_{CMB}\ s^{1/2}$
353P	353	397	404	$\mu K_{CMB}\ s^{1/2}$
353S	234	205	277	$\mu K_{CMB}\ s^{1/2}$
545S	0.087	0.052	0.116	MJy $sr^{-1}\ s^{1/2}$
857S	0.085	0.056	0.204	MJy $sr^{-1}\ s^{1/2}$

Notes. The quoted value is the noise that is obtained on the map after one second of integration, i.e., about 180 hits for one bolometer. This gives the noise characteristics of bolometers, inverse quadratically averaged over the similar ones within a channel ("P" is for polarization sensitive bolometers and "S" for spider-web unpolarized bolometers). The second column gives the white noise level measured on the power spectrum in the range of 0.6 to 2.5 Hz. The third column gives the total noise, i.e., the rms noise at the map level for one second of integration time of a single detector. The next column recalls the goal stated before launch by Lamarre et al. (2010). Note that the mean integration time per detector per $(1.7')^2$ pixel is 0.56 s for the 100−353 GHz channels and 0.63 s for 545 and 857 GHz, for the nominal mission (see Fig. 21).

time, so that pure white noise would have numerically identical NET and total noise. Deconvolution and filtering effects can produce a NET larger or smaller than the total noise.

The noise estimate is also analysed in the time domain. Figure 4 shows one pointing period of the *signal-removed* TOI for four detectors, along with the histogram of the samples.

Figure 5 shows an example of the evolution of this total noise (uncalibrated at this stage) during the first four surveys (hence beyond the nominal mission). The bias linked to the pointing period duration has been corrected for. Notice that the total noise is mostly constant, with peak-to-peak variations at the percent level, suspected to be induced by ADC non-linearities (see Sect. 6.2).

A pointing period that deviates significantly from the others is flagged in the qualification process and not used in further processing. Three criteria were used to quantify the deviation:

- the absolute value of the difference between the mean and the median value of the *signal-removed* TOI;
- the total noise value; and
- the Kolmogorov-Smirnov test deviation value – when a given pointing period is stamped as anomalous for more than half the bolometers, it is discarded for all of them.

The common anomalous pointing periods are linked to some spacecraft events or strong solar flares, while the individual anomalous pointing periods correspond to incidents in the overall level of the timeline (like strong drifts).

There are two detectors (one each at 143 and 545 GHz, not counting toward the total of 50 HFI detectors) that are not used at all because they show a permanent non-Gaussian noise structure, which we call random telegraphic signal (RTS). The RTS bolometer *signal-removed* TOI show an accumulation of values at two to five discrete levels. The measured *signal-removed* TOI jump at random intervals of several seconds between the different levels. The jumps are uncorrelated. A third detector (at 857 GHz) shows the RTS phenomenon only for some well-delimited periods amounting to 7.4% of the nominal mission. Other detectors show a significant but smaller RTS in episodes of short duration (2.1% and 1.2% of the data from two 217 GHz bolometers). A dedicated module searches for these episodes, which are then added to the list of discarded pointing periods. Ten pointing periods of exceptionally long duration are discarded for all bolometers, because noise stationarity is not satisfied in those cases. The discarded pointing periods represent less than 0.8% of the total integration time for the nominal mission.

Many examples of the characterization and qualification of the TOI processing can be found in Planck Collaboration (2013), where simulations are used to limit the possible effects of undetected RTS periods to a fraction of the overall noise level. In addition, Planck Collaboration (2013) presents a number of simulations and other tests which have been done to set limits on possible contamination from other possible systematic effects.

3.11. Big planet TOI

As the TOI of the standard pipeline are interpolated around Mars, Jupiter, and Saturn, they cannot be used for the beam reconstruction (see Sect. 5). Therefore a dedicated pipeline is run on appropriate pointing period ranges. The difference from the standard pipeline is mainly a special deglitching step performed on the planet samples to cope with such a strong signal and its variations during a given pointing period. Also, the jump correction is not applied to avoid being triggered by the planet transit.

4. Detector pointing

Here we summarize the pointing solution we use, determined with the overall goal of limiting detector pointing errors to less than 0.″5 (rms). The satellite pointing comes from the star tracker camera subsystem, which gives the location of a fiducial boresight direction as a function of time, sampled at 8 Hz. In practice, science data analysis requires the pointing of each detector, sampled at the same rate as the detector signal. This, in turn, requires a number of separate steps:

1. resampling to the acquisition frequency (180.4 Hz);
2. rotation from the fiducial boresight to the detector line of sight; and
3. correction for detector aberration (Planck Collaboration XXVII 2014).

The second step must be calibrated in situ: the detailed geometry must be measured by comparison with the positions of known objects (planets and other bright sources whose extent is small compared to the width of the beam). The primary source of this geometrical calibration is the planet Mars, which is bright (but not so bright as to drive the detectors into a nonlinear response) and nearly pointlike (with a mean disk radius of 4.″1 during the nominal mission). Figure 6 shows the pointing of each detector relative to the pre-launch optical model.

Note that the in-scan pointing is degenerate with any phase shift induced by the combined detector time response and optical beam and any attempt to remove them by deconvolution (Planck Collaboration VII 2014). For that reason, this calibration of the pointing cannot be considered as a measurement of the focal plane geometry per se.

Because the transfer of the pointing from the star tracker to the detectors depends on the satellite rotation axis and hence the moment of inertia tensor, we do not expect the detector pointing relative to the star tracker to be constant in time. We therefore reconstruct the pointing solution relative to the star tracker as a

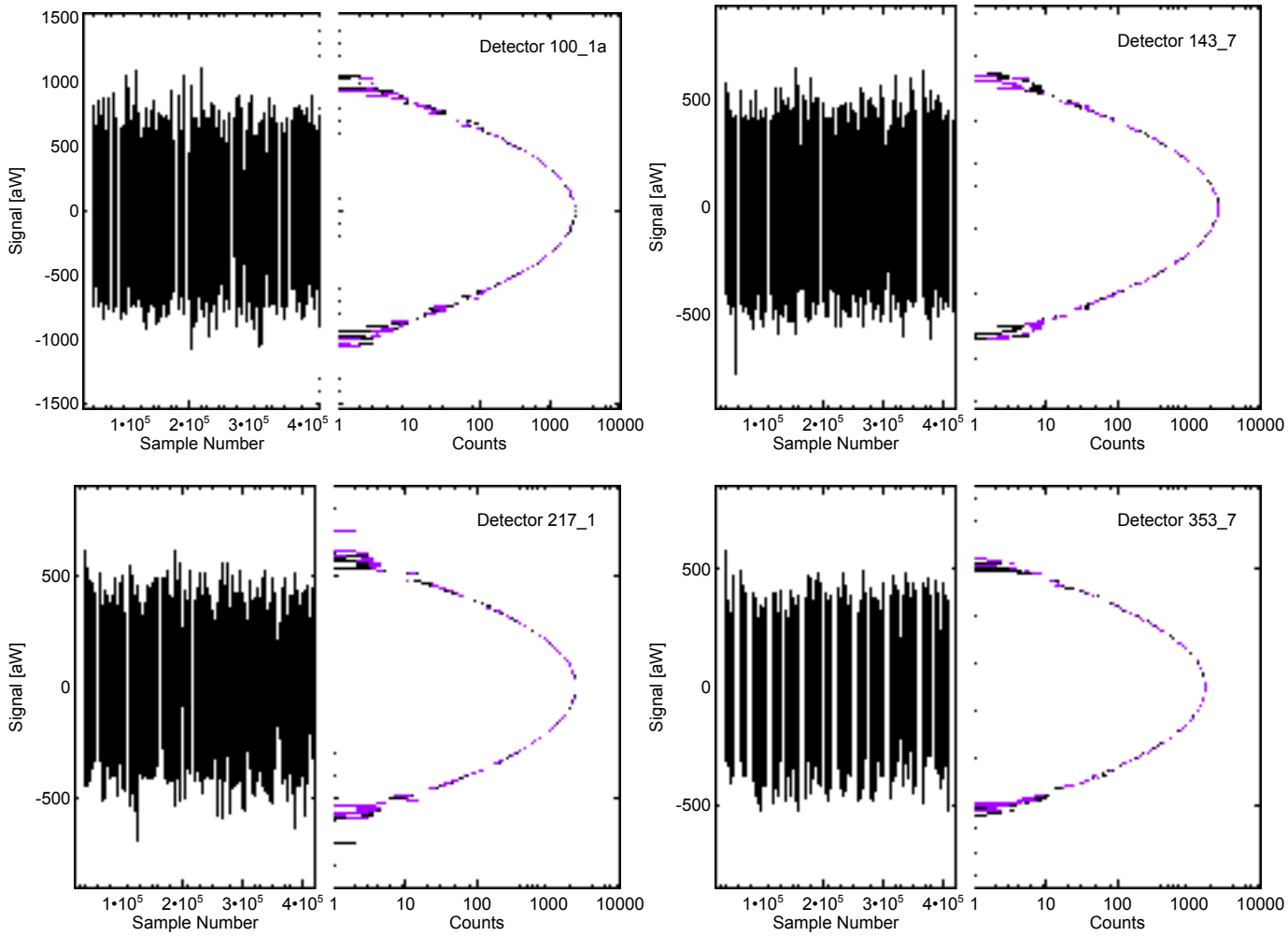

Fig. 4. *Signal-removed* TOI sample values displayed for one pointing period and four detectors (*left panel* in each of the four sets). Flagged samples are not shown. Samples falling near the Galactic plane or point sources are not shown (corresponding to one-minute periodic blanks in the plots). The *right panel* of each graph shows the histogram (in black) of the samples. The coloured curve is the vertically reflected version of the histogram around the mean.

function of time, and in the following discuss the accuracy of the reconstruction in different frequency regimes.

High-frequency fluctuations in the spacecraft and focal plane orientation are inhibited by inertia, but are still present in the raw star tracker pointing. Having no useful signal content, this regime is treated by applying a low pass filter to the reconstructed pointing. Similarly, high-frequency errors can be assessed by studying the noise-dominated high frequency pointing power spectrum.

Intermediate-frequency pointing errors, on one minute time scales, are characterized with Jupiter transits. We make use of the optimal combination of high signal-to-noise ratio and relatively wide beam at the *Planck* 143 GHz channel and first perform a global fit of the planet position in the transit data. We then consider a small pointing offset to each 60 s scanning circle. This successfully recovers an expected interference signal from the radiometer electronics box assembly (REBA; see Planck Collaboration II 2011 and Planck Collaboration I 2014). Thermal control on the REBA was adjusted on day 540 after launch and subsequently Jupiter transit three does not exhibit the interference. We find that the intermediate-frequency pointing error is less than 3″ (rms) before the REBA adjustment and less than 1″ beyond day 540 (see Fig. 7).

The pointing is easiest to monitor over long time scales, using observations of bright planets. In Fig. 8 we show the difference between the first two observations of Mars; differences along the scan direction have a mean of 0.″85 and a standard deviation of 0.″59, while cross-scan differences in the direction perpendicular to this are 3.″7 ± 2.″8 and are systematic with frequency. Indeed, analysis of further planet-crossings and of aggregate high-frequency point-source crossings shows arcminute-scale evolution over the course of the mission. Fitting for an overall offset for each planetary transit allows us to measure long time scale (several days) pointing fluctuations. We complement this sparse sampling of the overall offset by time domain position fits of the brightest compact radio sources as well as monitoring of many low-flux-density high-frequency sources in aggregate. In the process we learned that each radio source position was biased by a few arcseconds from its catalogued position. We assume the bias results from convolving the source emission with our effective beams and correct for it by assuming that the low frequency pointing correction derived from planet transits alone is already accurate enough for debiasing the positions. We solve for the apparent position of each compact source in the *Planck* data by estimating a single constant offset from its catalogued position.

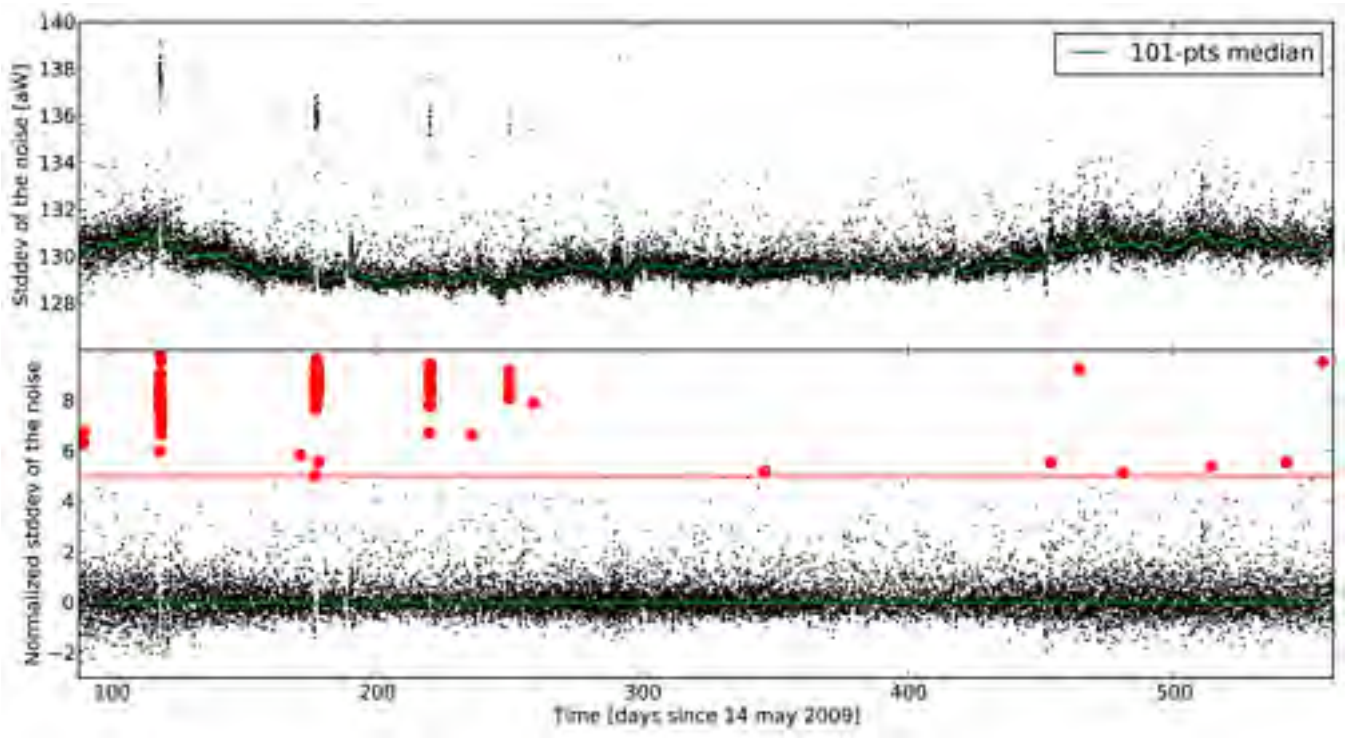

Fig. 5. *Top*: total noise estimated for each stable pointing period for a 143 GHz PSB. A smoothed version is shown in green. *Bottom*: a version of the upper plot shifted to zero mean and normalized to unit variance shows how outliers, the red dots, are picked up (above 5σ of the moving median in green).

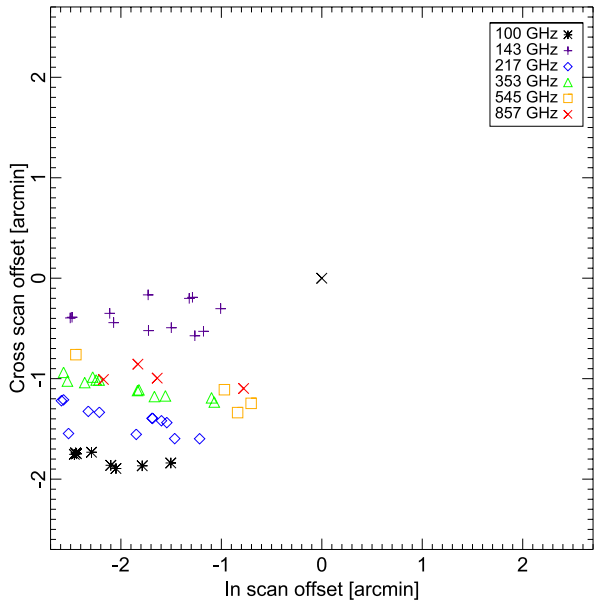

Fig. 6. Positions of the individual HFI detectors with respect to a pre-launch model, as measured on the first pass of Mars. The horizontal axis is the direction of the scan ("in-scan"); vertical is perpendicular to this ("cross-scan").

The planet positions alone indicate a change in the average level of the low frequency fluctuations between Jupiter transit two and Neptune transit three (days 418 and 540 from launch). The radio sources, particularly QSO J0403−3605, further narrow the transition before day 456. It is likely that the offset is due to thermoelastic deformation caused by the sorption cooler system switchover on day 460 (Planck Collaboration II 2011; Planck Collaboration I 2014). If entirely untreated, the low frequency pointing error dominates the error budget with around 15″ (rms) error. Two independent focal plane solutions bring the low-frequency rms error well below 10″ and applying a time-dependent correction reduces the low frequency error to a few arcseconds.

Figure 9 shows the uncorrected planet positions with the debiased bright point-source positions along with the resulting *Planck* pointing solution, which smoothly interpolates with a spline fit between planet observations. Figure 8 shows the offset of Mars for all detectors between the first and second surveys after correction by the pointing solution and Fig. 10 the effect of the corrected pointing on the high-frequency point sources at 545 and 857 GHz.

After these corrections, the pointing error is about 2.″5 (rms) over the mission, less than 1″ during planet observations, and increasing between planet crossings. The individual HFI detector locations (along with their respective beam patterns) are shown in Fig. 11.

5. Detector beams

Here we provide a brief overview of the measurement of the *Planck* HFI beams and the resulting harmonic-space window functions that describe the net optical and electronic response to the sky signal , as well as the impact of processing (for a full discussion see Planck Collaboration VII 2014).

At any given time, the response to a point source is given by the combination of the optical response of the *Planck* telescope (the *optical beam*) and the electronic transfer function. The latter is partially removed as discussed in Sect. 3 and Planck Collaboration VII (2014), but any residual is taken into account as part of the beam. This response pattern is referred to

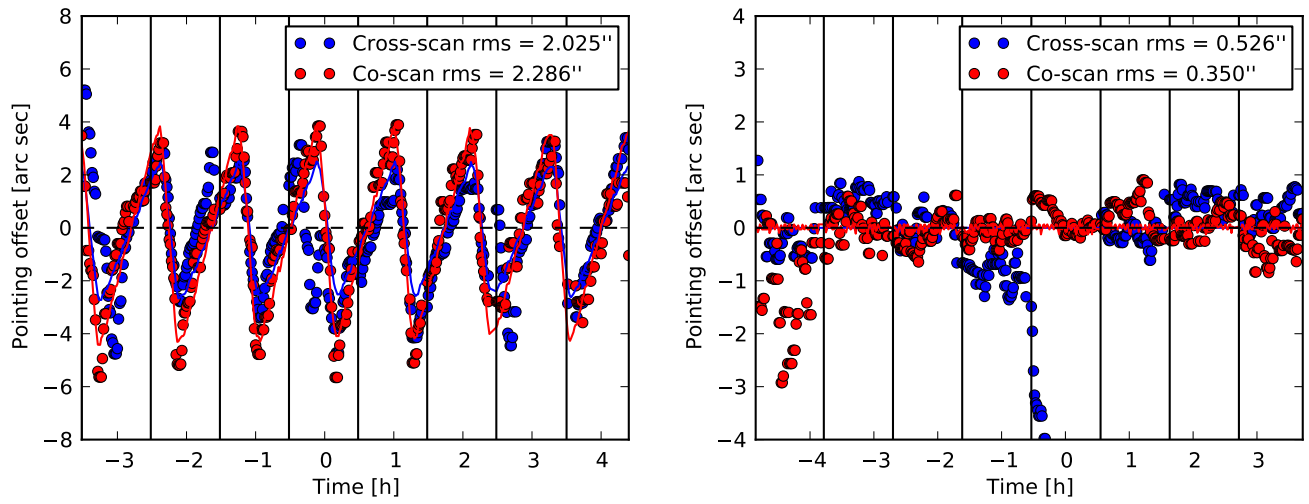

Fig. 7. Measured intermediate frequency pointing errors at one minute intervals. The plotted time span covers the period that Jupiter is within one FWHM of the 143-1a bolometer beam center. The offsets were smoothed with a five-point median filter. Vertical lines mark the pointing period boundaries. The overplotted solid line is the scaled and translated REBA temperature. REBA thermal control was adjusted between Jupiter transits two and three. *Left*: pointing fluctuations during the second Jupiter transit. *Right*: fluctuations during the third Jupiter transit, after the REBA thermal control was adjusted. Note the different vertical scales.

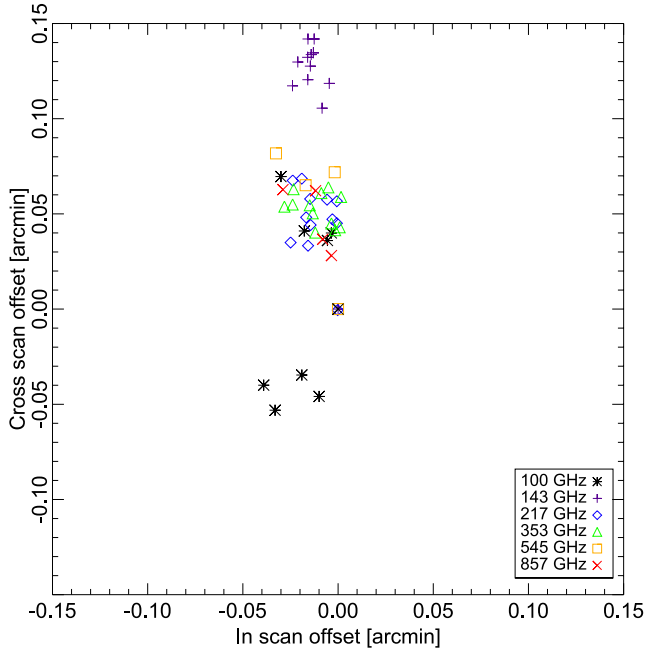

Fig. 8. Pointing differences between the first and second crossings of Mars, as in Fig. 6 (but note the different axis scales).

as the *scanning beam, which includes any further effect due to the temporal data processing*. However, the mapmaking procedure discussed in Sect. 6 below implies that any map pixel is the sum of many different samples in the timeline, each of which contributes in a different location within the pixel and with a different scan direction. Thus, the *effective beam* (Mitra et al. 2011) takes into account the details of the scan pattern (and even this is a somewhat simplified picture, as long-term noise correlations accounted for by destriping in the mapmaking procedure described in Sect. 6 mean that even samples taken when the telescope was looking elsewhere contribute to a given pixel). Finally, the multiplicative effect on the angular power spectrum is encoded in the *effective beam window function* (Hivon et al. 2002), which includes the appropriate weights for analysing aggregate maps across detector sets or frequencies.

5.1. Scanning beams

For the single-mode HFI channels, the scanning beam is well-described by a two-dimensional elliptical Gaussian with small perturbations at a level of a few percent of the peak (Huffenberger et al. 2010). We measure the beams on observations of Mars, and model them with B-spline fits to the timeline supplemented with a smoothing criterion as discussed in Planck Collaboration VII (2014).

We measure the beam on a square patch 40′ on a side. This main beam pattern must be augmented by several effects that are visible within roughly 1° of the beam centre due to variations of the mirror surface. At all frequencies we see evidence of unmodelled effectively random dimpling, well-fit by a sum of Ruze (1966) models. At 353 GHz and higher we see evidence of the hexagonal backing structure of the mirrors, included directly in the B-spline fits. The scanning beam patterns for each detector are shown in Fig. 11.

Other steps in the data processing pipeline also affect the scanning beam pattern. We see residual effects from the deconvolution as a shoulder in the beam localized to the "trailing" side of the scan. The residual pointing uncertainty results in a slight broadening of the beam which is modelled in the Monte Carlo simulations we use to estimate the beam errors. Further simulations indicate that undetected or inaccurately removed glitches (Sect. 3.3) result in a negligible additional bias, as do the uncorrected ADC non-linearities. Because the response of the detector depends on the spectral shape of the source, there is a colour correction (see Sect. 6.6) when converting from the approximately known planet spectrum (roughly ν^2) to the nominal ν^{-1} shape.

All of these give a change in the beam solid angle of roughly 0.5% at 100 GHz and less than 0.2% for 143 GHz and above. However, there is an additional contribution to the scanning beam from near sidelobe response beyond the square patch on which the beam is measured (e.g., from the deconvolution of the time response). Simulations show that the near sidelobes contribute less than 0.2% of the beam power.

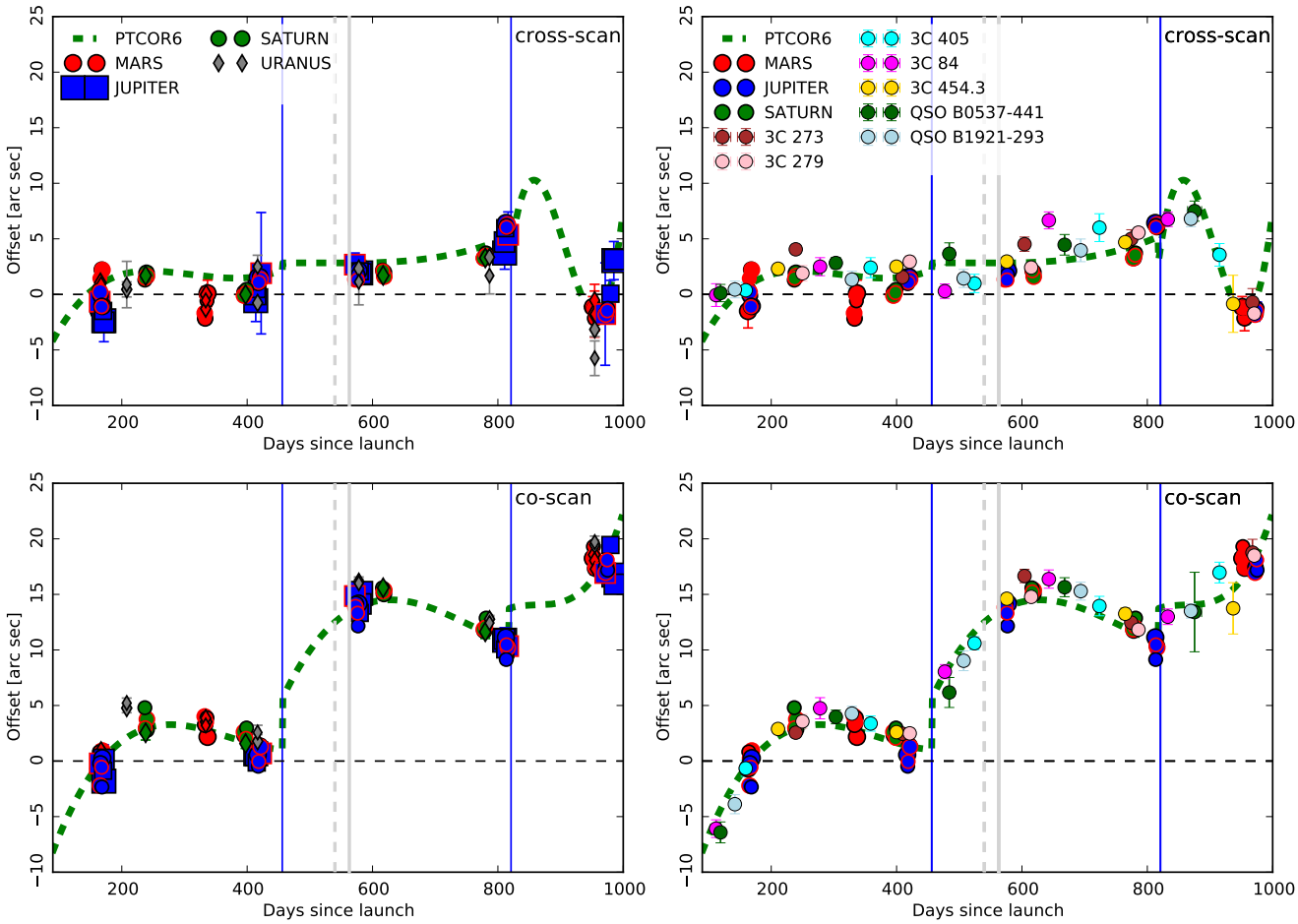

Fig. 9. Compilation of planet and bright point-source positions versus time since the start of the mission. We mark the REBA thermal control adjustment on day 540 with a dashed grey line and the end of the nominal mission (day 563) with a solid grey line. Note the two discontinuities added to the pointing correction model at days 455 and 818. The dashed green line denotes the spline fit to the planet positions used to correct the long-term pointing variations. *Left*: compilation of measured planet position offsets across the *Planck* frequencies. Usable planets change by frequency: the blue spectral energy distribution of the planets renders all but Jupiter too dim for required positioning in the LFI frequencies and Jupiter and Saturn positions above 217 GHz are compromised due to the nonlinear bolometer response. *Right*: debiased bright source position offsets in *Planck* 100–217 GHz data compared to a trend line fitted to the planet position offsets. Each source was fitted for an apparent position rather than using the catalogued position to measure pointing offset. Two successive observations of the same source have opposite scanning directions, so having the wrong apparent position produces opposite pointing errors that we have corrected.

Planck Collaboration XXXI (2014) shows that accounting for this contribution would further improve the good agreement between HFI and LFI at adjacent frequencies.

5.2. Effective beams

The scanning beams are used to calculate the effective beam response at a given pixel. A symmetric beam in a uniformly-sampled pixel (and ignoring effects induced by long-time-scale noise correlations accounted for in the mapmaking procedure) would give an effective beam that is the convolution of the scanning beam pattern with a top-hat pixel window function. Departures from these idealities, due to scanning beam asymmetry and the scan strategy, mean that the effective beam will be asymmetric and will depend upon sky location: ignoring long-term noise correlations, the effective beam is given by averaging the scanning beam pattern at the observed locations and orientations of the real scan pattern in each pixel. In practice, this must be approximated by using a coarse pixelization of the scanning beam or restricting the calculation to those components with low spherical-harmonic multipoles m. We have developed a set of methods in real and harmonic space to account for these effects, described more completely in Planck Collaboration VII (2014) and references therein.

We propagate the scanning beam pattern from each detector, along with the largest-variance eigenmodes of the Monte Carlo error covariance matrix, using the *Planck* scanning strategy. The error eigenmodes are scaled by a factor of 2.7 to account for the unmodelled near sidelobe bias in the scanning beam. The eventual calculation of power spectra requires the cross-correlation of various detector pairs and more generally arbitrary weighted combinations of detector pairs used to construct the final CMB power spectrum. Our algorithm results in both mean beam patterns (Fig. 12) and sky-averaged window functions, along with error eigenmodes on the latter (Fig. 13), for the required detector combinations. The far sidelobe response of the instrument (response to signal more than 5° from the beam centroid, discussed in Sect. 6.4) negligibly biases the calibration and the effective beam window function (Planck Collaboration VII 2014; Planck Collaboration XIV 2014). The full window functions are available with the *Planck* data release, and the key numerical results are shown in Table 4.

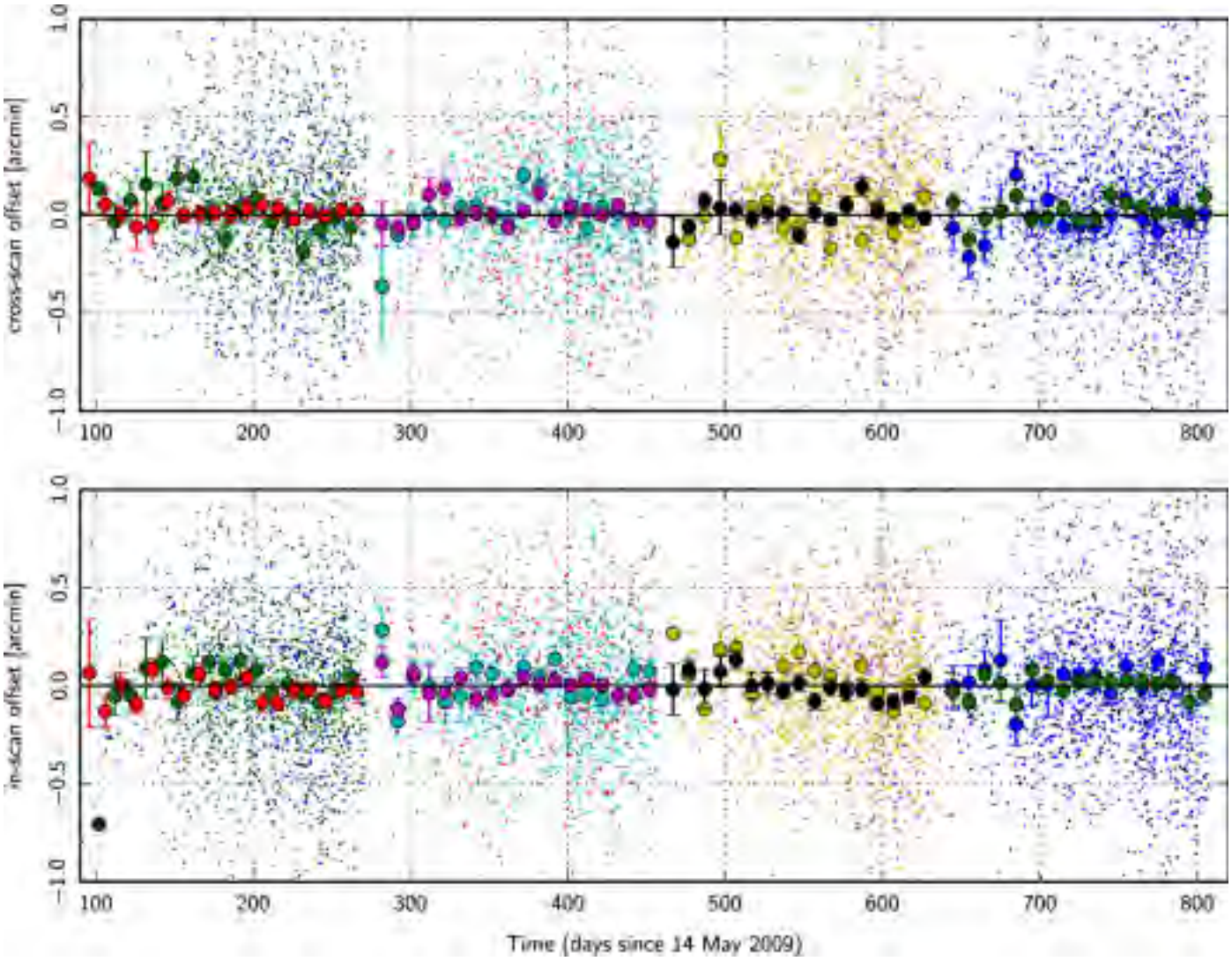

Fig. 10. Pointing evolution from aggregate high-frequency point sources, measured by comparing point sources seen at 545 and 857 GHz to known *IRAS* positions. Light-coloured points show individual source deviations, points with error bars give ten-day errors. Different colours correspond to the two frequencies and four individual *Planck* sky surveys.

6. Mapmaking and photometric calibration

This section gives an overview of the mapmaking and photometric calibration procedure. More details are described in Planck Collaboration VIII (2014).

6.1. Map projection and calibration techniques

The HFI mapmaking scheme is very similar to that described in Planck HFI Core Team (2011b). The inputs for each detector come from the TOI processing (see Sect. 3) with the associated *invalid data* flags. Mapmaking is done in three steps. We first take advantage of the redundancies during a stable pointing period (ring of data) by averaging each detector's measurements in `HEALPix`[3] (Górski et al. 2005) pixels, building a new data structure, the `HEALPix` pixel ring (HPR). We prefer to use this structure for mapmaking, rather than the phased binned rings previously described, because the latter introduce an additional smoothing in the reconstructed map power spectra. We set the `HEALPix` resolution for the HPR at the same level as for the final maps, $N_{\rm side} = 2048$, for the same reason. In the second step we use these HPRs to perform the photometric calibration of each detector's data. Once this is done, the mapmaking per se is performed. As for the previous release, the mapmaking procedure algorithm we used is an implementation of a destriping algorithm, which is made possible by the characteristics of the HFI detector noise.

In the destriping framework, detector noise is modelled as a set of constants, called offsets, representing the low-frequency drift of the signal baseline over given time intervals, and a white noise component uncorrelated with these constants. The general mapmaking scheme may thus be written in this approximation as a solution to the equation

$$\boldsymbol{d} = G \times \mathsf{A} \cdot \boldsymbol{T} + \Gamma \cdot \boldsymbol{o} + \boldsymbol{n}, \quad (2)$$

where $\boldsymbol{d}$ is the vector of TOI data, $\boldsymbol{T}$ represents the pixelized sky (which may be a vector (I, Q, U) at each pixel if polarization is accounted for), G is the detector gain, A is the pointing matrix indexed by sample number and pixel, equal to zero when the pixel is unobserved at that sample, one when the pixel is observed by an unpolarized detector, or the vector $(1, \cos 2\alpha, \sin 2\alpha)$ for a polarized detector at an angle α with respect to the axis defining

[3] `http://healpix.sourceforge.net`

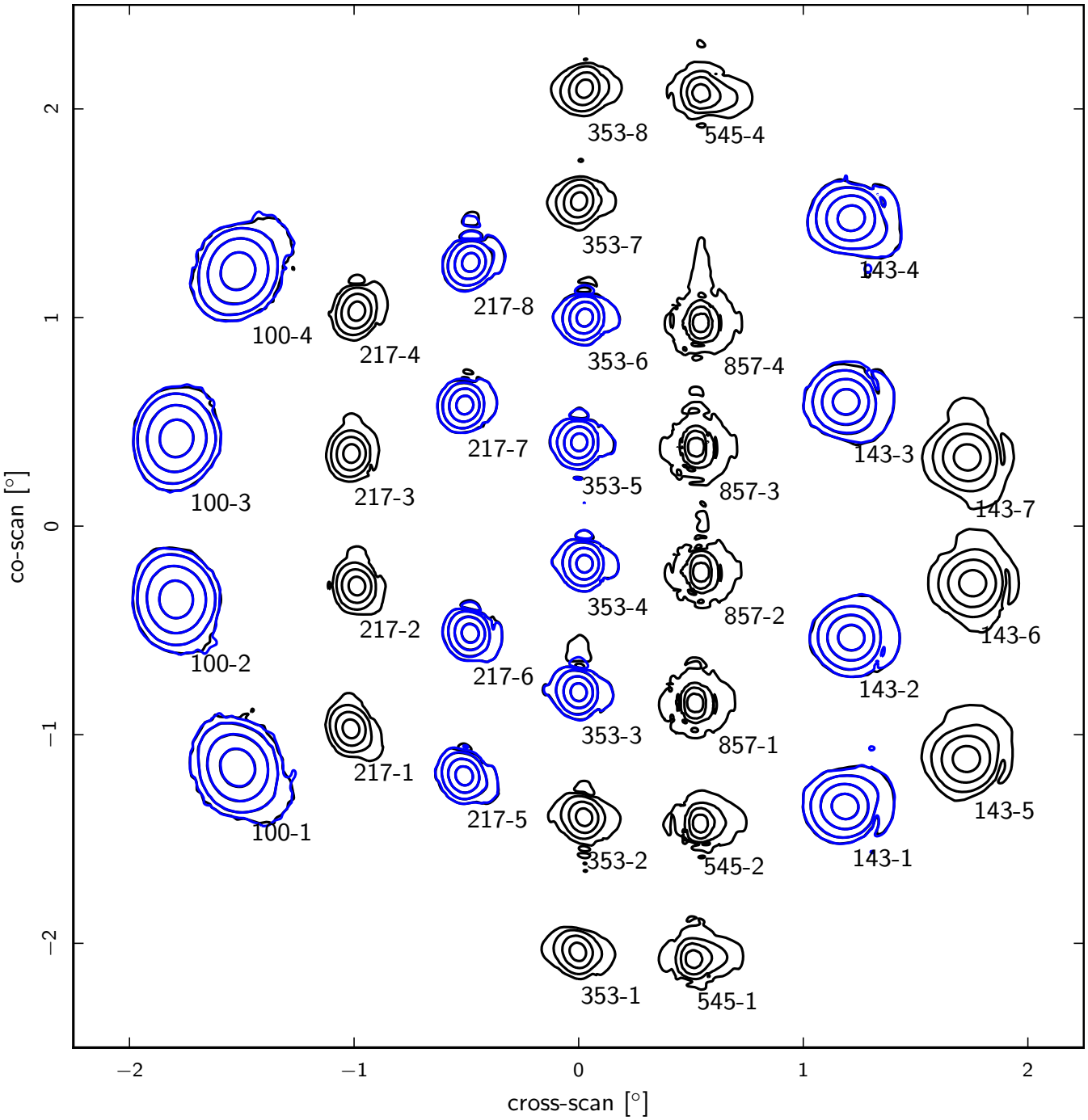

Fig. 11. Scanning beam patterns reconstructed from planet observations at their respective positions in the HFI focal plane. The contours are plotted at −3, −10, −20, and −30 dB from the peak of each beam. Polarization-sensitive bolometers are indicated as a pair of contours, one black and one blue (in most cases the underlying black contour is invisible, indicating essentially identical beam shapes).

the Stokes parameters, and Γ is the matrix folding the ring onto the sky pixels. From the above equation, the offsets $\boldsymbol{o}$ are derived through maximum likelihood, imposing an additional constraint, in our case that the sum of the offsets has to be equal to zero (arbitrarily, since we do not measure the absolute temperature on the sky, only differences). The performance of this implementation has been evaluated using simulations in Tristram et al. (2011).

We produce temperature and polarization maps for a number of data sets:

- individual detectors;
- independent detector sets at the same frequency (see Table 1); and
- the combination of all detectors at each frequency.

To enable systematic checks, we build maps for the whole time interval spanned by the HFI data, as well as more restricted intervals corresponding to individual surveys. We also build maps in each of the above cases using data from the first and second half of the rings independently. In each case (a full ring or its two halves) we first determine the offsets on the total time range and apply them to produce maps on any more restricted time range. Together with each temperature map, we build maps containing

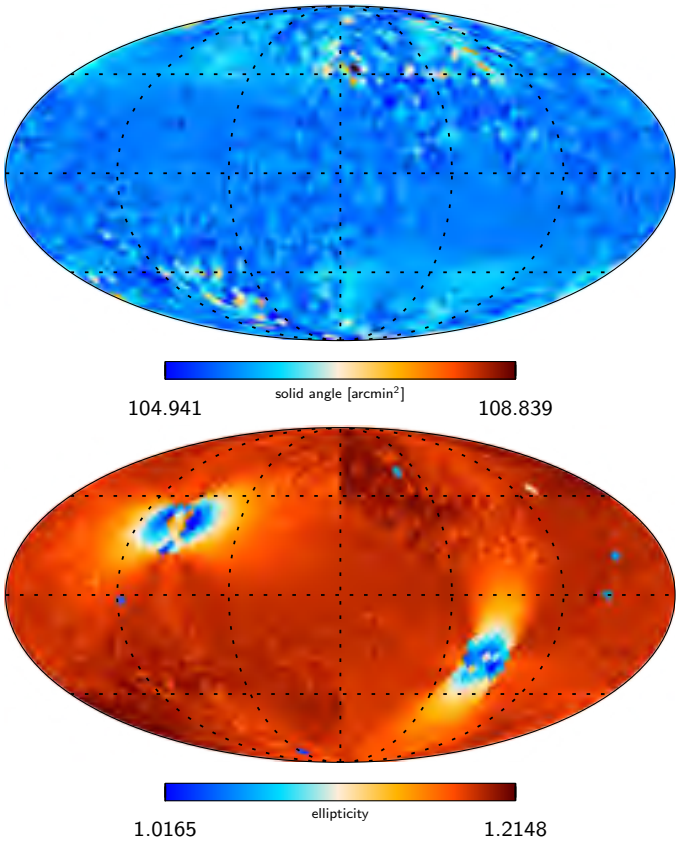

Fig. 12. Effective beam solid angle (*upper panel*) and the best-fit Gaussian ellipticity (*lower panel*) of the 100 GHz effective beam across the sky in Galactic coordinates.

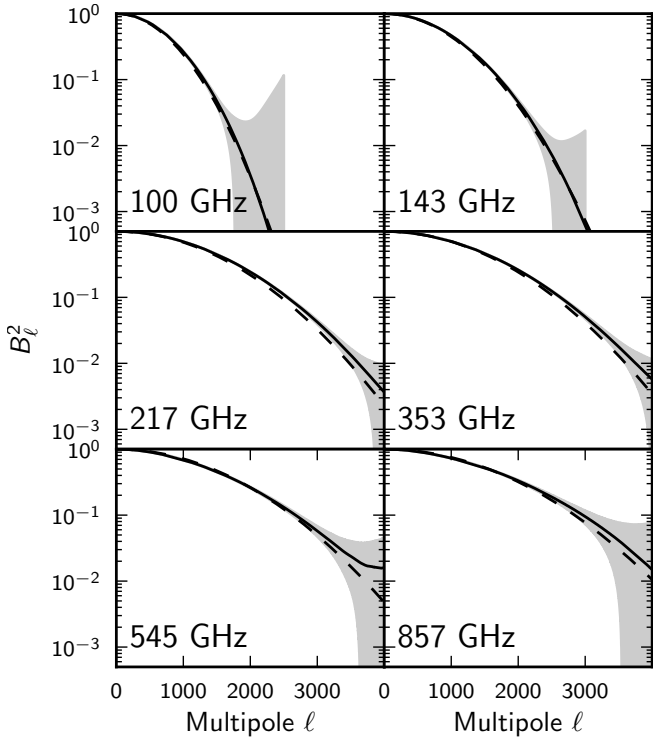

Fig. 13. Effective beam window functions (solid lines) for each HFI frequency. The shaded region shows the $\pm 1\sigma$ error envelope. Dashed lines show the effective beam window function for Gaussian beams with FWHM 9.′65, 7.′25, 4.′99, 4.′82, 4.′68, and 4.′32 for 100, 143, 217, 353, 545, and 857 GHz, respectively. We compute the 100 GHz window function to $\ell = 2500$, 143 GHz to $\ell = 3000$, and the rest to $\ell = 4000$.

the hit count (number of TOI samples in each pixel) and the propagation of the TOI sample variance, as measured by the total noise NET (see Sect. 3.10). In total, more than 6500 maps are produced.

6.2. Absolute photometric calibration

We use two techniques to perform the photometric calibration of the HFI detectors, one for lower frequency channels (100−353 GHz, typically given in temperature units, K_{CMB}), another for higher frequency channels (545 and 857 GHz, given in flux density units, MJy sr^{-1}). In both cases, significant changes have occurred with respect to the early data processing. The photometric calibration processes and their performance are described in detail in Planck Collaboration VIII (2014). Our philosophy is to calibrate each detector individually, without relative calibration between them.

Previously (for the early results from *Planck*), the lower frequencies were calibrated using the solar dipole, and the higher frequencies using FIRAS dust spectra measurements, assuming constant gain. When more data were accumulated, comparisons between measurements taken one year apart in identical detector configuration unambiguously showed that the detectors' gains exhibit variations of 1 to 2%, over a wide range of time intervals (one day to one year).

We also found that these apparent gain variations are primarily consequences of the nonlinearities of the ADC used in the read-out electronic chain (see Sect. 7.2.1). Correcting for such effects requires a precise knowledge of the ADC transfer function. To acquire these we characterized the read-out response using warm data after the end of the 100 mK cooling in January 2012. This data-taking was not completed in time for the 2013 HFI data release. At the frequencies where the solar dipole has a high enough amplitude (100 to 217 GHz) we evaluated the apparent gain variations of the detectors by solving the nonlinear equation $data = gain \times sky + noise$ for both gain and sky signal. Examples of gain-variation measurements are shown in Fig. 14. Note the wide range of behaviour, from slow drifts (e.g., 100-1a) to apparent jumps (e.g., 143-1a).

These measurements have been used to correct the bolometer data in the present data release. As these gain variations are just the first-order consequence of the ADC nonlinearities, these corrections will not remove all ADC nonlinearity effects. We estimate (Planck Collaboration VIII 2014) that the remaining apparent gain variations (or other residual time-variable systematics) after correction are lower than 0.3%, as measured by comparison with the solar dipole.

The presence of residual nonlinear systematic biases in our data precludes the use of potentially more precise techniques, such as those discussed in Tristram et al. (2011) using the orbital CMB dipole anisotropy. In Planck Collaboration VIII (2014) we show that using a calibration derived from the orbital dipole would lead to larger detector-to-detector relative calibration dispersion, which induces large-angular-scale patterns in polarization through dipole leakage. In addition, for detectors for which the Solar and orbital dipole difference is large (typically around 0.5% but in few cases as large as 1%), a residual dipole is apparent after subtracting the *WMAP* prediction. Thus, the calibration for 100 to 353 GHz is based on the solar dipole as measured by *WMAP* (we use a non-relativistic calculation; the roughly 0.1%

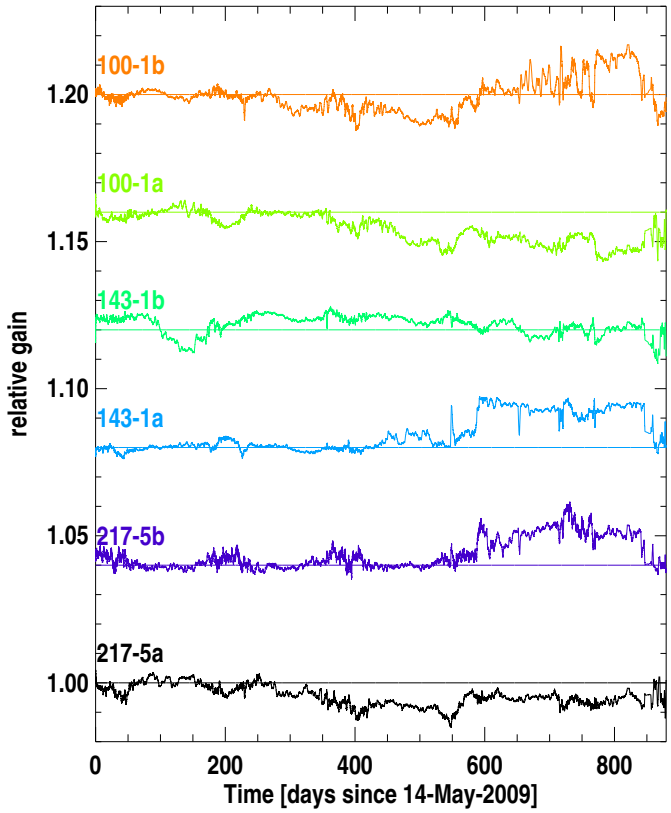

Fig. 14. Samples of relative gain variations reconstructed for six CMB channel bolometers. Data for each bolometer have been translated vertically for clarity, with a 3% spacing. In each case, thin lines show the average level over days 150 to 280, during which the solar dipole calibration is determined. The observed variations range in general over ±1.5%.

relativistic correction is smaller than other residuals such as the uncorrected ADC non-linearities).

For the two highest frequency channels, the calibration scheme that was used for the early data release was based on FIRAS data. As described in Planck Collaboration VIII (2014), several studies since the first release indicated that the calibration scale of these two channels was somewhat inaccurate. These include measurements of the dust spectral energy distribution and of the amplitude of the CMB anisotropy itself (still detectable at 545 GHz). Re-analysis of the FIRAS data (Liang et al. 2012) also seems to indicate that the FIRAS spectra might contain additional systematic errors. Since we also observed systematic differences between HFI and FIRAS data, we decided to revise our calibration strategy. We therefore now supplement our calibration using the reconstructed fluxes of planets, compared with models of their emission (Moreno 2010), in order to renormalize the relative FIRAS calibration at 545 and 857 GHz. We used observations of Uranus, Neptune, and Mars (Jupiter and Saturn, although observed in *Planck* data, are too bright and hence affected by detector nonlinearities). Compared to previous data releases, this new calibration scheme amounts to a decrease in flux densities of 15% and 7% at 545 and 857 GHz, respectively.

Various techniques have been used to evaluate the relative (intra- or inter-frequency) and absolute calibration accuracy (Planck Collaboration VIII 2014; Planck Collaboration XV 2014). Results are summarized in Table 4. The main limitations on the photometric calibration accuracy that we have identified result from the residual nonlinearities for low frequency channels, and from the accuracy of the models of planetary brightness at 545 and 857 GHz.

For this data release, the zero levels of the maps, which *Planck* cannot determine internally, have not been set. Still, we estimate in Planck Collaboration VIII (2014) a Galactic and an extragalactic zero level (Tables 4 and 5). For the Galactic case, we compute the map brightness corresponding to zero gas column density as traced by the 21 cm emission from neutral hydrogen. For the monopole term of the CIB, we use an empirical model, which can be used to enable total emission analysis. These estimates can be used to set the appropriate zero levels of HFI maps and are also summarized in Table 4.

6.3. Overview of HFI map properties

Figures 15 to 20 show the sky maps constructed from HFI data. These correspond to maps uncorrected for zodiacal light emission and far sidelobe pick-up (discussed in the next section). The top row of the figure series shows the intensity maps reconstructed from the nominal mission, while the second row shows the difference between maps made from the first and the second halves of each stable pointing period (i.e., half-ring maps), which provides visual information on the level and distribution of the residuals, since these maps illustrate the difference between maps constructed from rings taken about 20 min apart; therefore they illustrate the variation of the detector signal along a sky circle on such a timescale, which certainly dominates the rms. Longer timescale variations can be judged from the third row of plots showing the difference in the sky between the Survey 1 and Survey 2. This time one sees variations on a six-month time scale, which maximizes systematic effects by comparing measurements taken with a different scan orientation of the satelitte. Note that for 100−217 GHz, the colour scale of the second row is enlarged by a factor of 75, by 200 at 353 and 545 GHz, and by a factor of approximately 730 at 857 GHz.

The distribution of integration time per channel is shown in Fig. 21. The map noise properties may be evaluated from variance maps computed from the integration time per pixel, but a better approach uses the half-ring map differences (middle row of Figs. 15 to 20), which gives a better rendition of the noise at map level due to the non-white structure of the timeline noise after time-response deconvolution. In Fig. 22 we show the angular power spectra of these differences, for each frequency. With respect to the *Planck* early data release, these noise spectra are notably flatter at high ℓ, thanks to the use of a better low pass filter in the TOI processing (although the 100 GHz channels still show a rise at high ℓ due to imperfect deconvolution). The figure also shows the spectra of the differences between maps made from the first and second sky surveys (bottom row of Figs. 15 to 20), giving an indication of the contribution to the noise from longer timescales. The two sets of spectra converge at high ℓ.

The average of the half-ring power spectra from $\ell = 100$ to 6000 are reported in Table 4. One should note, however, that the half-ring maps give an estimate of the noise that is biased low (by a couple of percent), due to small correlations induced by the way the timelines have been degliched. This is discussed in detail with the help of simulations in Sect. 7.2.2. Estimates of the noise level from the timelines and from the maps were discussed in Sect. 3.10 and given in Table 2. They are consistent with alternative descriptions of the noise that were computed in the HFI calibration and mapmaking paper (Planck Collaboration VIII 2014). The summary in Table 4 (lines *c1*−*c2*) gives sensitivity levels derived from these analyses.

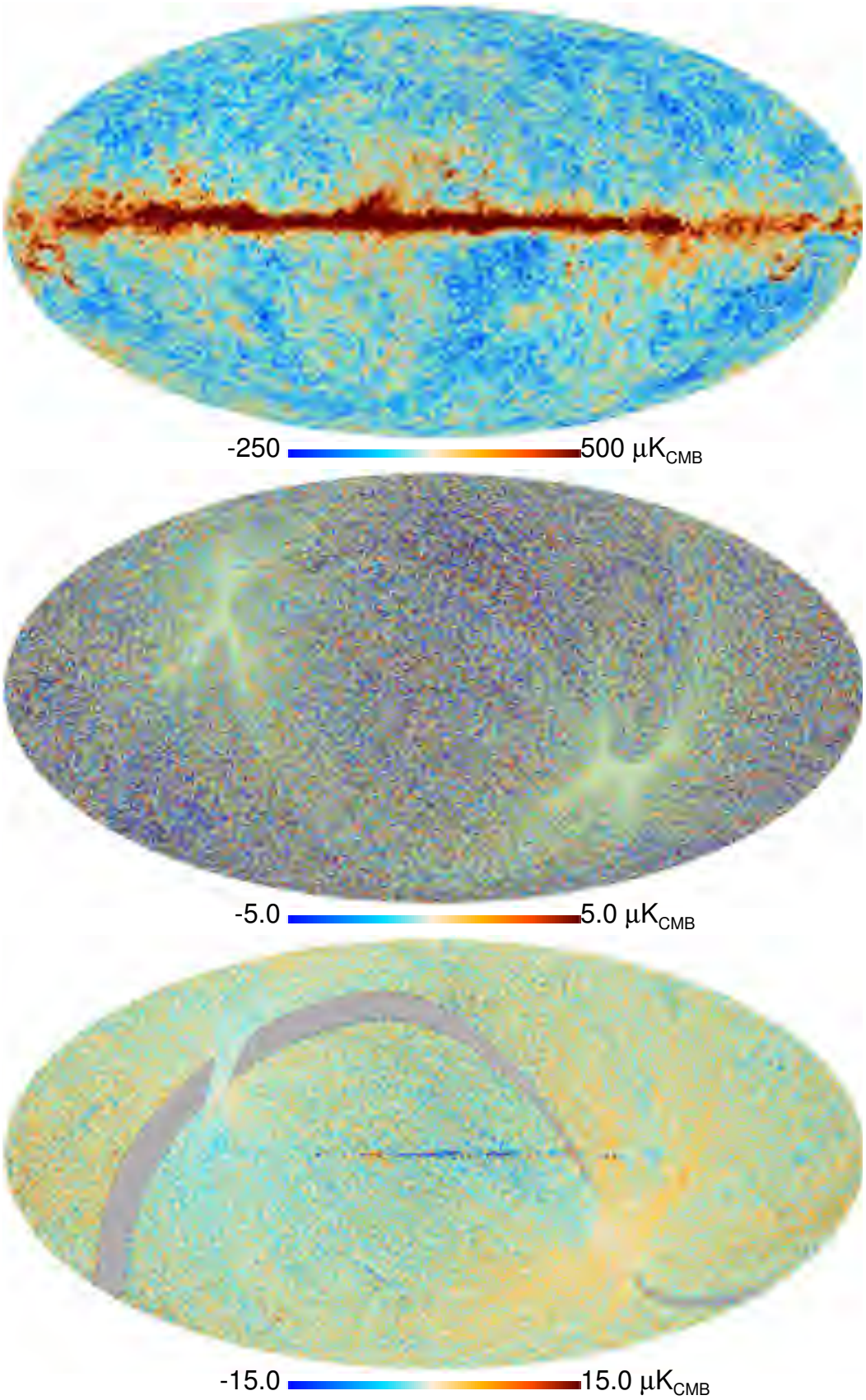

Fig. 15. HFI maps at 100 GHz. The *top panel* gives the intensity in μK_{CMB}. The *middle panel* shows the difference between maps made from the first and the second halves of each stable pointing period (i.e., half-ring maps). The *bottom panel* shows the difference between Survey 1 and Survey 2.

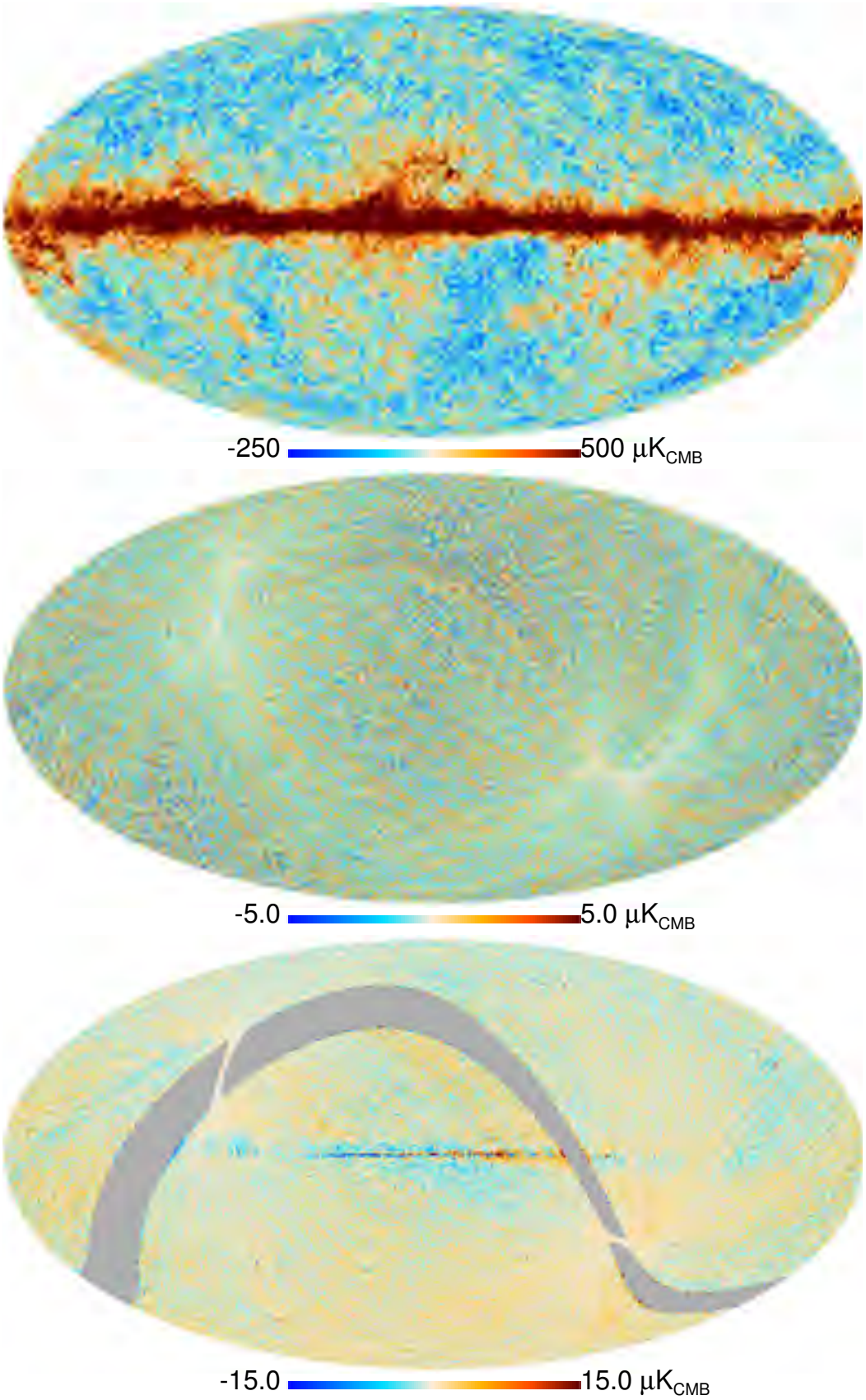

Fig. 16. HFI maps at 143 GHz. The *top panel* gives the intensity in μK_{CMB}. The *middle panel* shows the difference between maps made from the first and the second halves of each stable pointing period (i.e., half-ring maps). The *bottom panel* shows the difference between Survey 1 and Survey 2.

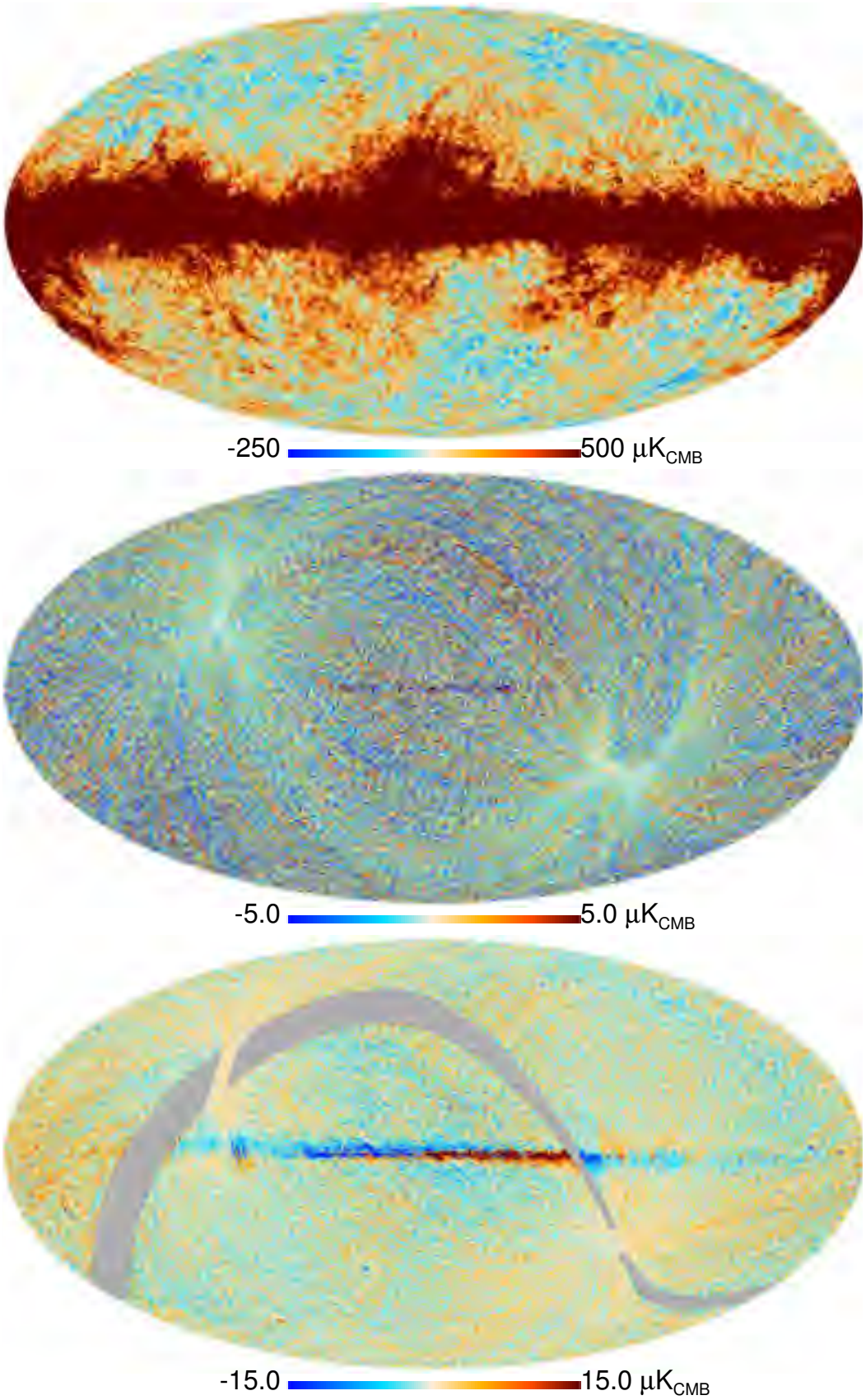

Fig. 17. HFI maps at 217 GHz. The *top panel* gives the intensity in μK_{CMB}. The *middle panel* shows the difference between maps made from the first and the second halves of each stable pointing period (i.e., half-ring maps). The *bottom panel* shows the difference between Survey 1 and Survey 2.

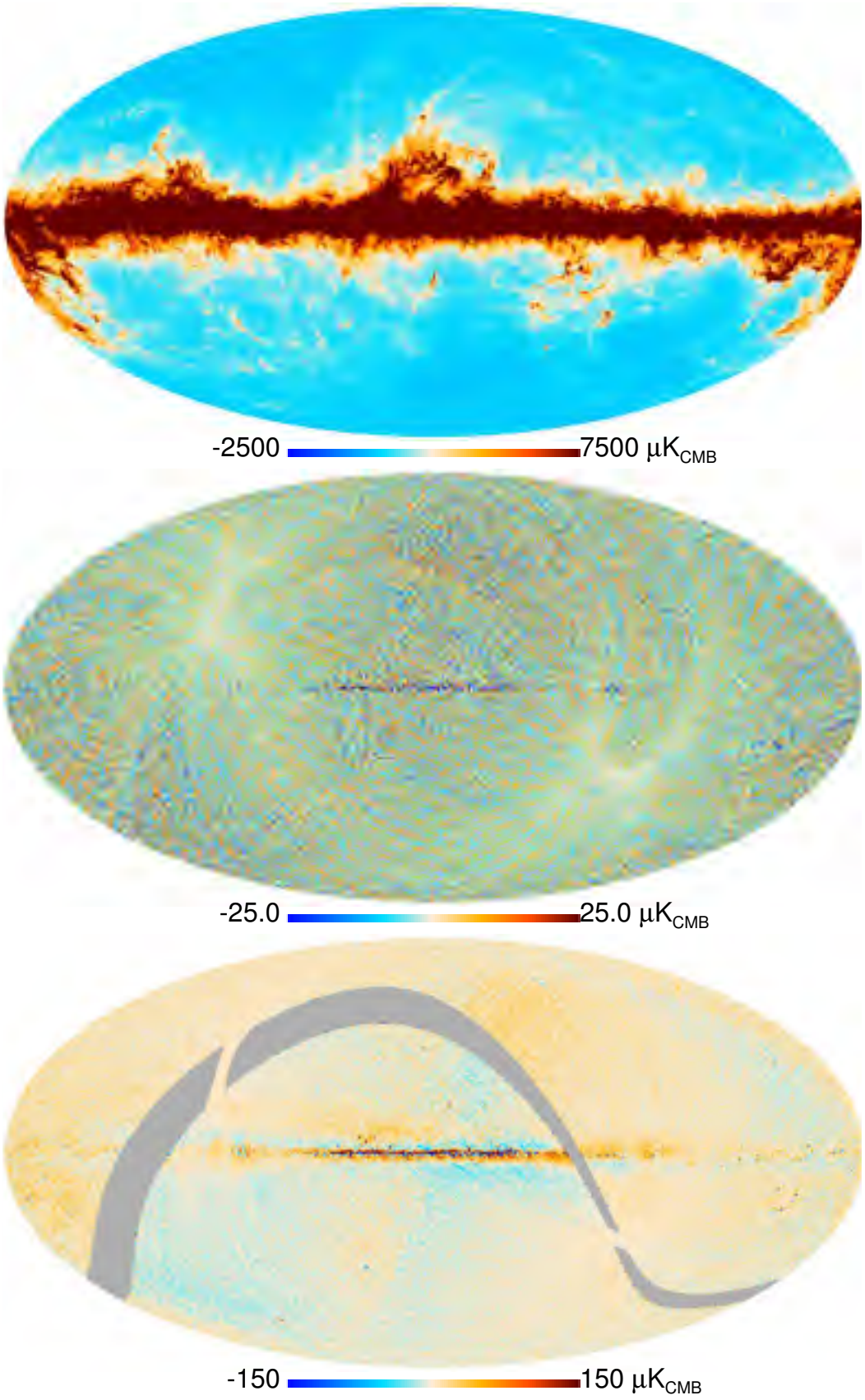

Fig. 18. HFI maps at 353 GHz. The *top panel* gives the intensity in μK_{CMB}. The *middle panel* shows the difference between maps made from the first and the second halves of each stable pointing period (i.e., half-ring maps). The *bottom panel* shows the difference between Survey 1 and Survey 2.

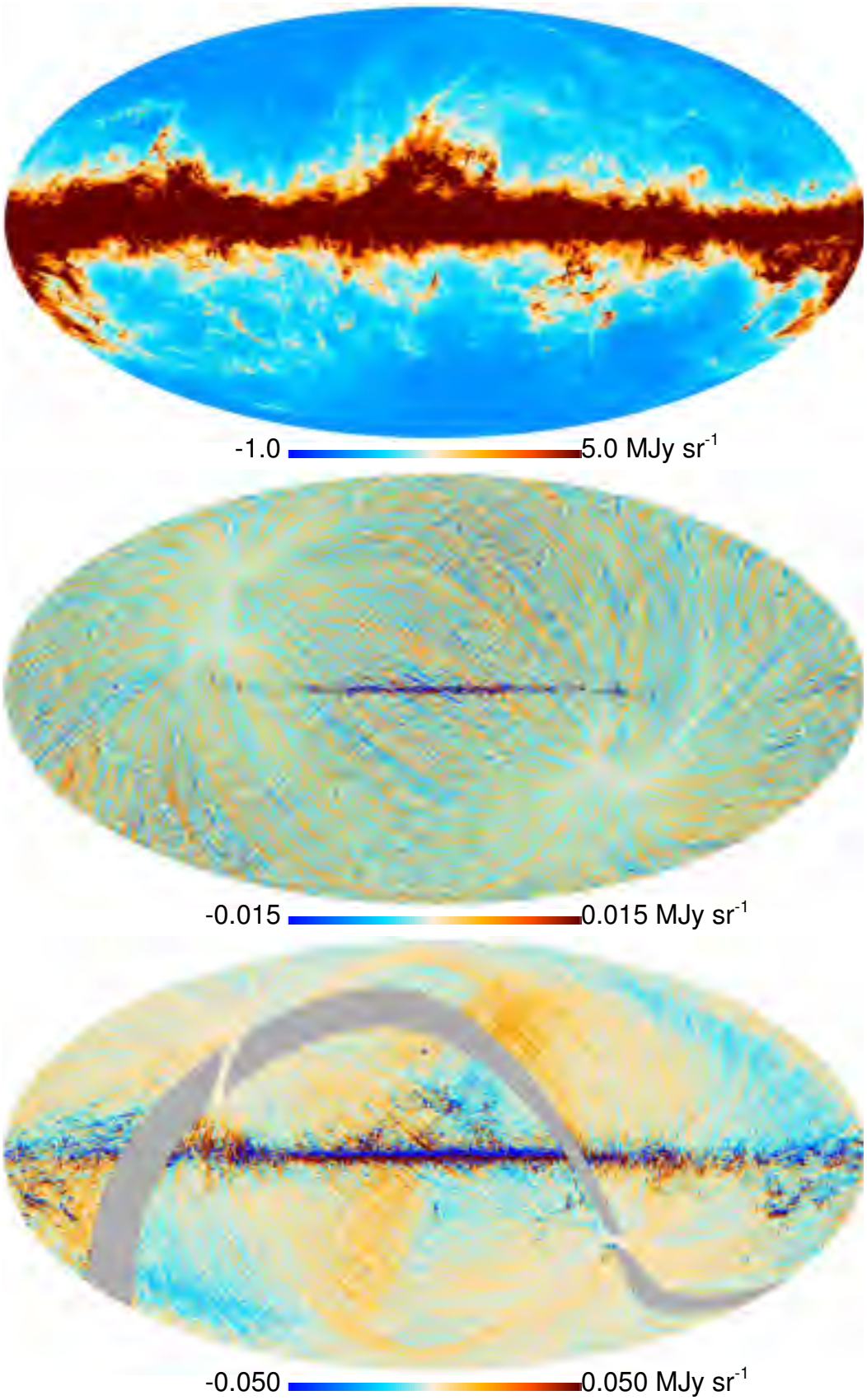

Fig. 19. HFI maps at 545 GHz. The *top panel* gives the intensity in MJy sr^{-1}. The *middle panel* shows the difference between maps made from the first and the second halves of each stable pointing period (i.e., half-ring maps). The *bottom panel* shows the difference between Survey 1 and Survey 2.

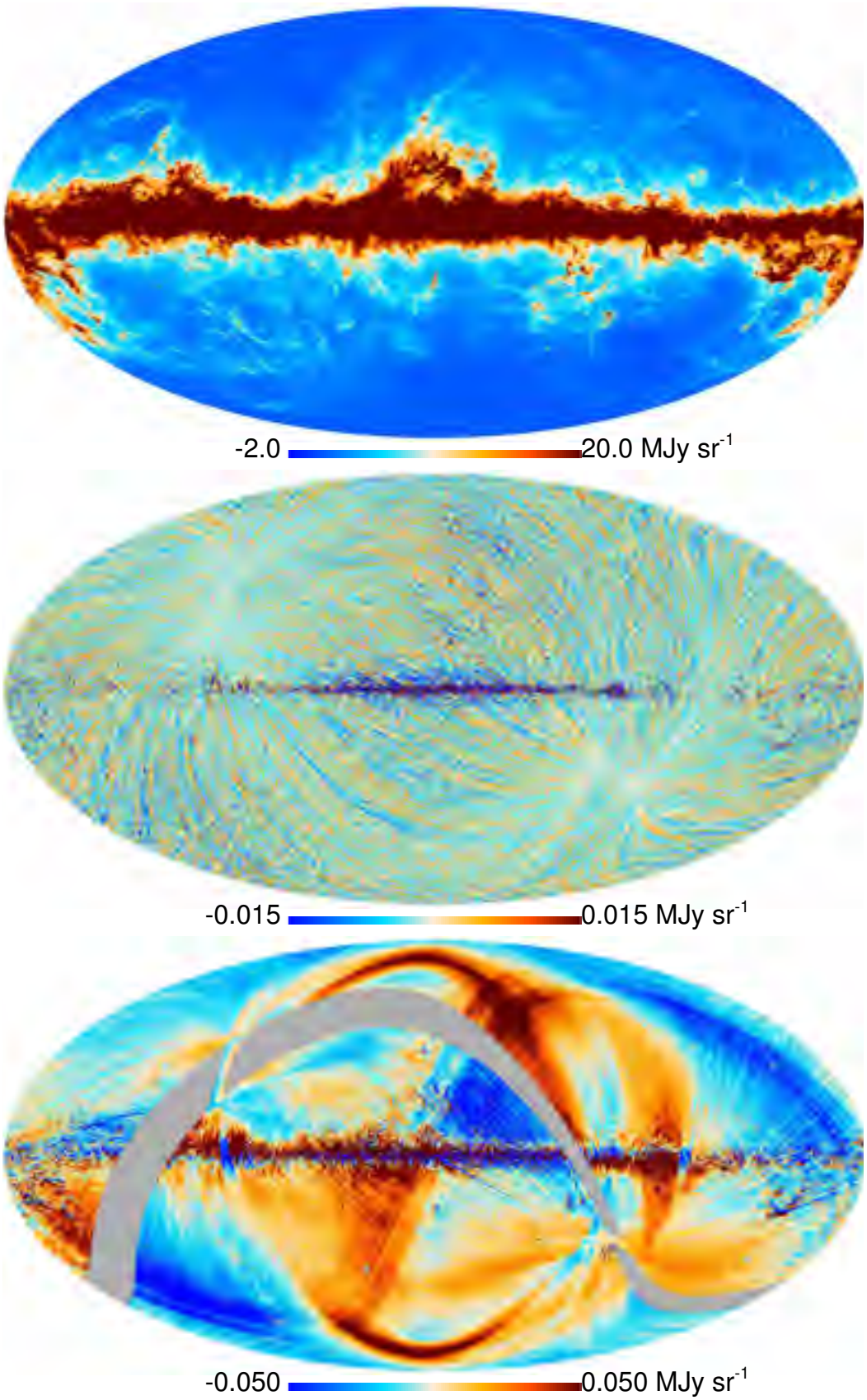

Fig. 20. HFI maps at 857 GHz. The *top panel* gives the intensity in MJy sr^{-1}. The *middle panel* shows the difference between maps made from the first and the second halves of each stable pointing period (i.e., half-ring maps). The *bottom panel* shows the difference between Survey 1 and Survey 2.

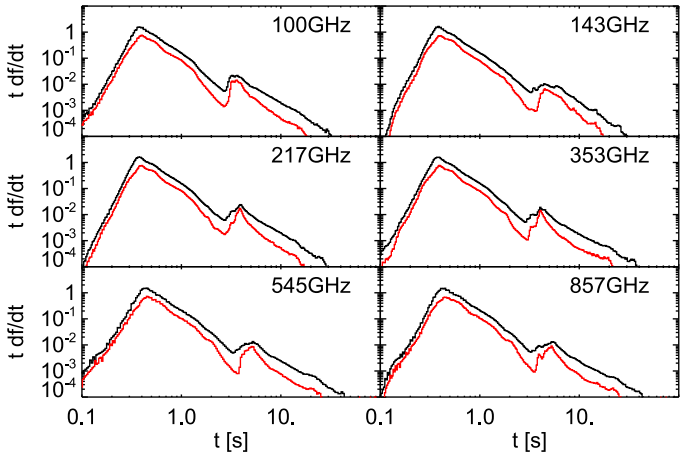

Fig. 21. HFI channel integration time distribution function. For each HFI channel, the histogram of the integration time t per pixel of area $(1.7')^2$ is shown. The black curve is for the nominal all-sky ($f_{\rm sky} = 1$) mission. The red curve represents the masked sky, using the CL39 ($f_{\rm sky} = 0.48$ for the Galactic part) mask defined in Planck Collaboration XV (2014). The normalization is such that $\int {\rm d}f = f_{\rm sky}$. The median integration time is about 0.42 s whereas the mean is 0.56 s. Notice that about 0.5% of the pixels are observed for more than 5 s; these mostly lie around the Ecliptic poles.

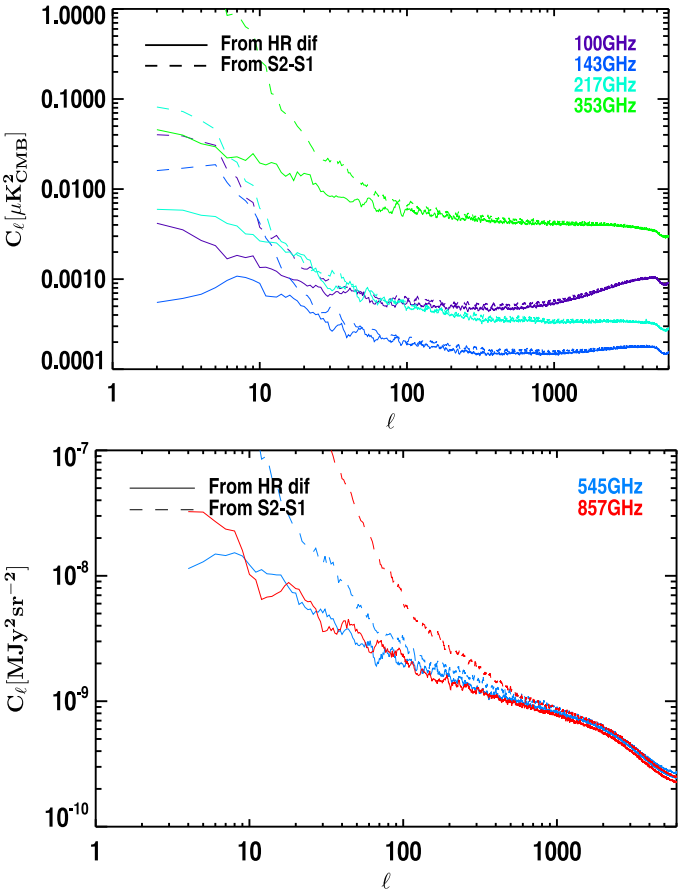

Fig. 22. Power spectra of the intensity maps reconstructed from the difference between the first and second half of each ring (denoted "HR dif"), or from the difference between Survey 1 and Survey 2.

6.4. Far-side lobe and zodiacal light correction

Most of the signals *Planck* observes on the sky are fixed to the celestial sphere. There are, however, two exceptions: zodiacal light emission (ZLE), and far sidelobe (FSL) contamination. Because *Planck* surveys the sky twice per year with a "cycloidal" scanning strategy (Dupac & Tauber 2005), each time a given location on the (distant) sky is observed, a different column of nearby dust in our Solar System is sampled, leading to a slightly different ZLE (see Planck Collaboration XIV 2014). The signature of zodiacal emission is indicated by the "S"-shaped band along the Ecliptic plane seen in the 857 GHz difference between maps made six months apart (bottom row of Fig. 20), when *Planck* is located at antipodal points in its orbit and therefore looking through very different columns of zodiacal dust. Figure 23 shows the sky pattern of the ZLE model in each of the HFI bands.

In addition, there is a small, asymmetric, off-axis beam response that also leads to additional time variability. This is seen as the arcs near the north and south Galactic poles in Fig. 20. Both of these are most pronounced in the highest-frequency channels. We remove these signals so that further Galactic and extragalactic studies will not suffer from interplanetary dust emission.

The removal process is described in more depth in Planck Collaboration XIV (2014). It consists of fitting survey maps from each horn to the COBE zodiacal emission model (Kelsall et al. 1998) to find the emissivities at the HFI wavelengths, plus templates for the Galactic and dipole signal seen through a model of the far sidelobes. With the amplitudes for each template from this fit, we again turn to the COBE and far-sidelobe models to reconstruct the implied zodiacal emission at all times during the survey for each individual detector. We convert the values to $\mu K_{\rm CMB}$, and remove these signals before the data are combined into maps.

The fit coefficients for the zodiacal emission are presented in Planck Collaboration XIV (2014), as are representative maps of the amount of signal removed from each map, and the power spectra of these maps. At 143 GHz, the zodiacal emission consists essentially of a band of emission between Ecliptic latitudes of roughly ±15°, reaching a maximum of 5 $\mu K_{\rm CMB}$. The power spectrum at 143 GHz is small: it appears only at multipoles less than roughly 75, and expressed as $(2\pi)^{-1}\,\ell\,(\ell+1)\,C_\ell$ is everywhere less than 2.5 $\mu K^2_{\rm CMB}$ for all multipoles (and even smaller if multipoles are binned).

Maps are made available both with and without ZLE removal. In addition, as there is a detection of the Galaxy seen through the far sidelobes in some horns at 857 and 545 GHz, these signals are removed as well, for these frequencies only, along with ZLE removal. Figure 23 shows the sky map of the signal removed, and Fig. 24 shows its power spectrum at 100−353 GHz, separately for odd and even multipoles, reflecting the approximate north/south symmetry of the pattern. The correction is much less uncertain at the three highest frequencies, but the low-frequency spectra allow us to gauge the rough level of the contribution to the low-ℓ power spectra in uncorrected maps. At $\ell \geq 50$ the ZLE contribution in uncorrected maps is smaller than 1 $\mu K^2_{\rm CMB}$ and can thus be neglected. But in order to extract the CMB, we found that one cannot use only a partial correction of the ZLE at the frequencies where it is well determined, i.e., at 353 GHz and higher frequencies, since lower-amplitude "S"-shaped residuals (in the CMB map) are found when the corrected maps are used. Nevertheless, overall, we discovered that the best CMB cleaning was achieved by using the full multi-component CMB and foreground separation process itself on maps not otherwise explicitly corrected for the

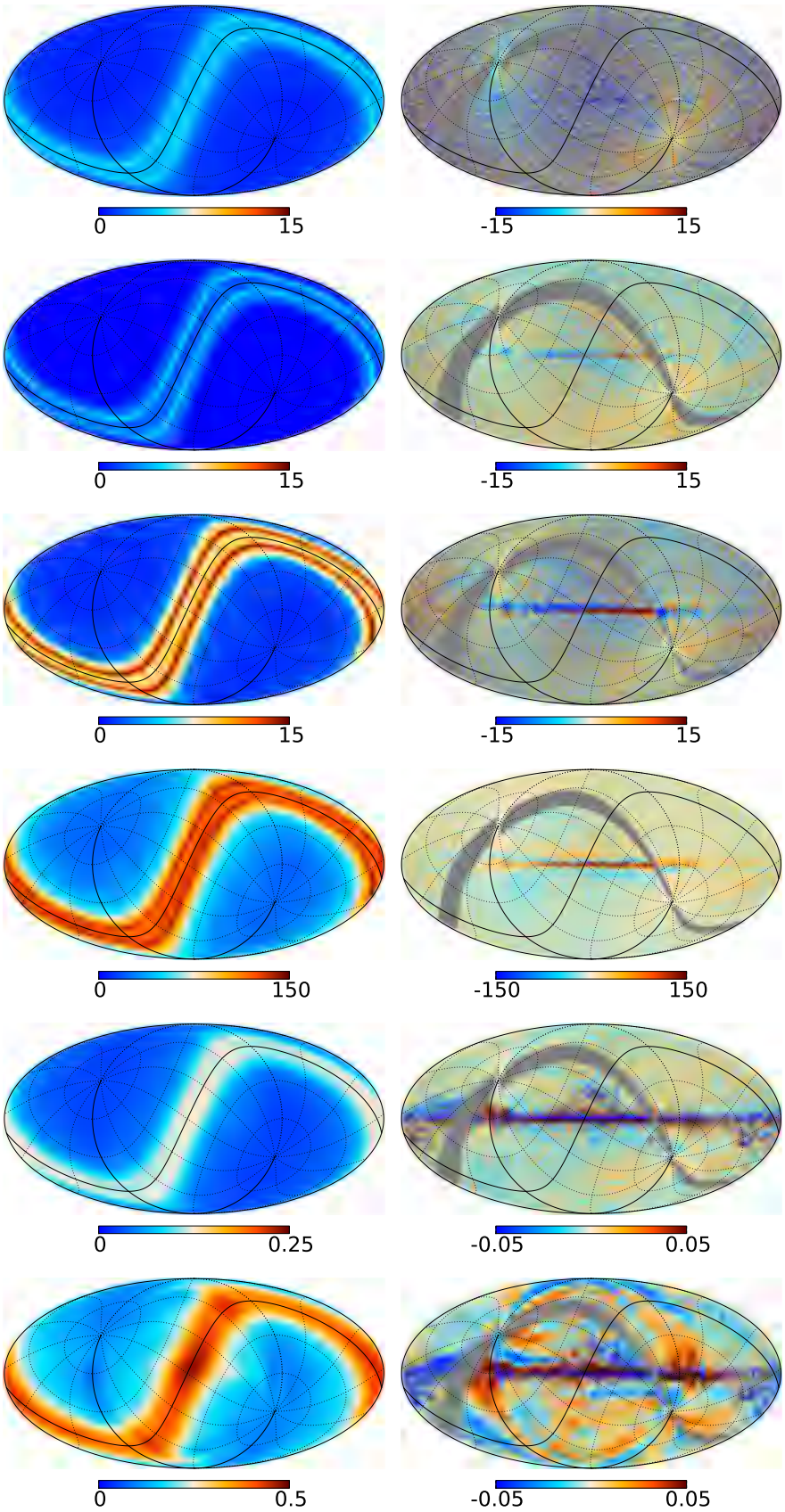

Fig. 23. Zodiacal light contribution in HFI channels, with 100 GHz to 857 GHz *from top to bottom*. Units are μK_{CMB} for 100−353 GHz and MJy sr^{-1} for 545 and 857 GHz. *Left column*: estimate of the correction. *Right column*: the Survey 1−Survey 2 difference map after correction, which can be compared with the bottom row of Figs. 15 to 20. While there is no visible difference in the CMB channels, note the improvement to the 353−857 GHz maps.

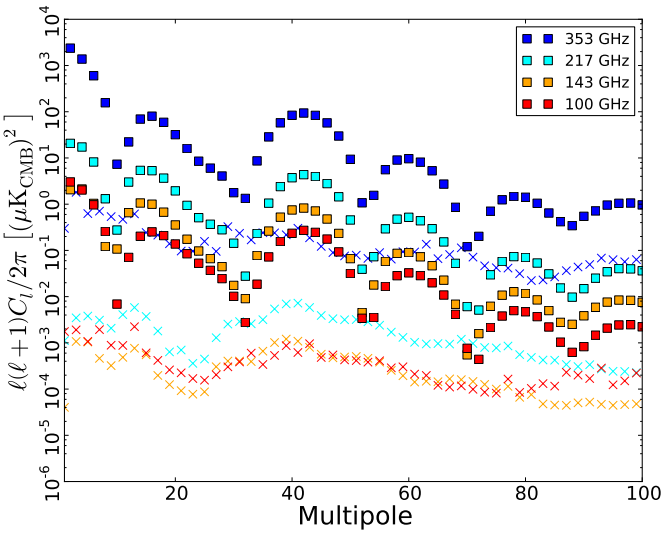

Fig. 24. Angular power spectrum of the zodiacal light contribution from each channel. Even multipoles are shown with filled boxes, odd multiples with crosses. The systematic difference reflects the approximate north/south symmetry of the zodiacal contribution. Spectra of other channels are given in Planck Collaboration XIV (2014).

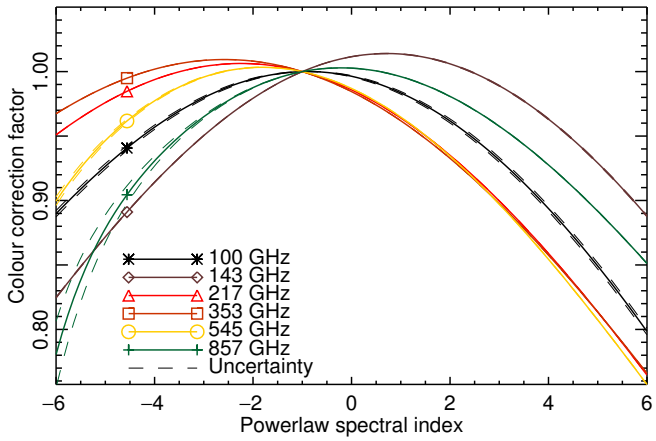

Fig. 25. Band-averaged colour correction for various power-law frequency spectra, normalized to spectral index −1. The dashed lines provide estimates of the uncertainty of these corrections.

ZLE. This is addressed in more detail in Planck Collaboration XII (2014), but the main reason can be seen right away: the relative weights of the maps that are used to generate a CMB map are found to be the same when one set of HFI maps or the other is used, and for the NILC component-separation technique described in Planck Collaboration XII 2014 are given by: 30 GHz: −0.01; 40 GHz: −0.04; 70 GHz: −0.16; 100 GHz: −0.22; 143 GHz: 1.2; 217 GHz: 0.33; 353 GHz: −0.11; 545 GHz: 3×10^{-4}; and 857 GHz: 1.8×10^{-5} . The typical peak-to-peak amplitude of the zodiacal correction is: 70 GHz: $6\,\mu K^2$; 100 GHz: $6\,\mu K^2$; 143 GHz: $5\,\mu K^2$; 217 GHz: $15\,\mu K^2$; 353 GHz: $150\,\mu K^2$; 545 GHz: $2400\,\mu K^2$; and 857 GHz: $2\times10^{-5}\,\mu K^2$. One sees that with the above weights the 353−857 GHz contribution roughly cancels the 143−217 GHz one, while lower frequency channels have both a smaller zodiacal contribution and a smaller weight in determining the CMB map.

6.5. CO correction

Some emission from the rotational transition lines of CO is present in the HFI bands. It is especially significant in the 100, 217, and 353 GHz channels, due to the 115, 230, and 345 GHz CO transitions. This emission comes largely from the Galactic interstellar medium, mainly located at low and intermediate Galactic latitudes ($|b| < 20°$). Because of the wide spectral coverage of *Planck* (Planck Collaboration IX 2014), we are able to produce velocity-integrated CO line maps for the first three transitions $J = 1 \rightarrow 0$, $2 \rightarrow 1$, and $3 \rightarrow 2$. A complete description of the methods used, the validation tests, and the CO products are given in Planck Collaboration XIII (2014). These all-sky CO maps can be used for astrophysical studies of the interstellar medium or in component separation methods.

Given the fraction of sky used for the estimation of cosmological parameters ($f_{\rm sky} \lesssim 0.5$) and the fact that CO is significant over less than 1% of the sky for these high Galactic latitudes, simply masking the CO-emitting regions is the course of action taken in cosmological studies with *Planck*.

6.6. Spectral bands and colour corrections

The HFI detector spectral response was determined through a series of ground-based tests conducted with the actual HFI focal plane in a simulated space environment, i.e., evacuated and cryogenic, prior to launch. During these tests, the HFI focal plane was coupled to a broadband radiation source observed through a continuously scanned polarizing Fourier transform spectrometer (FTS). The individual HFI detector responses to the modulated FTS signal, i.e., the observed interferograms, were recorded alongside that of a reference bolometer located inside an integrating sphere within the experimental setup. Multiple scans were averaged together to increase the signal-to-noise ratio of the resultant spectra and to allow an estimate of the spectral uncertainty. Standard FTS data processing techniques were employed to obtain the observed spectra of each HFI detector and that of the reference bolometer; the ratios of the detector spectra against the reference bolometer spectrum provide the relative response of each HFI detector. This method incorporates the detector throughput (i.e., l'étendue $A\Omega$, see Planck Collaboration IX 2014) in the spectral response as the reference bolometer accepts a much wider field of view, i.e., approximately 2π sr over all frequencies. The HFI detector spectral transmission data, and their frequency band-average transmission spectra, are described more fully in Planck Collaboration IX (2014) and Planck Collaboration (2013), where a description of the band-averaging scheme is also provided.

As discussed in Sect. 6.2, HFI is calibrated using the CMB dipole for the four 100−353 GHz bands, expressed in units of K_{CMB}, and using planets for the two 545−857 GHz bands, expressed in units of $W\,m^{-2}\,sr^{-1}\,Hz^{-1}$ (equivalently, $MJy\,sr^{-1}$). Following the IRAS conversion (Beichman et al. 1988), the conversion between these units of K_{CMB} and $MJy\,sr^{-1}$ assumes a spectrum with a spectral index of −1. Colour corrections thus need to be applied for all other spectra; they are provided for a variety of spectral indices (see Fig. 25) and other common spectral profiles including modified blackbodies and planetary spectra. It is thus important to ensure that data processing, e.g., component separation, is conducted in a consistent manner in units appropriate for the frequency band. The HFI policy is to operate in units of $MJy\,sr^{-1}$, as this is valid for all of the HFI frequency bands whereas K_{CMB} is only valid for 100−353 GHz. The K_{CMB} to $MJy\,sr^{-1}$ unit conversion coefficients are therefore

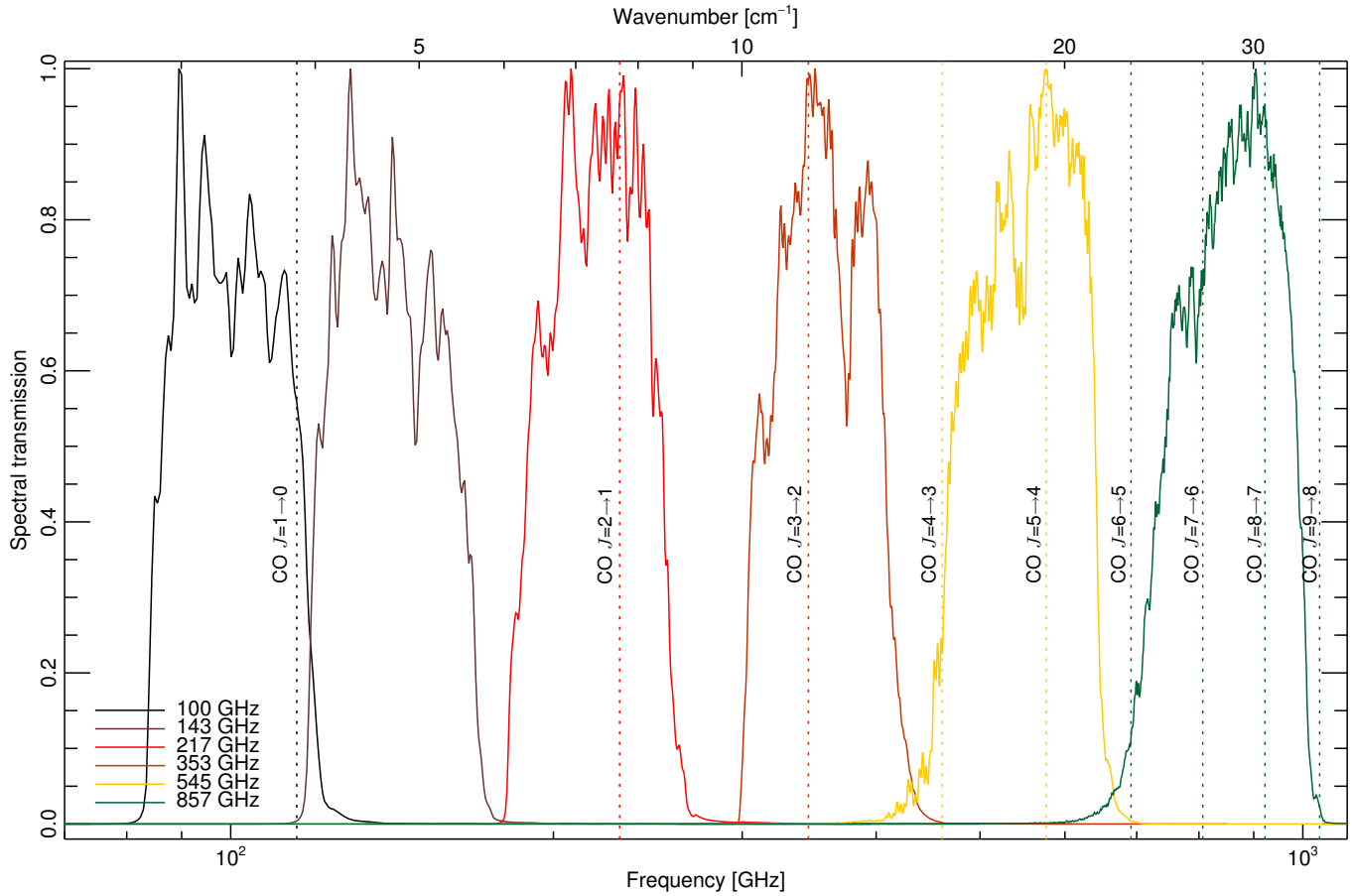

Fig. 26. Band-averaged transmission spectra for all HFI frequency bands. The locations of the various relevant CO transitions are marked with vertical lines.

given by the following ratios

$$U(\mathrm{K_{CMB}\ to\ MJy\ sr^{-1}}) = \frac{\int \mathrm{d}\nu\ \tau(\nu) b'_\nu}{\int \mathrm{d}\nu\ \tau(\nu)(\nu_\mathrm{c}/\nu)} \times 10^{20} \left[\frac{\mathrm{MJy\ sr^{-1}}}{\mathrm{K_{CMB}}}\right], \quad (3)$$

where $\tau(\nu)$ is the relevant spectral transmission curve, $b'_\nu = \mathrm{d}B_\nu/\mathrm{d}T|_{T_\mathrm{CMB}}$ is the Planck function derivative, and ν_c is the nominal band centre frequency.

Other unit conversions are also provided, to y_SZ (the Sunyaev-Zeldovich Compton parameter, discussed in Planck Collaboration XXI 2014), $\mathrm{K\,km\,s^{-1}}$ (CO transmission; see Planck Collaboration XIII 2014), and $\mathrm{K_{RJ}}$ (brightness temperature). It is important to note that brightness temperature is not restricted to a Rayleigh-Jeans spectral profile, but is a convention for an alternate expression of an arbitrary flux density in temperature units (e.g., Rybicki & Lightman 1986).

The HFI unit conversion and colour correction philosophy expresses equivalent flux density at a predefined nominal frequency depending on the spectral profile in question, rather than maintaining a set signal amplitude at a varying effective frequency, which would also depend on the spectral profile in question. This is primarily done to ease the requirements on component separation, since having all components expressed at the same effective frequency for all detectors within a frequency band is much preferred over dealing with a variety of different effective frequencies for each detector, and each component.

More details on the unit conversion factors are provided in Planck Collaboration IX (2014), while tables of conversion factors for *Planck* detectors (only HFI channels for some spectral shapes, e.g., CO lines) are provided in Planck Collaboration (2013). Figure 26 illustrates the band-averaged spectra for each of the HFI bands; similar, and related, plots for individual HFI detectors are provided in Planck Collaboration (2013).

A series of IDL scripts, called the `UcCC` routines, is available to allow users of *Planck* data to determine unit conversion and colour correction coefficients, and uncertainties, for user-specified profiles, in addition to those nominally provided in the public IMO. Further details on these scripts are provided in Planck Collaboration (2013).

6.7. Polarization

Together with the intensity maps, we derive polarization maps for each HFI frequency from 100 GHz to 353 GHz (cf. Planck Collaboration VIII 2014). The Q and U Stokes parameter maps have a nearly white noise spectrum and are dominated by Galactic dust emission and CMB with a signal-to-noise ratio of roughly 100 for $\ell < 100$. Nevertheless, at the present state of the reconstruction, polarization maps are dominated at large scales by systematic effects. As a consequence, they are not included in the present release. However, these data will be used in forthcoming analyses of foreground polarization, and hence we describe the major systematic effects remaining in the polarization data.

The *Planck* scanning strategy does not allow recovery of the polarization signal for each detector independently. We use a combination of at least four detectors oriented at 45° in order

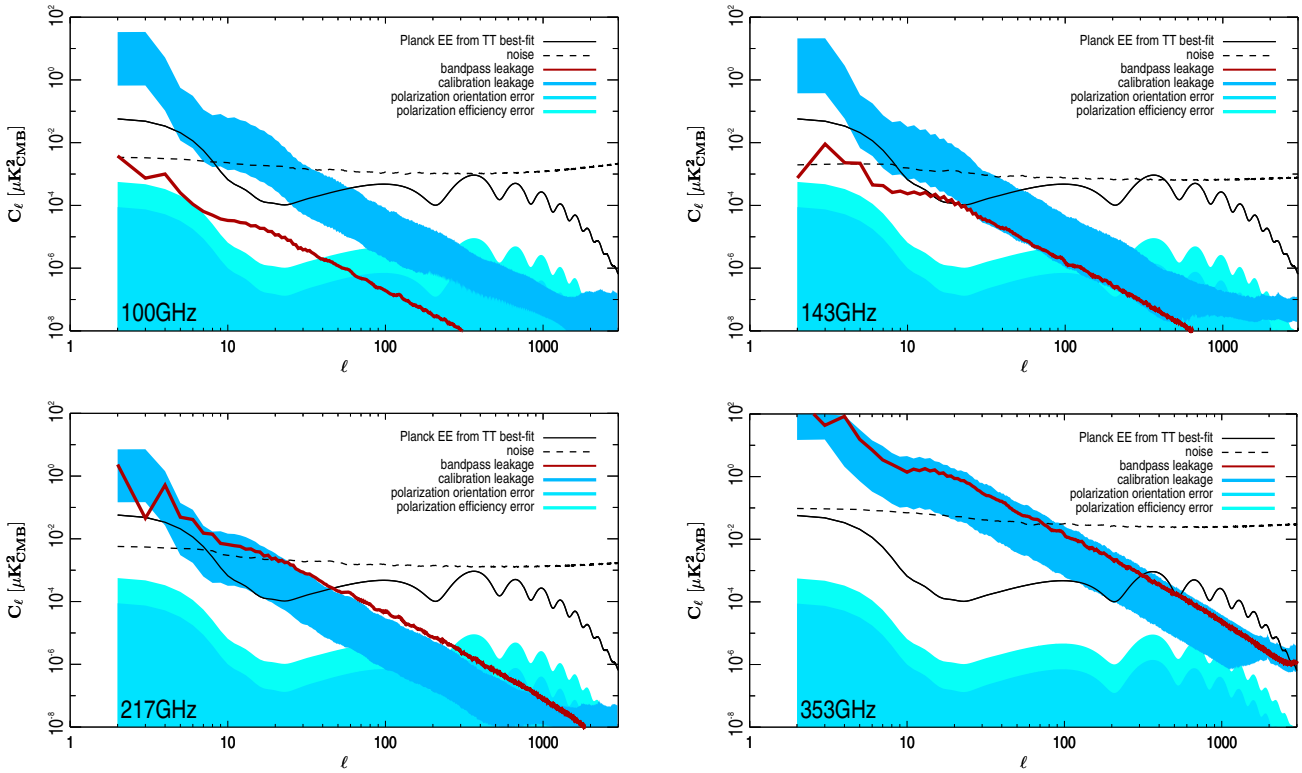

Fig. 27. Uncertainties on polarized power spectra due to residual systematics in the HFI polarization maps, compared to the *EE* spectrum predicted for the best-fit model from *Planck* temperature data.

to reconstruct the Q and U Stokes parameters. Any miscalibration between the data sets will thus lead to a mix between Stokes parameters and, in particular, a leakage from intensity to polarization. As discussed in Planck Collaboration VIII (2014), absolute calibration is derived from the solar dipole and gain variations due to ADC nonlinearities are corrected to a few tenths of a percent in the time domain. Final intercalibration uncertainties between HFI bolometers are of the order of 0.4% or less for the three lowest HFI frequencies (0.39, 0.28, and 0.21% respectively at 100, 143, and 217 GHz) and rise to 1.35% at 353 GHz. The induced leakage is dominated by the solar dipole intensity, which produces large-scale features in the polarization maps. We have estimated the leakage due to calibration mismatch using simulations. Figure 27 shows that the leakage is dominant over the CMB signal up to $\ell = 100$ in the *EE* angular power spectrum, as predicted by the best-fit cosmological parameters measured from *Planck* temperature data (Planck Collaboration XVI 2014).

In addition to the calibration mismatch, differences in bolometer spectral transmissions will also introduce a leakage from dust emission intensity into polarization. Using the spectral transmission as measured on the ground (Planck Collaboration IX 2014), we estimated the level of leakage introduced by bandpass mismatch, as shown in Fig. 27.

Polarization angles and efficiency have been assessed during ground measurements. Values and uncertainties are reported in Rosset et al. (2010). We derive uncertainties on angular power spectra using simulations for both polarization angle and efficiency independently.

Figure 27 shows the level of specific sources of error in *EE* polarization angular power spectra compared to the CMB anisotropies and the noise level (estimated from half-ring differences) computed on 90% of the sky, excluding the Galactic plane. In the polarized HFI bands (100, 143, 217, and 353 GHz) systematic errors dominate over the CMB signal at low multipoles ($\ell < 100$) due to miscalibration leakage and bandpass mismatch leakage. Polarization angle and polarization efficiency uncertainties are second-order effects. For Galactic emission polarization studies, the signal is more than an order of magnitude more intense. At higher multipoles ($\ell \gtrsim 200$), HFI polarization maps are noise-dominated but there is no evidence for correlated noise from channel to channel.

7. Data consistency and validation

7.1. Consistency with a severe selection of data

Another check based on real data consists of comparison with data in which the pointing periods have been much more severely censored. As mentioned in Sect. 3.10, the normally discarded pointing periods represent less than 1% of the total integration time for the full mission and 0.2% for the nominal mission, the difference being due to some solar flare events and the HFI end-of-life operations during the fifth survey.

Following much more severe criteria, 30% of the data of the full mission are rejected. For example, very conservative thresholds on the stationarity of the noise are applied (see the details in Appendix B). We then create a map at each frequency with this selection and compute the pseudo-spectra of both the normal and the severe selections. We show in Fig. 28 the difference between those two pseudo-spectra (red curve) and its expected 1σ envelope, as well as the cosmic variance and the instrumental noise. This difference computed at each multipole is effectively centred around zero and shows a very low absolute value compared to cosmic variance or instrumental noise (even in the [2−500] ℓ-range where it remains below a few percent).

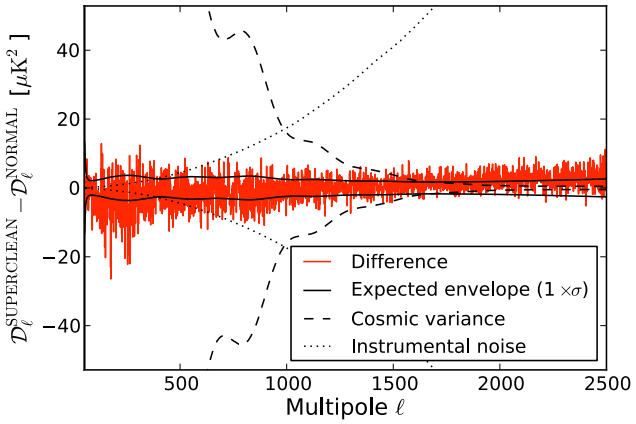

Fig. 28. The difference of the pseudo-spectra for the normal and the severe selections (in red) for the 143 GHz case. This difference is negligible with respect to both the cosmic variance and the instrumental noise (computed from FIRST × LAST half-ring differences). No binning is applied.

Some departures from ideality can be seen with the severe selection, e.g., a slight tilt in the difference spectra at high ℓ, and a higher dispersion than expected, especially at low ℓ, but these features are also present in the checks we performed. These comparisons with respect to the expected dispersion are detailed in Appendix B. This brings evidence that the level of non-stationarity of the noise during the nominal mission is negligible, and that the tilt induced by the data selection is more likely due to the variation in the structure of the hit map than to a variation in the level of a residual systematic effect.

7.2. Difference map consistency tests

We perform a series of difference map consistency tests to evaluate the contribution of residual systematic effects to the angular power spectrum of the temperature anisotropies. We generate difference maps of halves of the nominal mission data in which the signal is expected to fully subtract out in the absence of systematic effects. The resulting maps are then subtracted from systematics-free simulated "Yardstick" realizations (Appendix A) of the same differences propagated through the same mapmaking pipeline as that used for data processing. The amplitude of the power of the remaining signal in each likelihood bin can thus be used as an estimate of the level of the residual systematic contamination in this bin. This estimate is derived from cross-spectra between different detector sets to allow for a direct comparison with the spectra used as inputs by the likelihood code (Planck Collaboration XV 2014).

Many differences of halves of the data can be expected to be compatible with an absence of signal. Given *Planck*'s scanning strategy, we expect the bulk of the remaining systematic contamination to be captured in survey difference maps. In particular, transfer function errors, far-sidelobe pickup, gain instability, pointing drifts, and residual glitches will leave an imprint in these maps. Half-focal-plane difference maps will be particularly sensitive to relative gain errors, while also providing some sensitivity to sidelobe pickup. Finally, difference maps obtained by subtracting PSB-only from SWB-only sky maps probe any unexpected behavioural difference (e.g., beam mismatch) between PSBs and unpolarized dectectors, and provide a check of the (I, Q, U) decomposition applied to the data from the former. Bandpass difference misestimation between the two detector technologies will also leave a signal in these maps.

Since the survey difference test is the most stringent difference map consistency test at our disposal, we focus the discussion in this section on the corresponding results. Indeed, we did not observe null test failures in any of our other tests from the list above. The nominal mission survey difference test results are shown in Fig. 29, while Fig. 30 shows the outcome of a suite of difference map consistency tests at 217 GHz.

In Fig. 29, the angular power spectrum of the residual signal is obtained by taking the cross-spectrum between detector sets ds1 and ds2 at each frequency (see Table 1) after application of the $f_{\rm sky} = 0.48$ mask used in the primary cosmological analysis (Planck Collaboration XV 2014), combined with a mask of the regions not seen by either Survey 1 or Survey 2 and a mask of the point sources included in the input *Planck* Sky Model (PSM; Delabrouille et al. 2013) maps. The resulting sky fraction is 0.30 at 100 GHz, and 0.29 at both 143 GHz and 217 GHz. Results are then binned according to the likelihood binning. For clarity, bins at multipoles higher than $\ell = 60$ are grouped in sets of four, whereas those at $\ell > 1250$ are grouped in sets of eight. The plot at left shows the residual signal over the whole range of multipoles used in the likelihood analysis. At right, the same results are shown with a low-ℓ ($\ell < 200$) zoom. In both cases, we report the variance of the C_ℓ distribution in each bin as computed from the simulations.

At all three CMB frequencies, the $\ell < 200$ residuals are strikingly small, never exceeding about $0.5\,\mu$K^2. Excluding a single bin in each case, the residuals actually remain below or at the level of $0.2\,\mu$K^2 over this range of multipoles. Although these non-zero differences are detected with very high statistical significance, they are many orders of magnitude smaller than the binned sample variance (shown in black in Fig. 29) at these scales. In particular, they cannot affect the cosmological analysis. This stays true all the way up to $\ell \sim 1000$, at which point residuals become higher than the binned sample variance at 100 and 217 GHz. At 143 GHz, this does not happen until $\ell \sim 1500$.

In the multipole range from 1000 to 2500, although the amplitude of the residuals is almost always greater than the binned sample variance, the variance in the simulation results is significantly larger than in the $\ell < 1000$ regime. As a result, the 100 and 143 GHz residuals for that range of multipoles are fully compatible with zero. However, the 217 GHz residuals in the same multipole range are not, as can be directly inferred from the plot, where an apparently significant oscillatory feature starts at $\ell = 1000$.

This survey-difference test has been performed at each frequency for all combinations of the input maps used in the likelihood analysis (two at 100 GHz, five at 143 GHz, and six at 217 GHz), and for two survey differences: Survey 1 − Survey 2 and Survey 1 − Survey 3. In addition to the 217-ds1 × 217-ds2 cross-spectrum shown in Fig. 29, only two other cross-spectra fail this test, namely 217-1 × 217-ds2 and 217-1 × 217-3. We have evidence that these failures result in part from a systematic feature at $\ell \sim 1800$ mitigated by additional data flagging to reduce the effect of electromagnetic interferences from the 4 K cooler drive and the read-out electronics (see Sect. 3.6). In the likelihood analysis (Planck Collaboration XV 2014), we have checked (cf. Figs. 24 and 25) that the inclusion, or not, of these three cross-spectra has no discernible influence on the determination of all basic CDM cosmological parameters (but for a slight broadening of the posterior distribution, while the main foreground parameter change is a shift of the point source amplitude at 217 GHz).

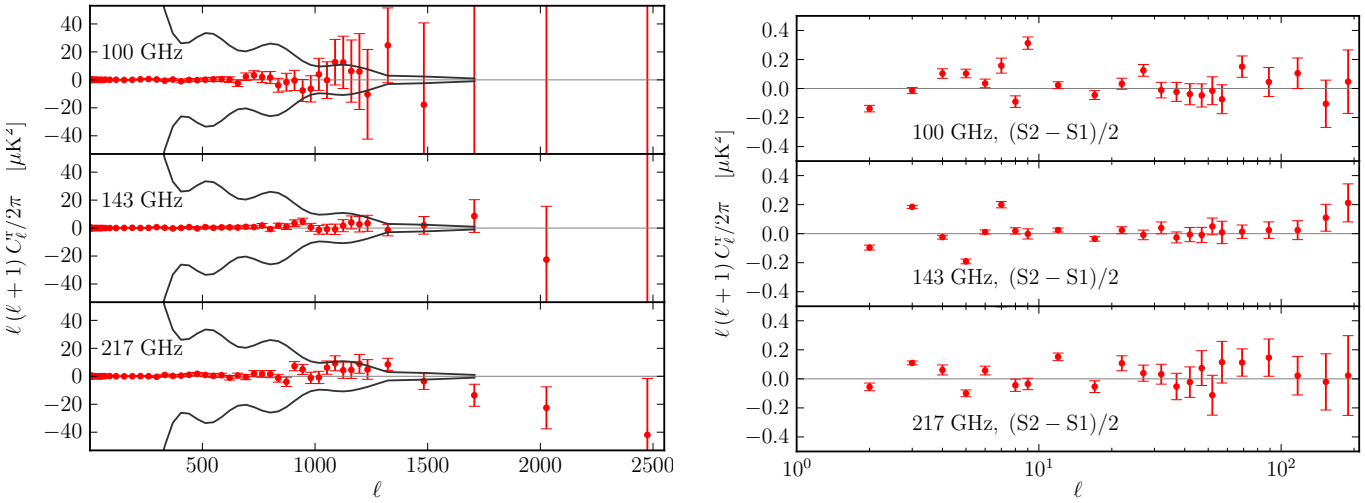

Fig. 29. (Survey 2 − Survey 1)/2 consistency test result from the ds1 × ds2 cross-spectra at 100, 143, and 217 GHz, with the $f_{\rm sky} \simeq 0.30$ mask derived from that used in the primary cosmological analysis (see text). *Left*: the residual signal in each bandpower up to the highest multipole used in the likelihood code (Planck Collaboration XV 2014). For clarity, the bins used in the likelihood analysis are grouped in sets of four for $\ell > 60$ and sets of eight for $\ell > 1250$. We show in each bin the variance of the C_ℓ distribution from the simulations. Note that the amplitude of the residual signal is under the binned sample variance envelope expected for the $f_{\rm sky} \simeq 0.30$ mask (shown in black) up to $\ell \sim 1000$ at all three frequencies. *Right*: zoom-in on the low-ℓ part of the spectrum, showing that although the difference test failures are highly significant at these scales, their amplitudes at all three CMB frequencies are less than about $0.5\,\mu$K^2 for all multipoles up to $\ell = 200$, which is a tiny fraction of the binned sample variance at these scales.

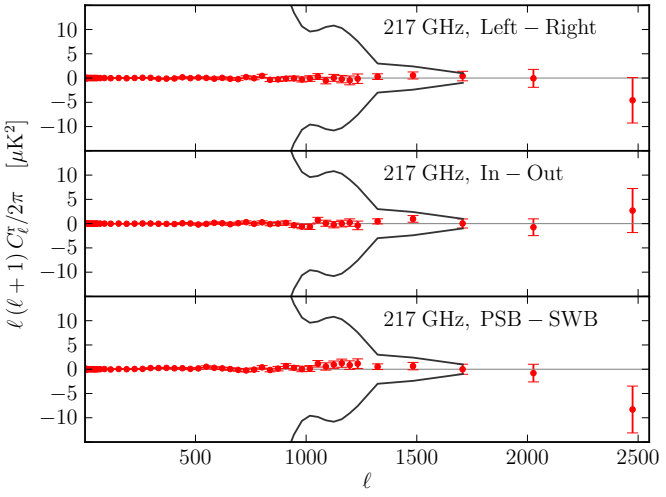

Fig. 30. Examples of map difference consistency tests at 217 GHz with the $f_{\rm sky} \simeq 0.30$ mask, derived from that used in the primary cosmological analysis (see the text). The range of multipoles shown and the binning used are identical to those described in Fig. 29. We again show in each bin the variance of the C_ℓ distribution from the simulations, and in black the binned sample variance for our mask. "Left" and "Right" refer to the two halves of the focal plane, whereas "In" and "Out" refer to detectors toward the centre and the periphery of the focal plane. Unlike in the survey difference test shown in Fig. 29, no significant null test failure is detected here. The detector combinations used in the example plots above are (5−8) × (1−4), (7−8) × (3−4), and (ds1 − 3) × (ds2 − 4) for, respectively, the (Left−Right), (In−Out), and (PSB−SWB) tests. As in Fig. 29, these power spectra are divided by four to allow for a direct comparison of the amplitude of the residuals to that of the components in the nominal mission power spectrum.

Finally, to best address any remaining concerns about systematic errors resulting from data selection and differences in the first-half and second-half spectra, we present additional, high precision, tests of systematics performed since the March 2013 data release on the 217 GHz *Planck* channel. Indeed, this channel has the highest angular resolution within the "CMB frequency" range 100−217 GHz used for most of the cosmological results. As a consequence, it has the least degree of redundancy of the CMB frequencies, since one cannot cross-check the 217 GHz spectrum with the lower frequency spectra at high multipoles ($\ell \gtrsim 2000$). Appendix C presents tests of the fidelity of the *Planck* power spectra using additional data from the full mission (29 months, 4.8 sky surveys, with the same processing than for the nominal mission). By using the full mission it is possible to perform more extensive and higher signal-to-noise tests than those described by Spergel et al. (2013), which were based exclusively on the 2013 nominal mission data release. Reassuringly, the outcome lends further support to the claimed robustness and accuracy of the cosmological results based on the current processing of HFI data.

7.2.1. ADC nonlinearity impact

We check the impact of including the effect of ADC nonlinearity through a comparison of data and simulations of the two PSB pairs at 143 GHz. Note that this effect had been suspected to be detectable, but is partially degenerate with time-dependent gain variations in the detectors. Beyond correcting for such gain variations, the effect was not accounted for in the nominal mission products, nor included in the corresponding Yardstick simulation, since the relevant modelling information was only obtained after the end of the HFI cryogenic phase through dedicated data gathering during the warm phase. Figure 31 shows that the inclusion of this effect leads to similar $\ell \lesssim 100$ deviations from the Yardstick compared to those observed in the survey difference consistency test of the 143 GHz data, which suggests this is one of the main limiting factors for measuring the low-ℓ polarization with the current processing of the data. The inclusion of this effect makes little difference at higher ℓ.

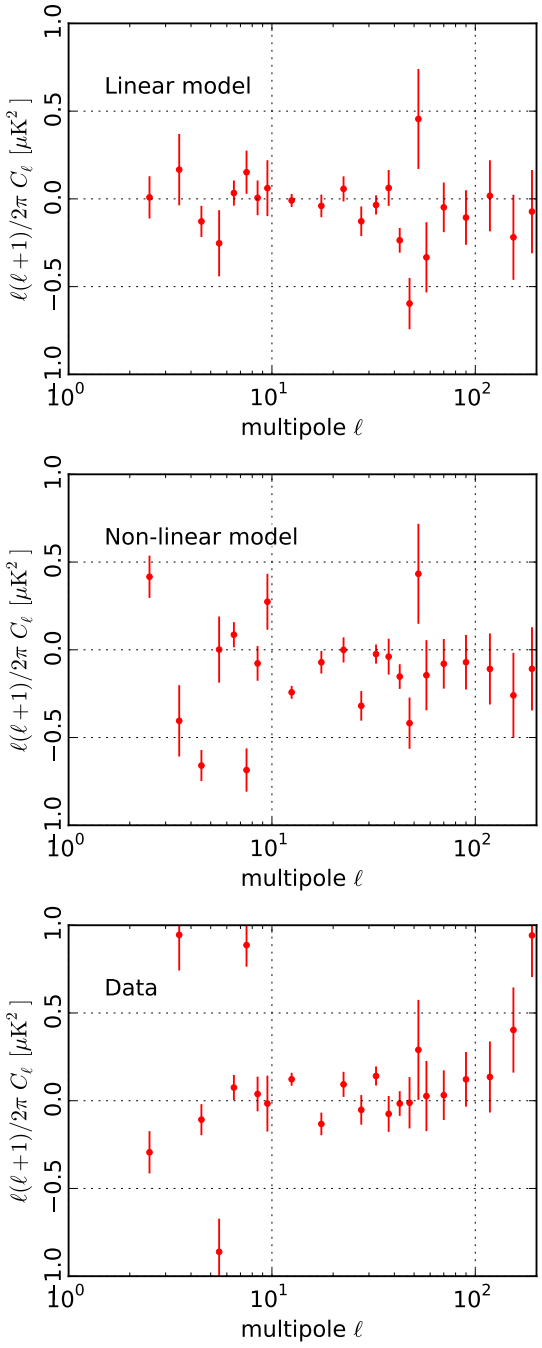

Fig. 31. Simulated effect of the ADC nonlinearity on the Survey 1 – Survey 2 difference at 143 GHz. *Top*: difference test of a single realization of the full pipeline, assuming a linear response of the ADC. *Middle*: the same, but with our current best model of the nonlinearity response of the ADC. This can be compared with the *bottom panel*, which shows the result of the test applied to the delivered data in exactly the same conditions. This demonstrates that indeed the effect of ADC nonlinearity can explain most of the coherent deviation seen at $\ell \lesssim 100$.

7.2.2. Noise estimation bias from half-ring maps

A detailed comparison of the power spectra of the sum and difference of half-ring maps shows a constant offset of a few percent at high multipoles. At these scales, there is no longer any signal remaining in the sum map, due to the beam cut-off (see Fig. 32 for an example), and we would expect that the difference map spectrum would give a precise determination of the high-ℓ tail of the sum map, while it is actually slightly below. This offset shows that a noise estimate from half-ring maps difference is a slightly biased indicator of noise in the sum maps. This results from the deglitching algorithm.

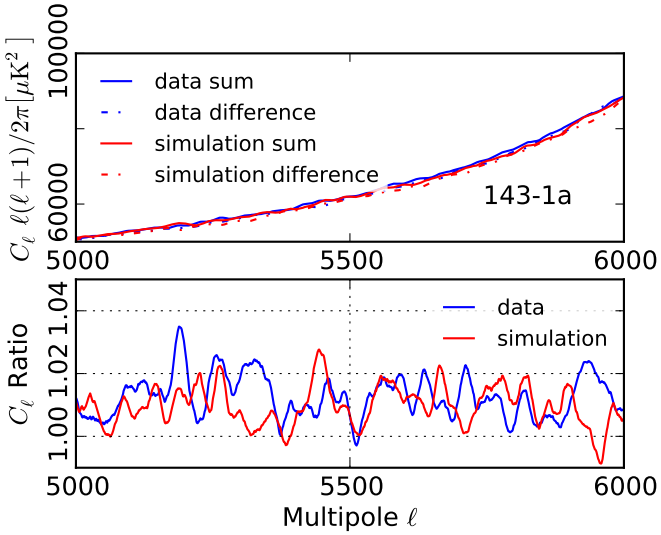

Fig. 32. Comparison of the high-ℓ part of the power spectra of the sum and difference of half-ring maps for the 143-1a detector, both for flight data and simulations where glitches were introduced and deglitched with the actual processing pipeline. The comparison shows that the simulations provide a good description of this effect (which is not included in the Yardstick simulations). *Top*: the sum and difference spectra. *Bottom*: ratios of the sum and difference spectra for both data and simulations, which differ by about 2%.

Table 3. Percentage increase of the power spectrum of the difference of half-ring maps needed to correct the bias of the noise level estimate in frequency maps.

Frequency [GHz]	Fractional change [%]
100	0.53 ± 0.08
143	0.61 ± 0.08
217	0.75 ± 0.09
353	0.44 ± 0.09

In the first step, the pipeline estimates the signal by averaging the timelines into rings. This signal estimate is removed in order to aid detection of glitches by comparison with the noise level. Each positive sample greater than three times the noise level is flagged as a glitch. One side effect of this thresholding is that the positive tail of the timeline noise distribution is now clipped at 3σ. Note that the signal estimate within a ring is of course still noisy, so that its removal from the timeline before deglitching subtracts this residual noise component periodically (coherently at all harmonics of the spin frequency), in effect periodically modulating (in both half-rings) the flagging and clipping level of the noise distribution. In the difference of half-ring maps, this common contamination disappears, while it is present in the sum map, leading to this slight bias.

Figure 32 shows that the inclusion of the deglitching step in simulations accounts quantitatively for the difference in the power spectra of the sum and difference of half-ring maps. By fitting the ratio of the spectra of sum and difference maps (masked to retain 37% of the sky) at very high ℓ (around $\ell \sim 7000$ – not shown in the figure) one finds the bias levels which are given in Table 3.

7.3. Power spectrum consistency tests

A powerful check of the data follows from assessing the signal consistency between detectors at the same frequency given the prior information on the effective beam uncertainties and calibration. At each frequency, an estimate of an adapted power spectrum model is processed with the SMICA likelihood (Planck Collaboration XV 2014). At 143 and 217 GHz where the CMB is dominant, the spectrum on the measured sky is modelled as $\boldsymbol{a}\boldsymbol{a}^\dagger + \boldsymbol{n}_\ell$, a sum of the the free signal power, C_ℓ, plus a free independent noise spectrum, $\boldsymbol{n}_\ell$, where the known vector $\boldsymbol{a}$ accounts for the fixed CMB emissivity at each frequency (bold-faced vectors have elements at each frequency). At higher frequencies, dust emission begins to dominate the CMB, and some foreground modelling is necessary. Thus the CMB power is fixed to the angular spectrum determined at 143 GHz, the noise is kept free and a free foreground is added, with colour correction determined from a greybody spectral shape integrated though the measured spectral response of each detector (40% of the sky is used to estimate the binned empirical power spectrum with spice, Szapudi et al. 2001). Furthermore, beam errors are modelled as a linear combination of templates, thanks to a beam error-mode analysis (Planck Collaboration VII 2014). Then, five beam parameters along with a calibration are estimated. The full model is written as

$$\boldsymbol{R}_\ell = \boldsymbol{B}_\ell \left(\boldsymbol{a}\boldsymbol{a}^\dagger c_\ell^{143} + \boldsymbol{b}\boldsymbol{b}^\dagger g_\ell \right) + \boldsymbol{n}_\ell \quad (4)$$

where $\boldsymbol{R}_\ell$ is the modelled spectrum, $\boldsymbol{B}_\ell$ the free beam model, $\boldsymbol{b}$ the free dust emmisivity at each frequency, g_ℓ the free dust power, and $\boldsymbol{n}_\ell$ the free noise power. The beam model for detector d is written $B_\ell[d] = \exp(\sum_q \theta^{d,q} T_\ell^{d,q})$, where θ are the beam-eigenmode amplitude parameters and T the templates. Due to the intrinsic ambiguity between spectral power and beams, beam simulations are used to determine the variances of a Gaussian prior on these parameters. Finally, at 100 GHz, with only two detector sets, three parameters per ℓ (one signal and two noise powers) allow an estimate of the empirical spectrum, but relative calibration and beam parameters estimation are then unfeasible.

Figure 33 shows the result of such an analysis. At 143 and 217 GHz, where the CMB is dominant and used as calibrator, the only adjustments necessary are a gain recalibration by a very small amount (0.2% at most) and the addition of a fraction of a σ of the first beam uncertainty eigenmode. At 545 and 857 GHz, where the CMB is subdominant and planets are used as calibrators, the required recalibration remains just as small (about 0.2%), but larger beam adjustments are necessary. The 353 GHz calibration is the one requiring the largest changes, about 1%. At 217 GHz, and to a lesser extent 353 GHz, the SWB and PSB beam window functions are at opposite sides of the "optimal" one. In conclusion, by properly modelling foregrounds at high frequency, cross-checks on signal anisotropy with 40% of the sky shows that maps are well calibrated (relatively) within a frequency band.

Figure 34 shows the magnitude of the beam corrections determined by maximizing the internal consistency for the most sensitive CMB channels of *Planck*. The largest corrections would be about $2\,\mu\mathrm{K}^2$ around $\ell \sim 100$ and about $4\,\mu\mathrm{K}^2$ around the third peak of the CMB spectrum ($\ell \sim 800$). For the delivered frequency maps, which combine all detectors at the same frequency, the effect is even weaker, and for the likelihood analysis, this is fully accounted for (these beam eigenvalues are either directly estimated or marginalized over, including in addition their expected cross-correlations as discussed in Planck Collaboration VII 2014 and Planck Collaboration XV 2014).

7.4. Consistency of the calibration across frequencies

In the previous section, we looked at the consistency of detector spectra within a given frequency band. A similar analysis of the spectra used in the high-ℓ part of *Planck* likelihood Planck Collaboration XV (2014) shows that the best relative recalibration (for the mask considered and accounting for the first beam eigenmode), between all 13 detectors maps in the 100, 143 and 217 GHz channels, would be less than 0.2%. This level has an insignificant effect on the constraints on cosmological parameters.

Finally, we can further broaden our consistency checks by using the SMICA component separation method on both LFI and HFI data from 44 to 353 GHz, in effect intercalibrating on the common CMB anisotropies themselves, taking 143 GHz as the reference (see Sect. 7.3.3 of Planck Collaboration VIII 2014 and Planck Collaboration XII 2014). Figure 35 compares the results of such an analysis[4] on a full focal-plane (FFP6) simulation (Planck Collaboration 2013) and on the 2013 maps, using a five-component foreground model. The simulations accurately validate the approach, in a realistic setting (albeit with decreasing accuracy at 44 and 353 GHz). For flight data, the multipole range over which the calibration factor is averaged has been split in two, a relatively low-ℓ range (50−300), more appropriate to include the noisier 44 and 70 GHz LFI channels, and a higher-ℓ range, (300−700), more appropriate for HFI data. The figure confirms that the 100−217 GHz map calibrations are consistent to 0.2%, as discussed earlier. The 353 GHz results would suggest a slightly higher calibration than the one we finally adopted, although the SMICA analysis does not account for the Rayleigh scattering correction (see Planck Collaboration VIII 2014) and we may also reach the limit of a five-component foreground model. This analysis also suggests a residual calibration difference between LFI at 70 GHz and HFI at 100 GHz of roughly 0.3%.

Further checks involving comparison with the LFI and *WMAP* data are discussed in Planck Collaboration XXXI (2014).

7.5. Further validation

Other tests are described in various other papers:

- Planck Collaboration XXXI (2014) compares the maps from the HFI and LFI instruments on *Planck* and from the *WMAP* satellite. We demonstrate excellent consistency amongst the three sets of maps produced with different instruments over a a factor of thirty in wavelength, and especially over the narrow range of 70−100 GHz covered by all three instruments, illustrating the excellent control of systematic errors we have achieved with *Planck*.
- Planck Collaboration XII (2014) discusses several methods for separating the various astrophysical and cosmological data. Methods with very different assumptions about the physics of the different components, and about the nature of the noise in the *Planck* maps, are able to converge on equivalent maps for different components, most importantly of the CMB itself.
- Planck Collaboration XV (2014) discusses the angular power spectrum, C_ℓ, computed from *Planck* data, as well as the likelihood function that embodies its full probability distribution. The likelihood is computed by taking into account

[4] The analysis is actually carried out over 40% of the sky, for various ℓ ranges; the results discussed here show the average in the multipole range 100−679 for the simulations.

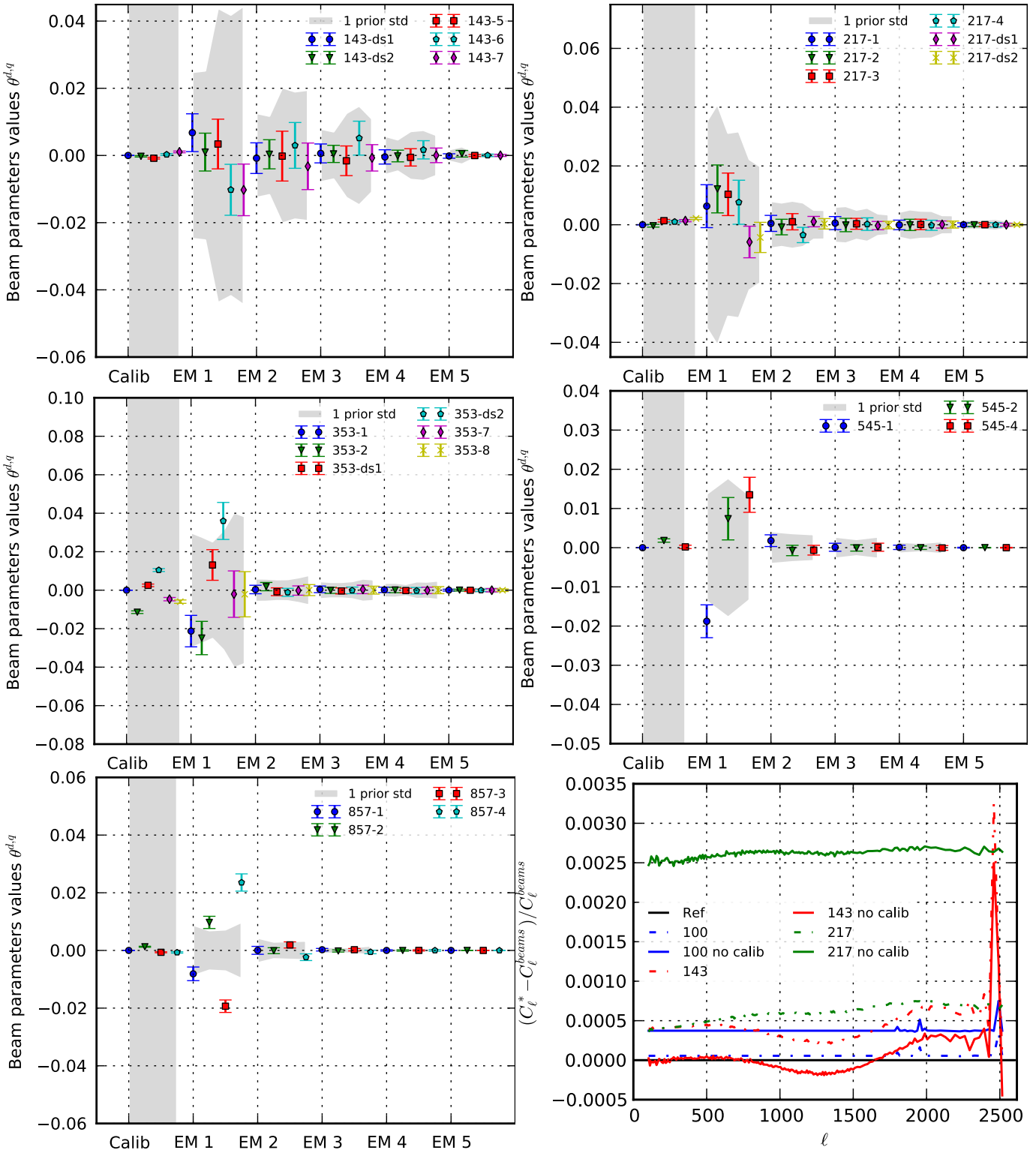

Fig. 33. Calibration ("Calib") and beam uncertainty mode ("EM") determination for all detectors (or detector sets) within each frequency band. The grey areas show the 1σ priors on each beam parameter (without assuming a prior for gain calibration; the first detector in each series is used as a fixed reference). The error bars show the 1σ posteriors. The *bottom right panel* shows the variations of the power spectra in the primary CMB channels when applying the recalibration and beam uncertainty corrections described in the text. Altogether, this leads to variations smaller than 0.4% at all $\ell \lesssim 2500$. Note that the shape variations with ℓ are much smaller (a fractional variation less than about 5×10^{-4}).

explicit models of foreground contamination and of systematic effects, such as beam errors and the relative calibration of different detectors. The resultant spectra explicitly illustrate consistency across those bands with the highest signal-to-noise ratio for the cosmological spectra at 100, 143, and 217 GHz, at the level of power spectra and of cosmological parameters. As discussed as well in 7.2, the likelihood is robust to the inclusion (or otherwise) of even the 217 GHz detectors that show some mild non-zero features in the spectra of their difference maps.

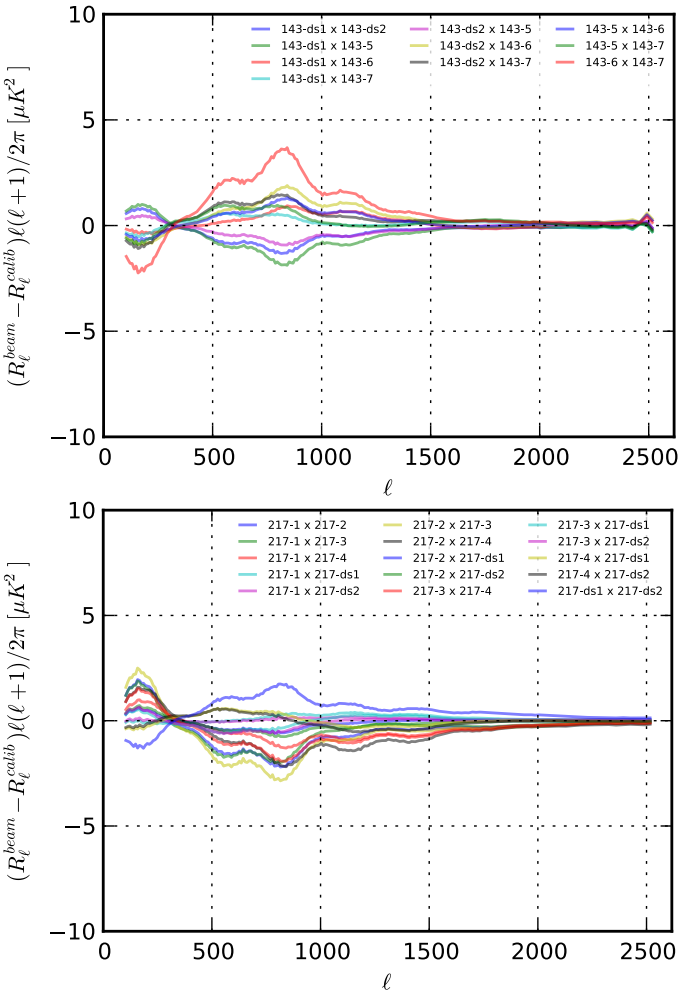

Fig. 34. Derived overall beam correction of each detector set which minimizes their mismatch, given the model used (Eq. (4)). This is plotted for 143 and 217 GHz, where there are sufficient data to simultaneously estimate beam parameters along with signal and noise power spectra. These corrections peak around $\ell \sim 200$ and 800 and are at most of the order of 3 μK^2.

8. Summary of product characteristics and conclusions

The data provided to the *Planck* collaboration and the community by the HFI DPC, in addition to the IMO, consisted of the following (letters refers to entries in the final column of Table 1).

1. C: beam-corrected power spectra for each CMB detector set used in the *Planck* likelihood code, together with a description of the relevant beam uncertainties;
2. N: frequency maps for the nominal mission duration, not corrected for ZLE/FSL;
3. B: effective beams and uncertainties (for N);
4. F: spectral bands and uncertainties;
5. H: hit count maps (for N);
6. HR: half-ring maps, HR1 and HR2, two maps made from the first and the second half of each pointing period of the nominal mission;
7. S: survey maps, S1 and S2, made from the data of Survey 1 only and Survey 2 only; and
8. Z: zodiacal light emission and far sidelobe corrected frequency maps and their survey maps (Z-N, Z-S1, Z-S2).

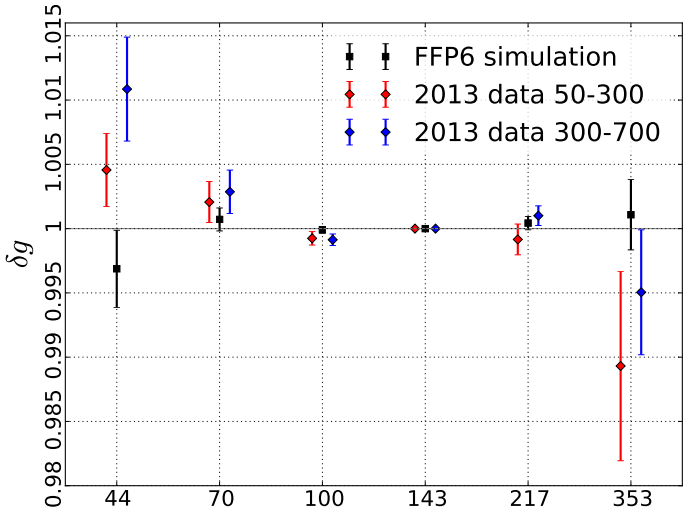

Fig. 35. Recalibration factor maximizing the CMB consistency in in simulations (black) and in the data, considering different multipole ranges (red and blue), at each *Planck* frequency in GHz (on the horizontal axis).

Table 1 summarizes the various detector sets from which we made these products, while Table 4 summarizes the map characteristics needed to make use of the maps. Further details and comments are given below.

Angular response

Effective beams provide the response of a map pixel to the sky (lines *b1*–*b7* of Table 4). They are based on a determination of the scanning beam from planet scans (Sect. 5.1), which include the effect of the optical beam, the electronic detection chain, and the TOI processing pipeline. Scanning beams are an important intermediate product, although they are usually not relevant for astrophysical applications. The effective beam further accounts for the combined effect of the scanning strategy and additional data processing.

Different applications need different levels of accuracy and detail, from the mean full-width at half-maximum (FWHM) of a symmetrical Gaussian description (line *b4*) to an actual point spread function at each specific map location. Beam solid angles are given in line *b1*. Mean ellipticities are given in line *b6*. Lines *b2*, *b3*, and *b7* provide information on the angular response uncertainties and variation across the sky. Our complete uncertainty budget, including covariances of the beam eigenvalues between detectors, in a form which is usable for the power spectra analyses of Planck Collaboration XV (2014), is provided in Planck Collaboration VII (2014).

Sensitivity

The numbers given in line *c1* of Table 4 indicate the rms contribution of the noise per beam solid angle, for the median integration time, as scaled from maps at the full resolution (pixels of 1.7 arcmin). The numbers given in line *c2* of the table also convert this into an rms of the noise in pixels of 1° on a side, again assuming that the rms varies inversely proportional to the pixel scale, as if it were white noise. While convenient to compare the sensitivity of different experiments, this number may be misleading, since it is actually an overestimate of the real noise in the map at the 1° scale.

Table 4. HFI nominal maps − main characteristics.

Quantity							Notes
Reference frequency ν [GHz]	100	143	217	353	545	857	*a1*
Number of bolometers	8	11	12	12	3	4	*a2*
Effective beam solid angle Ω [arcmin^2]	105.78	59.95	28.45	26.71	26.53	24.24	*b1*
Error in solid angle σ_Ω [arcmin^2]	0.55	0.08	0.03	0.02	0.03	0.03	*b2*
Spatial variation (rms) $\Delta\Omega$ [arcmin^2]	0.31	0.25	0.27	0.25	0.34	0.19	*b3*
Effective beam FWHM$_1$ [arcmin]	9.66	7.27	5.01	4.86	4.84	4.63	*b4*
Effective beam FWHM$_2$ [arcmin]	9.65	7.25	4.99	4.82	4.68	4.33	*b5*
Effective beam ellipticity ϵ	1.186	1.036	1.177	1.147	1.161	1.393	*b6*
Variation (rms) of the ellipticity $\Delta\epsilon$	0.023	0.009	0.030	0.028	0.036	0.076	*b7*
Sensitivity per beam solid angle [μK]	10	6	12	39			*c1*
[kJy sr^{-1}]					13	14	*c1*
Sensitivity [μK deg]	1.8	0.8	1.0	3.5			*c2*
[kJy sr^{-1} deg]					1.1	1.1	*c2*
Relative calibration accuracy [%]	$\lesssim$0.2	–	$\lesssim$0.2	$\lesssim$1	$\lesssim$5	$\lesssim$5	*d1*
Absolute calibration accuracy [%]	$\lesssim$0.5	$\lesssim$0.5	$\lesssim$0.5	$\lesssim$1.2	$\lesssim$10	$\lesssim$10	*d2*
Galactic zero-level offset [MJy sr^{-1}]	0.0047	0.0136	0.0384	0.0885	0.1065	0.1470	*e1*
Galactic zero-level uncertainty [MJy sr^{-1}]	0.0008	0.0010	0.0024	0.0067	0.0165	0.0147	*e2*
CIB monopole prediction [MJy sr^{-1}]	0.0030	0.0079	0.033	0.13	0.35	0.64	*e3*

Notes. [a1] Channel map reference frequency, and channel identifier. [a2] Number of bolometers whose data was used in producing the channel map. [b1] Mean value over detectors at the same frequency. See Sect. 5. [b2] As given by simulations. [b3] Variation (rms) of the solid angle across the sky. [b4] FWHM of the Gaussian whose solid angle is equivalent to that of the effective beams. [b5] FWHM of the mean best-fit Gaussian. [b6] Ratio of the major to minor axis of the best-fit Gaussian averaged over the full sky. [b7] Variability (rms) on the sky. [c1] Estimate of the noise per beam solid angle given in *b1*. See Sect. 6.3. [c2] Estimate of the noise scaled to 1° assuming that the noise is white. [d1] Relative calibration accuracy between frequency channels. See Sect. 6. [d2] Calibration uncertainty including the estimated uncertainty of the calibrating source. [e1] Offset to remove at each frequency to set the Galactic zero level. The values quoted correspond to νI_ν = const. At the four lowest frequencies, the conversion factor is about 244, 371, 483, and 287 MJy sr^{-1} K$^{-1}_{\rm CMB}$. [e2] Overall error on the map zero point, for a constant νI_ν spectrum. [e3] According to the Béthermin et al. (2012) model, whose uncertainty is estimated to be at the 20% level. (Also for constant νI_ν.)

It is interesting to note that the sensitivity of the map delivered is comparable to pre-flight predictions (Planck Collaboration 2005), despite the flagging of a significant fraction of data. This decrease of integration time per pixel is approximately compensated by the better-than-required sensitivity of the individual bolometers. A more detailed description of the noise is made available as "half-ring" maps whose differences offer a quite accurate view of the small scale noise, varying by up to half a percent.

Photometric accuracy

The photometric calibration (Sect. 6.2) of the 100 to 353 GHz channels relies on the solar dipole. Comparing the common CMB component at these frequencies shows that the relative accuracy between these channels is better than 0.2% between 100 and 217 GHz, and at the percent level for the 353 GHz channel. For the two highest frequencies, this relative accuracy is at the five percent level (lines *d1*−*d2*). We have also estimated the zero level offset of the maps which needs to be accounted for in Galactic and cosmic infrared background studies (lines *e1*−*e3*).

Spectral response and conversions

The accuracy of the HFI spectral response characterization (Sect. 6.6) is validated using a variety of HFI in-flight observations. Comparisons of Zodiacal light observations (Sect. 6.4) with the bandpass data reveal an out-of-band signal rejection of better than 10^8. The bandpass-based unit conversions and colour corrections were compared against those derived using sky-only data for sources including Sunyaev-Zeldovich (SZ) clusters, dust emission, and CO emission. The SZ observations show agreement with the bandpass data within the quoted uncertainty, as do the 100, 217, and 353 GHz dust coefficient comparisons. The 143 GHz dust coefficient comparison shows differences between the sky and bandpass calibration methods employed; however, the dust component is not dominant at 143 GHz so this discrepancy, although important to understand, does not significantly impact the results. The CO-based dust colour correction coefficients show good agreement with their bandpass-based counterparts, while there are some differences between the bandpass-based and sky-based CO unit conversion coefficients. Investigating these differences continues, and will improve the understanding of the HFI instrument and data; this will in turn lead to better data analysis and improved knowledge of systematic and calibration uncertainties. Details are provided elsewhere, primarily in Planck Collaboration IX (2014) and Planck Collaboration (2013).

Data limitations, validation, and checks for systematic errors

The most powerful top-down tests are the statistics of differences between sky maps. The power spectra of these difference maps have been computed in the same way as those used in the *Planck* CMB likelihood (which are based on the nominal maps). We have applied a large number of such tests, differencing maps made from various detector groups (in/out, left/right), and sky surveys. The sky survey differences maximize the ability

to detect systematic effects potentially affecting a specific detector or detector set; they have been applied to all likelihood inputs. We have found three potentially significant departures at large multipoles, for cross-spectra involving 217 GHz detectors. A jackknife test described in the CMB power spectrum and likelihood paper (Planck Collaboration XV 2014) verified that their removal does not affect significantly the cosmological constraints.

We also found small, microkelvin-level, residuals at low multipoles, which although very significant statistically, are insignificant for a cosmological analysis of the temperature. We have verified through simulations that most of this effect is due to the limitations of the partial correction made for the ADC non-linearity. This limits the accuracy of our dipole calibration to about 0.2% in the CMB channels, and prevents us from using polarization information at low multipoles. However, the data collected at the end of the cryogenic chain will allow a more satisfactory correction for ensuing *Planck* data releases.

Conclusions

The six intensity maps and ancillary information presented above constitute an unprecedented source of information in this frequency range, which is in line with our pre-flight expectations. The level of understanding reached while analysing this data release bodes well for the next release of *Planck* data, which will focus on polarization on all scales, and use nearly twice as much data.

Acknowledgements. The development of *Planck* has been supported by: ESA; CNES and CNRS/INSU-IN2P3-INP (France); ASI, CNR, and INAF (Italy); NASA and DoE (USA); STFC and UKSA (UK); CSIC, MICINN, JA and RES (Spain); Tekes, AoF and CSC (Finland); DLR and MPG (Germany); CSA (Canada); DTU Space (Denmark); SER/SSO (Switzerland); RCN (Norway); SFI (Ireland); FCT/MCTES (Portugal); and PRACE (EU). A description of the *Planck* Collaboration and a list of its members, including the technical or scientific activities in which they have been involved, can be found at http://www.sciops.esa.int/index.php?project=planck&page=Planck_Collaboration.

Appendix A: Yardstick simulations

The Yardstick simulation pipeline has been developed for two main purposes: to quantify the level of residual systematic effects in the maps produced by the HFI DPC; and to validate our correction (or lack thereof) of the data for the systematic effects that we are able to model. The former is achieved by comparing combinations of the data from which the sky signal is expected to vanish with an ensemble of signal and noise realizations of the same combinations of data subsets propagated through the same DPC processing as the data. A mismatch between the two, e.g., in angular power spectrum space, reveals a residual systematic effect in the data. These tests are described in Sect. 7.2. In addition, validating the correction of a given systematic effect requires the implementation of both a model of the effect and its correction (the latter is of course unnecessary if the aim of a test is to justify the absence of a correction). In Sect. 7.2.1, the validation of the non-correction in the data of the ADC non-linearity is an example of such a test. The Yardstick pipeline has been designed in a modular way to allow for both kinds of tests.

For all simulations, the sky signal is taken from the *Planck* sky model (PSM; Delabrouille et al. 2013). This parametric model allows the generation of all-sky temperature and polarization maps of the CMB, the SZ effects, and diffuse Galactic emission (in particular synchrotron, free-free, and thermal dust) with a resolution of a few arcminutes at all *Planck* frequencies. The PSM also includes an extensive point-source catalogue, as well as spinning dust, CO line, and H II region models. From the point of view of data validation, a particularly useful feature of the PSM is its ability to generate random realizations constrained to match observational data within their uncertainties. Although these realizations cannot be fully independent (with the exception of those of the CMB), they do allow for the propagation of some sky modelling uncertainty through the DPC pipeline. The PSM also handles convolution with the spectral response of the HFI bolometers.

The Yardstick pipeline uses the $a_{\ell m}$ spherical harmonic coefficients from the PSM as inputs. After generating the pointing timelines directly from *Planck*'s attitude history file, it feeds both to the LevelS-Core pipeline, software developed jointly by the HFI and LFI teams and documented in the HFI data processing early paper (Planck HFI Core Team 2011b). LevelS-Core returns the beam-convolved signal TOI for each bolometer, which is fed back into the Yardstick pipeline. Noise TOI are generated by a dedicated module and include both white noise and $1/f$ components. The high-frequency component is taken to be the detector noise described in Planck Collaboration VIII (2014), while the $1/f$ noise is modelled following Planck HFI Core Team (2011a). The overall amplitude of the noise is given on a ring-by-ring basis by half-ring map null tests, further discussed in Sect. 7.2.2. The noise model does not include correlations between detectors.

Instrumental effects can be added to the simulated data, each by the addition of a dedicated module to the pipeline. We have used this ability to improve our understanding of pointing and beam issues, as well as to test various aspects of glitch and 4 K line removal, among others. Section 7.2.1 shows an example of the use of the Yardstick simulation facility to evaluate the impact on null-test residuals of the non-correction of the ADC non-linearity. When evaluating the quality of the correction of a systematic effect, we simply apply the relevant TOI processing prior to proceeding with mapmaking. The impact of the transfer function convolution and deconvolution is in any case accounted for.

Finally, TOI are propagated through the DPC mapmaking and calibration pipelines following the procedures described in this paper, including gain correction and application of the various flags (Planck Collaboration VIII 2014). This allows for a one-to-one comparison of the simulated and data maps. Each simulation leads to the generation of per-detector and per-detector-set maps for each survey, and for the nominal mission on which the results in this release are based.

Appendix B: Comparison with a severe selection of data

This appendix describes the selection of pointing periods by more severe criteria and the impact at the map and angular power spectrum levels.

B.1. Data selection

Nominal TOI processing is used; only the selection of rings (i.e., data obtained during a stable pointing period) is changed and described here. The selected rings include only those showing sufficiently stationary noise, within strict bounds. To keep enough data, the full mission is used for this test, not only data from the nominal 15.5 months. We list here the applied criteria.

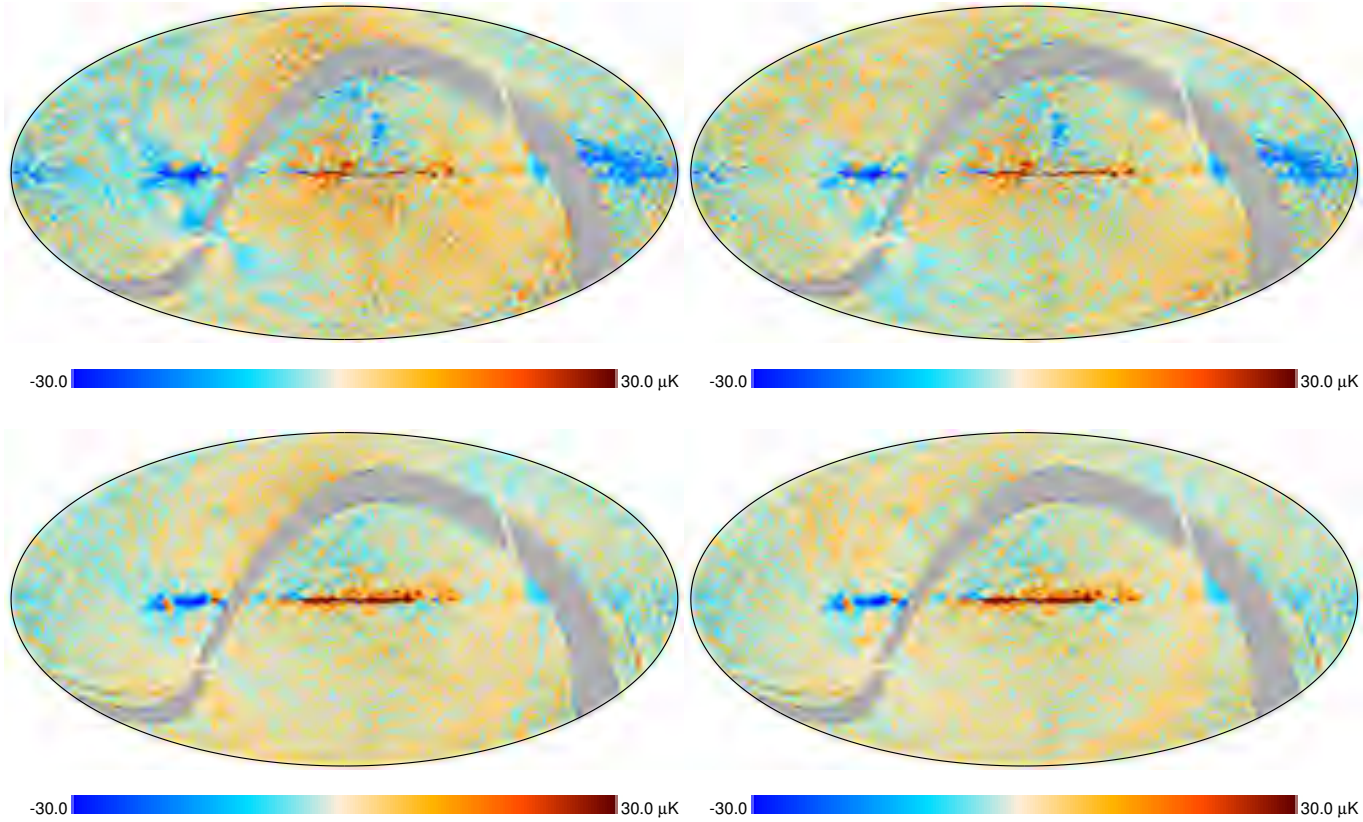

Fig. A.1. *Top*: data difference maps for the 143-1a bolometer. *Bottom*: differences from a simulation including the effect of ADC non-linearity and 4 K lines. *Left column*: Survey 1−Survey 2 differences for maps made without destriping. *Right column*: Survey 1−Survey 2 differences after the destriping used to create the delivered data. The match is sufficiently good that one can use such simulations to estimate the combined effect of the non-linearity of the ADC on the delivered data.

- *Normally discarded rings.* Of course, rings that are already discarded remain so.
- *4 K cooler lines.* Resonant rings are the ones for which a 4 K cooler line (Sect. 3.6) coincides with a harmonic of the spin frequency. The 4 K line correction comes from an interpolation that could introduce some problems. The 10 Hz line is the most troublesome, so we discard all the 10 Hz 4 K line resonant rings. This criterion is common to all detectors.
- *Baseline jump correction.* Rings where a jump correction (Sect. 3.8) was performed are discarded.
- *Bursts in the noise.* Any anomaly in the noise level (as measured by the total noise NET) can be discarded. From Sect. 3.10, these are due to either a baseline drift or a small jump. The basic threshold used here is ±3% of the median noise per ring.
- *Two-level noise.* As described in Planck Collaboration (2013), the following bolometers exhibit a larger than usual noise level in a specific range of rings indicated between brackets:
  - 353-2 – [4994, *end*];
  - 353-3a – [5811, 9057] and [18890, *end*];
  - 143-3a – [9410, *end*]; and
  - 353-5b – [2572, *end*].

  The corresponding ranges are entirely discarded.
- *Integration time per ring.* It is possible that the performance of the deglitching procedure might differ for rings with a significantly smaller integration time than average. Hence we discard rings with an integration time less than 35 min. *This criterion is common to all detectors.*
- *Planets.* Rings including a big planet (i.e., flagged as in Sect. 3.1) can perturb the mapmaking solution if long tails are unseen. *This criterion is common for detectors in the same row of the focal plane.*
- *Medium and small RTS.* All rings known to be affected by RTS (Sect. 3.10) are discarded.
- *Fifth survey.* Survey 5 is fully discarded because of solar flares, unusual integration time and end-of-life operations. *This criterion is common to all detectors.*
- *PSB.* If one of the bolometers of a PSB pair is flagged for a ring, then both bolometers are discarded for that ring.

B.2. Resulting ring statistics

Each criterion has a different impact on both global statistics and those of individual bolometers.

A logical-OR of all of the criteria is shown in Fig. B.1. Black pixels indicate that the corresponding rings of the corresponding bolometer are not used for the severe subset, whereas the red ones are those that were already discarded with the old criteria. Several features are notable, such as differences between the highest and lowest frequency channels, and the fact that some criteria affect all the bolometers.

The global impact of this ring selection is that about 41% of the rings are discarded for the full mission, about 35% for the 100−353 GHz channels, and 45% for 545−857 GHz. With the normal criteria, only about 1% of the rings are discarded for the full mission (0.2% in the nominal mission).

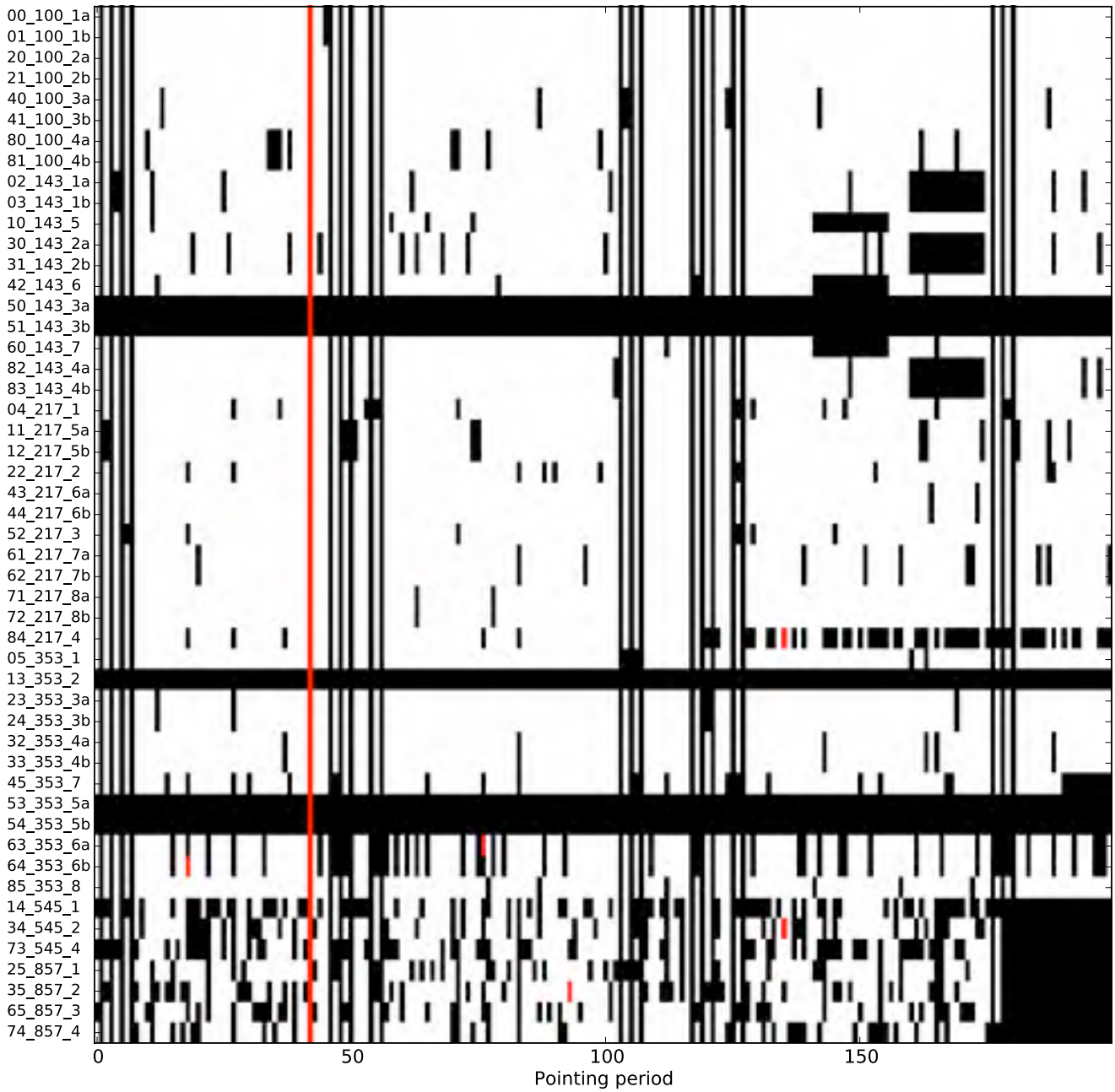

Fig. B.1. Example of normally discarded rings (red) and the severe selection (black) for 201 consecutive pointing periods (the abscissa has an arbitrary offset). The vertical axis gives the individual HFI detector (the first two digits describe the organization of the HFI readout electronics as described in Planck Collaboration 2013).

In order to distinguish the impact of a simple decrease of the observation time and the impact of the use of the severe selection, we check the difference between discarding 35% of the rings with the criteria above, and discarding 35% of the rings randomly for the 143 GHz channel.

B.3. Impact of the severe ring selection on map making

We use the standard pipeline to create maps for each frequency. Along with the global reduction of the number of samples, the severe ring selection will create stripes on the hit-maps, due to the temporal structure of some criteria. The sanity check with the randomly selected rings will have only the impact of the reduction of the hit number. This can be seen in the right column of Fig. B.2: the number of hits in the severe maps is not as homogeneous as in the normal map or the random map but rather looks like the shifted selection map. On the left side, the top panel represents the masked intensity of the normal map, whereas the lower panels correspond to the difference with the severe, random, and shifted maps, respectively. The differences have been whitened with a variance proportional to the inverse of the following effective hit number:

$$n_{\rm eff} = (1 - g) n_{\rm normal},$$

where n is the number of hits of the labelled map and the average ratio of the hit numbers in the severe map to the hit numbers in the normal map is $g = 0.65$ for 100−353 GHz and $g = 0.55$ for 545−857 GHz.

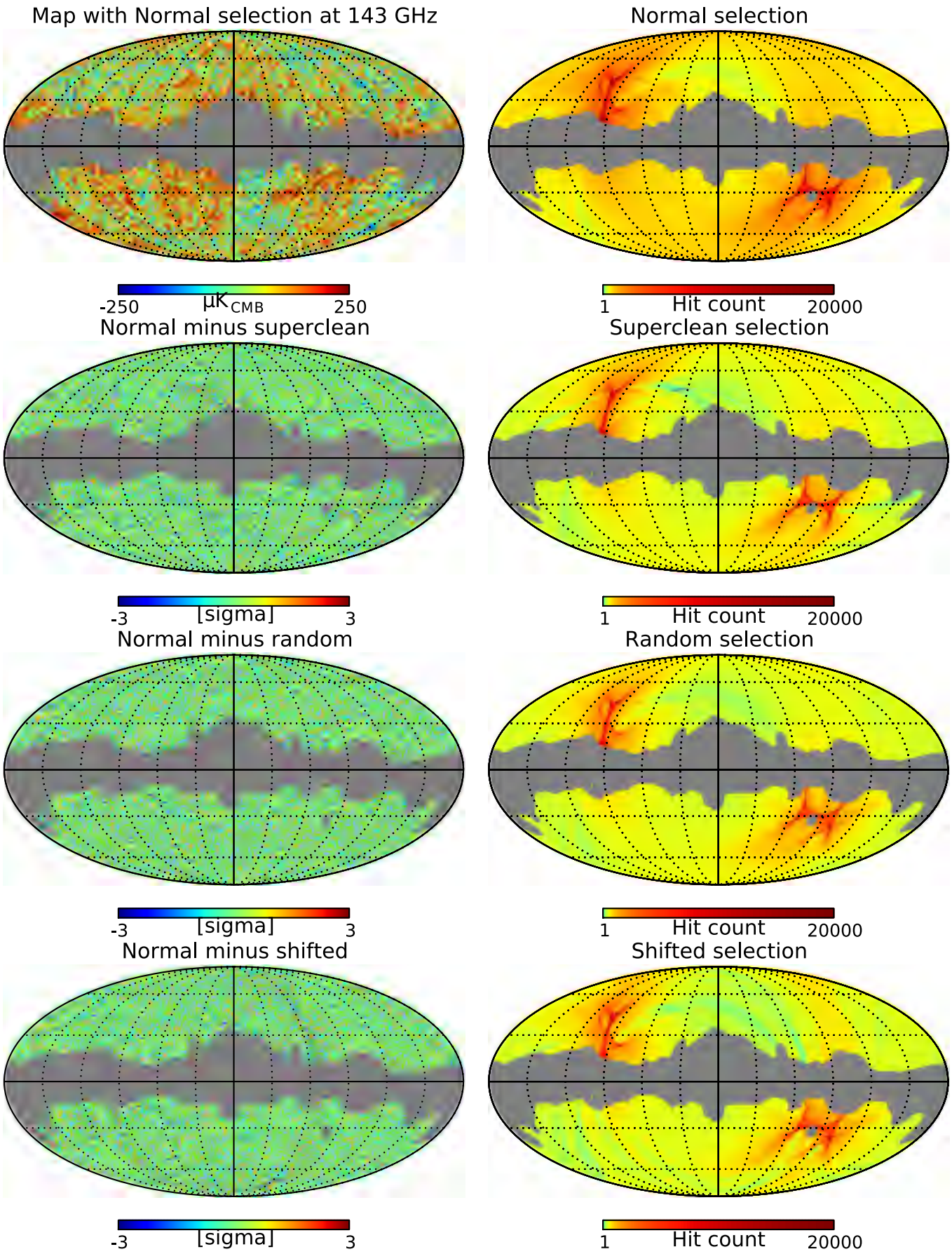

Fig. B.2. *Top panels*: 143 GHz intensity (*left*) and corresponding hit-count map (*right*). *Lower panels*: difference (*left*) between a given selection and normal maps, whitened with the noise calculated from the corresponding hit-count map (*right*), in units of the standard deviation. For the severe selection, striping of the hit numbers is more visible.

B.4. Impact of the severe ring selection on spectra

We then compare the spectra for the severe ring selection and the normal ring selection. We used cross-spectra of offset-corrected half-ring maps, FIRST × LAST. The offset correction is done in order to avoid discrepancies at low-ℓ due to mask leakage. To avoid contamination from the Galaxy, the masks applied to compute these offsets depend on the frequency: $f_{\rm sky}$ = [70,70,40,40,20,20]% for [100,143,217,353,545,857] GHz. Notice that, as the same sky mask is used with the normal and severe maps, the error bars do not include the cosmic variance.

Actually, in the Gaussian case, the expected variance of the difference is induced by noise, and can be computed as:

$$\sigma^2_{\rm expected}\left(C_\ell^{\rm S} - C_\ell^{\rm N}\right) = N_\ell \frac{2C_\ell^{\rm N}\frac{1-g}{g} + N_\ell\frac{1-g^2}{g^2}}{f_{\rm sky}(2\ell+1)}, \quad \text{(B.1)}$$

where $C_\ell^{\rm S}$ is the pseudo-spectrum for the severe selection, $C_\ell^{\rm N}$ is the pseudo-spectrum for the normal selection, N_ℓ is the noise pseudo-spectrum of the normal map. This formula holds if the noise of the individual half-ring maps have the same pseudo-spectrum and are totally uncorrelated, and if the only difference between the normal and the severe selections is the number of hits in them.

This formula does not take into account the exact scanning strategy and its associated geometrical effects. We plot in Fig. B.3 the difference of the two pseudo-spectra, as in Fig. 28, but normalized by the standard deviation expected with Eq. (B.1). Consequently, we would expect in the ideal case the mean to be 0 and the standard deviation to be 1.

The red curve is obviously not compatible with this ideal case. To check if this effect is due to the hit counts on the map or to the content of the rings, two sanity checks consisting of discarding the same number of pointing periods than the severe selection have been performed:

- a selection of randomly discarded pointing periods,
- a selection of discarded pointing periods shifted with respect to the severe one, by adding a constant to the list of discarded rings, modulo the total number of periods. The shifts are large to assess the impact of the fifth survey. Of course, the standard discarded ring list is still taken into account. We show in Fig. B.5 three examples of these selections which can be compared to the normal and the severe ones.

All the selections have the same number of discarded rings, but a different impact on the scanning strategy. The difference between the three realizations is driven by the absence or the presence of large stripes on the hit count maps, and depends on the shift.

As can be seen in Fig. B.2, the random selection has fewer stripes than the shifted one in the hit count map, so we expect smaller deviations at low ℓ for this selection. This is due to the large chunk of consecutive discarded rings in the severe selection. One can see in Fig. B.3 that the effects affecting the severe selection (the tilt in the mean, and the increase of dispersion at low ℓ) are also present at different levels in the sanity checks.

The difference between the severe and the normal selection cannot be cast into just a global coefficient $g = 1-0.35$, but the sanity check with shifted selections reproduce the observed bias well especially when the shift is by 15 000 rings which corresponds to about one year. Therefore the small features and the global slope of the difference between the normal and severe spectra can be attributed to the structure of the hit maps (directly linked to the scanning strategy) rather than to the content of the signal maps.

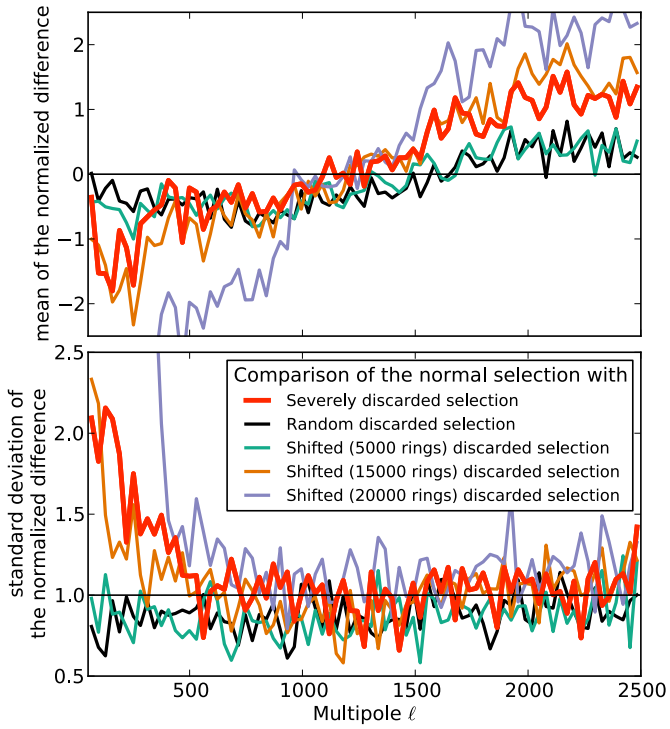

Fig. B.3. Binned difference between the severe and the normal pseudo-spectra at 143 GHz in units of the expected standard deviation. If our assumptions are correct, the residual noise has a Gaussian distribution centred on zero with a variance of one. The *top and bottom panels* represents the mean and standard deviation of the difference in bins of 31 samples, obtained from the data in Fig. 28. The black points represent a sanity check where the rings have been discarded randomly, and the blue, orange and green lines represent three sanity checks where the selection of discarded rings has been shifted with respect to the severe one.

Figure B.4 shows those normalized differences for all of the channels. The difference is plotted in units of $\sigma_{\rm expected}(C_\ell^S - C_\ell^N)$, so that the expected error bars are 0 ± 1. This is the case from $\ell = 500$ to $\ell = 2500$ for all frequencies. The rise at 143 and 217 GHz is as discussed in Fig. B.3.

The maps are thus fully compatible, and no effect of non-stationarity of the noise in the timelines (for instance) has been detected. The normal selection can be used safely to extract science from the frequency maps.

Appendix C: Additional tests at 217 GHz from full mission survey data

We denote the combined detector maps produced for Sky Survey 1, Sky Survey 2, etc., as S1, S2, S3, S4. Here we consider additional tests allowed using the full S3 and S4 surveys, i.e., using some data collected after the end of the nominal mission (and processed with the same pipeline). The 2013 likelihood is based on cross-spectra between detector-set maps (or detsets) to eliminate possible biases from inaccurate instrument noise determinations. At 217 GHz, we use six temperature maps from the available detsets over the nominal mission duration. One could have computed cross-survey spectra, for example S1 × S2; however, one then pays a substantial penalty in signal-to-noise ratio,

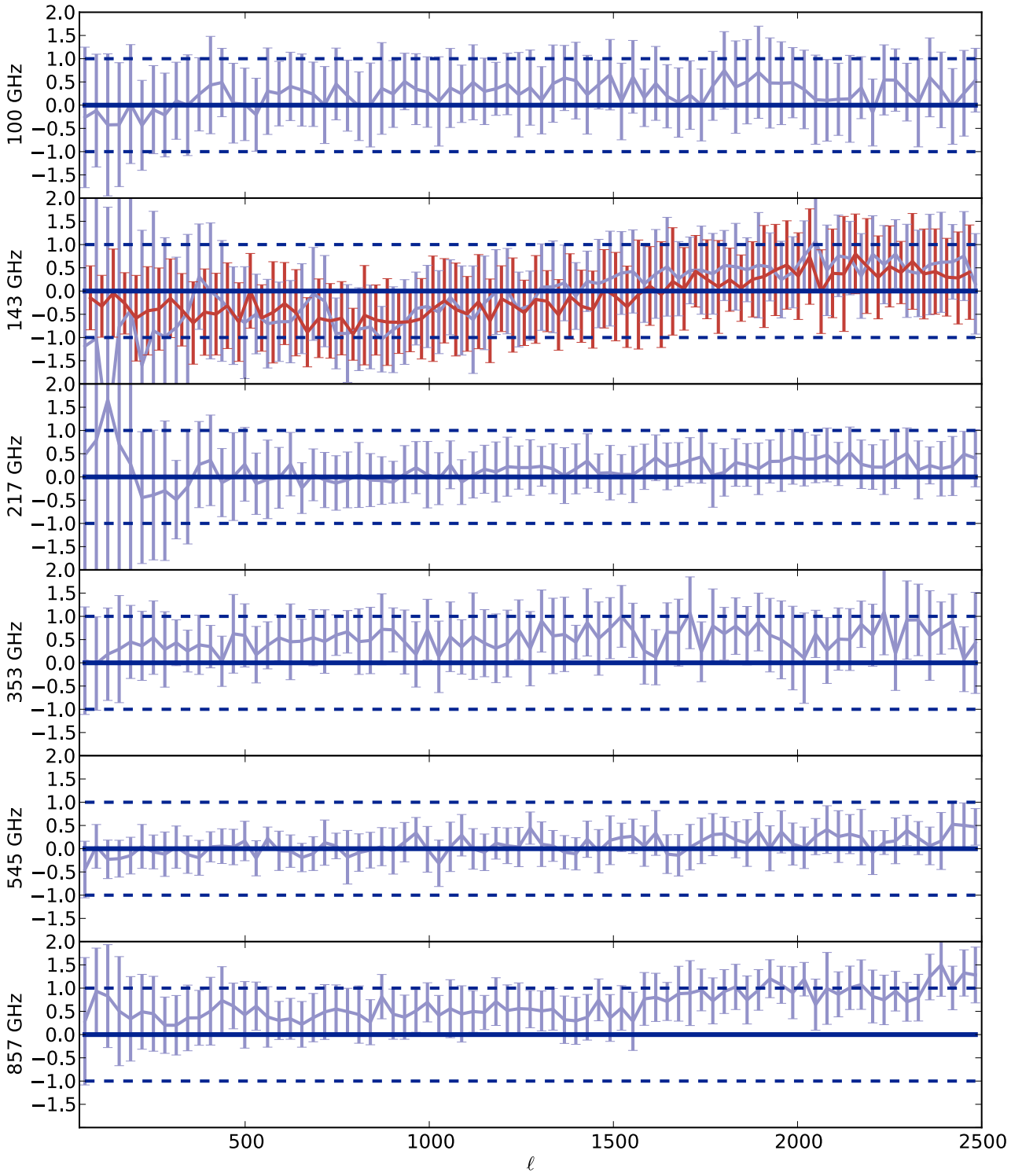

Fig. B.4. For each of the HFI channels, the difference of the normal spectrum and the spectrum obtained with a more severe selection of rings, is shown in units of the expected standard deviation. If our assumptions are correct, the residual noise is supposed to have a Gaussian distribution centred on zero with a dispersion of one. The red points for the 143 GHz correspond to a sanity check with a random discarding of rings as discussed in Fig. B.3 (the points here are band-averaged in bins of width $\Delta\ell \sim 31$).

since half the data are effectively discarded. Furthermore, since each individual survey does not cover the complete sky, S1 and S2 contain non-identical missing areas of sky, leading to irregularly shaped sky masks. In the *Planck* likelihood code released in 2013, we cross-correlated detset maps (excluding auto-spectra). This has the advantage of retaining almost all of the information in the *Planck* data, but has the disadvantage of susceptibility to biases caused by correlated systematics between detectors observing the sky at the same time. One therefore has to make a choice between analysing cross-survey spectra, with associated loss of signal-to-noise ratio, or analysing detset cross-spectra with potentially greater susceptibility to systematics. Of course,

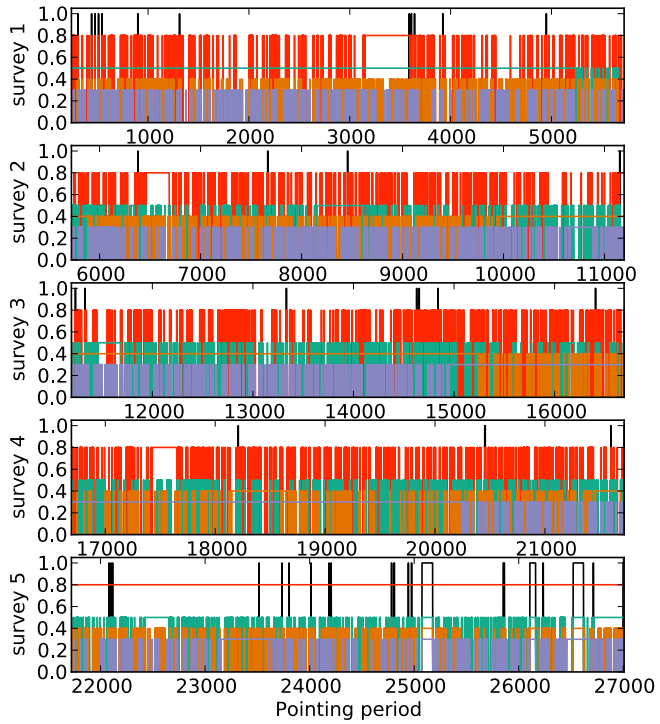

Fig. B.5. Selection of rings for one 143 GHz bolometer, for the normal selection (in black, value 1.0 if discarded), the severe selection (in red, 0.8 if discarded), three shifted selections (in blue, orange and green, respectively 0.3, 0.4, 0.5 if discarded). Each panel represents a survey. The color code for the shifted selections is the same as in Fig. B.3.

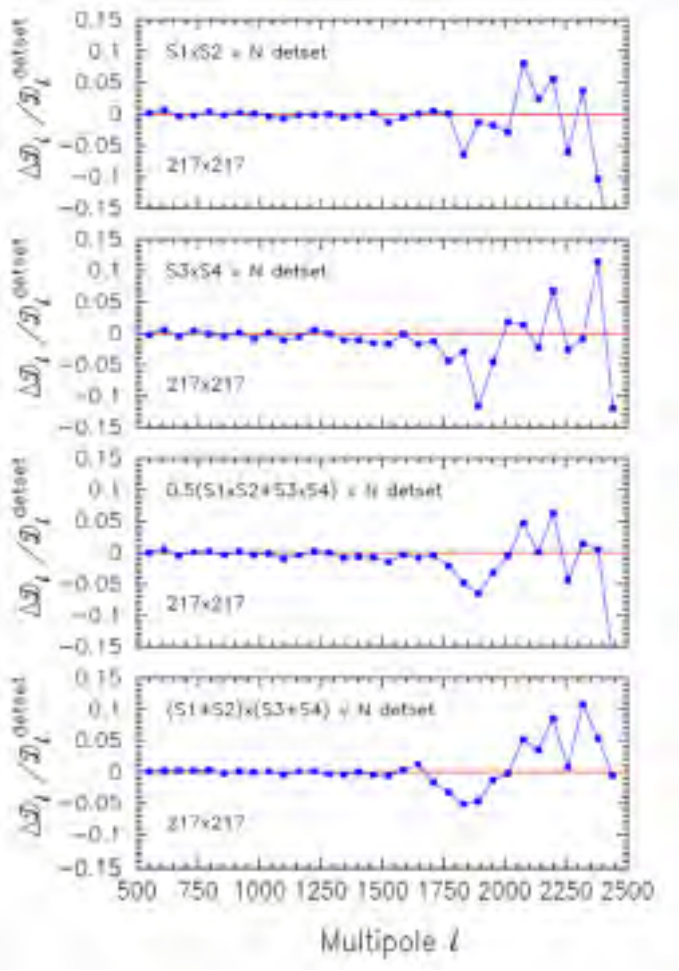

Fig. C.1. Differences between the 217 × 217 nominal mission detset spectrum (N) and various cross-survey spectra, as labeled. Clearly the detset and cross-survey spectra are in very good agreement. Any co-temporal systematics are extremely small.

if systematics can be controlled to a sufficiently low level, then the detset approach is the more powerful.

From each of the 217 GHz survey maps, we compute the following cross-spectra S1 × S2, S3 × S4, 0.5(S1 × S2 + S3 × S4) and (S1 + S2) × (S3 + S4). The sky masks are the same as the 217 GHz mask used in the 2013 Planck likelihood, with identical point source masks. The masks for S1 × S2 and S3 × S4 differ in that we exclude missing sky area and any pixels observed only in one sky survey. The yearly cross-survey spectra (S1 + S2) × (S3 + S4) have higher signal-to-noise ratio than either S1 × S2 or S3 × S4, and have the added advantage that we can use almost identical masks to those used for the detset spectra, thus eliminating cosmic variance in a comparison of spectra.

The four panels in Fig. C.1 show the differences between the 217 × 217 nominal mission detset spectrum and various cross-survey spectra. No corrections for Galactic dust emission or unresolved foregrounds have been made to the spectra. Since the masks are similar (almost identical in the case of (S1 + S2) × (S3 + S4)), the spectra are highly correlated in the signal-dominated regime. There is therefore a characteristic scale in this type of plot set by the onset of instrument noise. Over the multipole range where the spectra are signal-dominated, the scatter is small (much less than the cosmic variance). In the top two plots, the scatter abruptly increases at multipoles ∼1800 because of the high noise in the S1×S2 and S3×S4 spectra. The first panel shows hints of a deficit at multipoles around 1800, and perhaps a slight excess at multipoles of 2000. The S3 × S4 comparison shows further evidence of a deficit at $\ell \sim 1800$. The yearly cross-survey spectra, which have the highest signal-to-noise ratio of the cross-survey spectra, show clear evidence of a deficit at $\ell \sim 1800$, and evidence for an excess at $\ell > 2000$. As already mentioned, the dip at $\ell \sim 1800$ is caused by electromagnetic interference between the Joule-Thomson 4 K cooler electronics and the bolometer readout electronics. This interference leads to a set of time-variable narrow lines in the time-ordered data. The data processing pipeline applies a filter to remove these lines; however, the filtering failed to reduce the impact of these lines to negligible levels. Incomplete removal of the 4 K cooler lines affects primarily the 217 PSB × PSB cross-spectrum in Survey 1. At the time of submission of the 2013 *Planck* papers, we had not established clear evidence that the $\ell = 1800$ feature was a residual of the low level data processing. The impact of this systematic in the 217×217 spectrum was analysed in the revised versions of Planck Collaboration XVI (2014) (Appendix C.4), and was demonstrated to have little impact on cosmological parameter determination. But it does contributes to the weak detection of a feature in the power spectrum reconstruction done in Planck Collaboration XXII (2014).

The small excess at $\ell > 2000$ is caused by low levels of correlated noise between the 217 GHz bolometers, and is strongest in a subset of the SWB×SWB spectra. The amplitude of the correlated noise implied by the fourth panel of Fig. C.1 is compatible with results discussed in Planck Collaboration XV (2014), where it is found that the impact on cosmological parameters of this effect is negligible, with less than a 0.1σ variation on the mean posterior values.

Finally, we constructed a full mission likelihood (denoted F) based on the detset spectra, using sky masks identical to those used in the publicly-distributed likelihood. The impact of systematics in these full mission likelihoods should be substantially smaller than in the nominal mission likelihood. In particular, we verified that the $\ell = 1800$ 4 K line residual is strongly diluted in the full mission data. We find that the values of the parameters of the base ΛCDM cosmology determined from the publicly released nominal mission detset likelihood (N) and the full mission detset likelihood with the same sky coverage (F) are completely compatible. For example, $\Omega_c h^2$ varies from 0.1199 ± 0.0027 (N) to 0.1196 ± 0.0025 (F), σ_8 is completely unchanged till the third decimal place, and the value of H_0 for the nominal mission, $67.3 \pm 1.2\,\mathrm{km\,s^{-1}\,Mpc^{-1}}$ becomes $67.6 \pm 1.1\,\mathrm{km\,s^{-1}\,Mpc^{-1}}$ for the full mission, everything else being equal.

References

Beichman, C. A., Neugebauer, G., Habing, H. J., Clegg, P. E., & Chester, T. J. 1988, Infrared astronomical satellite (IRAS) catalogs and atlases, 1: Explanatory supplement, 1
Béthermin, M., Daddi, E., Magdis, G., et al. 2012, ApJ, 757, L23
Catalano, A., Coulais, A., & Lamarre, J.-M. 2010, Appl. Opt., 49, 5938
Chamberlin, A. B., Yeomans, D. K., Chodas, P. W., et al. 1997, BAAS, 29, 2106
Delabrouille, J., Betoule, M., Melin, J.-B., et al. 2013, A&A, 553, A96
Dupac, X., & Tauber, J. 2005, A&A, 430, 363
Górski, K. M., Hivon, E., Banday, A. J., et al. 2005, ApJ, 622, 759
Hivon, E., Górski, K. M., Netterfield, C. B., et al. 2002, ApJ, 567, 2
Huffenberger, K. M., Crill, B. P., Lange, A. E., Górski, K. M., & Lawrence, C. R. 2010, A&A, 510, A58
Kelsall, T., Weiland, J. L., Franz, B. A., et al. 1998, ApJ, 508, 44
Lamarre, J., Puget, J., Ade, P. A. R., et al. 2010, A&A, 520, A9
Liang, Z., Fixsen, D. J., & Gold, B. 2012, [arXiv:astro-ph/1201.0060]
Mitra, S., Rocha, G., Górski, K. M., et al. 2011, ApJS, 193, 5
Moreno, R. 2010, Neptune and Uranus planetary brightness temperature tabulation. Tech. Rep., ESA Herschel Science Center, available from ftp://ftp.sciops.esa.int/pub/hsc-calibration/PlanetaryModels/ESA2
Planck Collaboration. 2005, ESA publication ESA-SCI(2005)/01
Planck Collaboration I. 2011, A&A, 536, A1
Planck Collaboration II. 2011, A&A, 536, A2
Planck Collaboration VII. 2011, A&A, 536, A7
Planck Collaboration 2013, The Explanatory Supplement to the Planck 2013 results, http://www.sciops.esa.int/wikiSI/planckpla/index.php?title=Main_Page (ESA)
Planck Collaboration I. 2014, A&A, 571, A1
Planck Collaboration II. 2014, A&A, 571, A2
Planck Collaboration III. 2014, A&A, 571, A3
Planck Collaboration IV. 2014, A&A, 571, A4
Planck Collaboration V. 2014, A&A, 571, A5
Planck Collaboration VI. 2014, A&A, 571, A6
Planck Collaboration VII. 2014, A&A, 571, A7
Planck Collaboration VIII. 2014, A&A, 571, A8
Planck Collaboration IX. 2014, A&A, 571, A9
Planck Collaboration X. 2014, A&A, 571, A10
Planck Collaboration XI. 2014, A&A, 571, A11
Planck Collaboration XII. 2014, A&A, 571, A12
Planck Collaboration XIII. 2014, A&A, 571, A13
Planck Collaboration XIV. 2014, A&A, 571, A14
Planck Collaboration XV. 2014, A&A, 571, A15
Planck Collaboration XVI. 2014, A&A, 571, A16
Planck Collaboration XVII. 2014, A&A, 571, A17
Planck Collaboration XVIII. 2014, A&A, 571, A18
Planck Collaboration XIX. 2014, A&A, 571, A19
Planck Collaboration XX. 2014, A&A, 571, A20
Planck Collaboration XXI. 2014, A&A, 571, A21
Planck Collaboration XXII. 2014, A&A, 571, A22
Planck Collaboration XXIII. 2014, A&A, 571, A23
Planck Collaboration XXIV. 2014, A&A, 571, A24
Planck Collaboration XXV. 2014, A&A, 571, A25
Planck Collaboration XXVI. 2014, A&A, 571, A26
Planck Collaboration XXVII. 2014, A&A, 571, A27
Planck Collaboration XXVIII. 2014, A&A, 571, A28
Planck Collaboration XXIX. 2014, A&A, 571, A29
Planck Collaboration XXX. 2014, A&A, 571, A30
Planck Collaboration XXXI. 2014, A&A, 571, A31
Planck HFI Core Team 2011a, A&A, 536, A4
Planck HFI Core Team 2011b, A&A, 536, A6
Rosset, C., Tristram, M., Ponthieu, N., et al. 2010, A&A, 520, A13
Ruze, J. 1966, IEEE Proc., 54, 633
Rybicki, G. B., & Lightman, A. P. 1986, Radiative Processes in Astrophysics (Wiley VCH)
Spergel, D., Flauger, R., & Hlozek, R. 2013 [arXiv:1312.3313]
Szapudi, I., Prunet, S., & Colombi, S. 2001, ApJ, 561, L11
Tauber, J. A., Mandolesi, N., Puget, J., et al. 2010, A&A, 520, A1
Tristram, M., Filliard, C., Perdereau, O., et al. 2011, A&A, 534, A88

[1] APC, AstroParticule et Cosmologie, Université Paris Diderot, CNRS/IN2P3, CEA/lrfu, Observatoire de Paris, Sorbonne Paris Cité, 10 rue Alice Domon et Léonie Duquet, 75205 Paris Cedex 13, France
[2] Aalto University Metsähovi Radio Observatory, Metsähovintie 114, 02540 Kylmälä, Finland
[3] African Institute for Mathematical Sciences, 6-8 Melrose Road, 7945 Muizenberg, Cape Town, South Africa
[4] Agenzia Spaziale Italiana Science Data Center, via del Politecnico snc, 00133 Roma, Italy
[5] Agenzia Spaziale Italiana, Viale Liegi 26, Roma, Italy
[6] Astrophysics Group, Cavendish Laboratory, University of Cambridge, J J Thomson Avenue, Cambridge CB3 0HE, UK
[7] Astrophysics & Cosmology Research Unit, School of Mathematics, Statistics & Computer Science, University of KwaZulu-Natal, Westville Campus, Private Bag X54001, 4000 Durban, South Africa
[8] Atacama Large Millimeter/submillimeter Array, ALMA Santiago Central Offices, Alonso de Cordova 3107, Vitacura, Casilla 763 0355 Santiago, Chile
[9] CITA, University of Toronto, 60 St. George St., Toronto, ON M5S 3H8, Canada
[10] CNRS, IRAP, 9 Av. colonel Roche, BP 44346, 31028 Toulouse Cedex 4, France
[11] California Institute of Technology, Pasadena, California, USA
[12] Centre for Theoretical Cosmology, DAMTP, University of Cambridge, Wilberforce Road, Cambridge CB3 0WA, UK
[13] Centro de Estudios de Física del Cosmos de Aragón (CEFCA), Plaza San Juan 1, planta 2, 44001 Teruel, Spain
[14] Computational Cosmology Center, Lawrence Berkeley National Laboratory, Berkeley, California, USA
[15] Consejo Superior de Investigaciones Científicas (CSIC), 28006 Madrid, Spain
[16] DSM/Irfu/SPP, CEA-Saclay, 91191 Gif-sur-Yvette Cedex, France
[17] DTU Space, National Space Institute, Technical University of Denmark, Elektrovej 327, 2800 Kgs. Lyngby, Denmark
[18] Département de Physique Théorique, Université de Genève, 24 Quai E. Ansermet,1211 Genève 4, Switzerland
[19] Departamento de Física Fundamental, Facultad de Ciencias, Universidad de Salamanca, 37008 Salamanca, Spain
[20] Department of Astronomy and Astrophysics, University of Toronto, 50 Saint George Street, Toronto, Ontario, Canada
[21] Department of Astrophysics/IMAPP, Radboud University Nijmegen, PO Box 9010, 6500 GL Nijmegen, The Netherlands
[22] Department of Electrical Engineering and Computer Sciences, University of California, Berkeley, California, USA
[23] Department of Physics & Astronomy, University of British Columbia, 6224 Agricultural Road, Vancouver, British Columbia, Canada
[24] Department of Physics and Astronomy, Dana and David Dornsife College of Letter, Arts and Sciences, University of Southern California, Los Angeles, CA 90089, USA
[25] Department of Physics and Astronomy, University College London, London WC1E 6BT, UK
[26] Department of Physics, Florida State University, Keen Physics Building, 77 Chieftan Way, Tallahassee, Florida, USA

[27] Department of Physics, Gustaf Hällströmin katu 2a, University of Helsinki, 00014 Helsinki, Finland
[28] Department of Physics, Princeton University, Princeton, New Jersey, USA
[29] Department of Physics, University of California, One Shields Avenue, Davis, California, USA
[30] Department of Physics, University of California, Santa Barbara, California, USA
[31] Department of Physics, University of Illinois at Urbana-Champaign, 1110 West Green Street, Urbana, Illinois, USA
[32] Dipartimento di Fisica e Astronomia G. Galilei, Università degli Studi di Padova, via Marzolo 8, 35131 Padova, Italy
[33] Dipartimento di Fisica e Scienze della Terra, Università di Ferrara, via Saragat 1, 44122 Ferrara, Italy
[34] Dipartimento di Fisica, Università La Sapienza, P.le A. Moro 2, 00185 Roma, Italy
[35] Dipartimento di Fisica, Università degli Studi di Milano, via Celoria, 16, 20133 Milano, Italy
[36] Dipartimento di Fisica, Università degli Studi di Trieste, via A. Valerio 2, 34127 Trieste, Italy
[37] Dipartimento di Fisica, Università di Roma Tor Vergata, via della Ricerca Scientifica 1, 00133 Roma, Italy
[38] Discovery Center, Niels Bohr Institute, Blegdamsvej 17, Copenhagen, Denmark
[39] Dpto. Astrofísica, Universidad de La Laguna (ULL), 38206 La Laguna, Tenerife, Spain
[40] European Southern Observatory, ESO Vitacura, Alonso de Cordova 3107, Vitacura, Casilla 19001 Santiago, Chile
[41] European Space Agency, ESAC, Planck Science Office, Camino bajo del Castillo s/n, Urbanización Villafranca del Castillo, Villanueva de la Cañada, 28692 Madrid, Spain
[42] European Space Agency, ESTEC, Keplerlaan 1, 2201 AZ Noordwijk, The Netherlands
[43] Helsinki Institute of Physics, Gustaf Hällströmin katu 2, University of Helsinki, 00014 Helsinki, Finland
[44] INAF − Osservatorio Astrofisico di Catania, via S. Sofia 78, Catania, Italy
[45] INAF − Osservatorio Astronomico di Padova, Vicolo dell'Osservatorio 5, 35122 Padova, Italy
[46] INAF − Osservatorio Astronomico di Roma, via di Frascati 33, 00040 Monte Porzio Catone, Italy
[47] INAF − Osservatorio Astronomico di Trieste, via G.B. Tiepolo 11, Trieste, Italy
[48] INAF Istituto di Radioastronomia, via P. Gobetti 101, 40129 Bologna, Italy
[49] INAF/IASF Bologna, via Gobetti 101, 40129 Bologna, Italy
[50] INAF/IASF Milano, via E. Bassini 15, 20133 Milano, Italy
[51] INFN, Sezione di Bologna, via Irnerio 46, 40126 Bologna, Italy
[52] INFN, Sezione di Roma 1, Università di Roma Sapienza, Piazzale Aldo Moro 2, 00185 Roma, Italy
[53] IPAG: Institut de Planétologie et d'Astrophysique de Grenoble, Université Joseph Fourier, Grenoble 1/CNRS-INSU, UMR 5274, 38041 Grenoble, France
[54] IUCAA, Post Bag 4, Ganeshkhind, Pune University Campus, 411 007 Pune, India
[55] Imperial College London, Astrophysics group, Blackett Laboratory, Prince Consort Road, London, SW7 2AZ, UK
[56] Infrared Processing and Analysis Center, California Institute of Technology, Pasadena, CA 91125, USA
[57] Institut Néel, CNRS, Université Joseph Fourier Grenoble I, 25 rue des Martyrs, 38042 Grenoble, France
[58] Institut Universitaire de France, 103 Bd Saint-Michel, 75005 Paris, France
[59] Institut d'Astrophysique Spatiale, CNRS (UMR8617) Université Paris-Sud 11, Bâtiment 121, 91405 Orsay, France
[60] Institut d'Astrophysique de Paris, CNRS (UMR7095), 98bis Boulevard Arago, 75014 Paris, France
[61] Institute for Space Sciences, Bucharest-Magurale, Romania
[62] Institute of Astro and Particle Physics, Technikerstrasse 25/8, University of Innsbruck, 6020 Innsbruck, Austria
[63] Institute of Astronomy and Astrophysics, Academia Sinica, 10617 Taipei, Taiwan
[64] Institute of Astronomy, University of Cambridge, Madingley Road, Cambridge CB3 0HA, UK
[65] Institute of Theoretical Astrophysics, University of Oslo, 0315 Blindern, Oslo, Norway
[66] Instituto de Astrofísica de Canarias, C/Vía Láctea s/n, 38205 La Laguna, Tenerife, Spain
[67] Instituto de Física de Cantabria (CSIC-Universidad de Cantabria), Avda. de los Castros s/n, 39005 Santander, Spain
[68] Jet Propulsion Laboratory, California Institute of Technology, 4800 Oak Grove Drive, Pasadena, California, USA
[69] Jodrell Bank Centre for Astrophysics, Alan Turing Building, School of Physics and Astronomy, The University of Manchester, Oxford Road, Manchester, M13 9PL, UK
[70] Kavli Institute for Cosmology Cambridge, Madingley Road, Cambridge, CB3 0HA, UK
[71] LAL, Université Paris-Sud, CNRS/IN2P3, 91405 Orsay, France
[72] LERMA, CNRS, Observatoire de Paris, 61 Avenue de l'Observatoire, 75014 Paris, France
[73] Laboratoire AIM, IRFU/Service d'Astrophysique − CEA/DSM − CNRS − Université Paris Diderot, Bât. 709, CEA-Saclay, 91191 Gif-sur-Yvette Cedex, France
[74] Laboratoire Traitement et Communication de l'Information, CNRS (UMR 5141) and Télécom ParisTech, 46 rue Barrault, 75634 Paris Cedex 13, France
[75] Laboratoire de Physique Subatomique et de Cosmologie, Université Joseph Fourier Grenoble I, CNRS/IN2P3, Institut National Polytechnique de Grenoble, 53 rue des Martyrs, 38026 Grenoble Cedex, France
[76] Laboratoire de Physique Théorique, Université Paris-Sud 11 & CNRS, Bâtiment 210, 91405 Orsay, France
[77] Lawrence Berkeley National Laboratory, Berkeley, California, USA
[78] Max-Planck-Institut für Astrophysik, Karl-Schwarzschild-Str. 1, 85741 Garching, Germany
[79] McGill Physics, Ernest Rutherford Physics Building, McGill University, 3600 rue University, Montréal, QC, H3A 2T8, Canada
[80] National University of Ireland, Department of Experimental Physics, Maynooth, Co. Kildare, Ireland
[81] Niels Bohr Institute, Blegdamsvej 17, 2100 Copenhagen, Denmark
[82] Observational Cosmology, Mail Stop 367-17, California Institute of Technology, Pasadena, CA, 91125, USA
[83] Optical Science Laboratory, University College London, Gower Street, London, UK
[84] SB-ITP-LPPC, EPFL, 1015, Lausanne, Switzerland
[85] SISSA, Astrophysics Sector, via Bonomea 265, 34136 Trieste, Italy
[86] School of Physics and Astronomy, Cardiff University, Queens Buildings, The Parade, Cardiff, CF24 3AA, UK
[87] Space Sciences Laboratory, University of California, Berkeley, California, USA
[88] Special Astrophysical Observatory, Russian Academy of Sciences, Nizhnij Arkhyz, Zelenchukskiy region, 369167 Karachai-Cherkessian Republic, Russia
[89] Stanford University, Dept of Physics, Varian Physics Bldg, 382 via Pueblo Mall, Stanford, California, USA
[90] Sub-Department of Astrophysics, University of Oxford, Keble Road, Oxford OX1 3RH, UK
[91] Theory Division, PH-TH, CERN, 1211, Geneva 23, Switzerland
[92] UPMC Univ Paris 06, UMR7095, 98bis Boulevard Arago, 75014 Paris, France
[93] Université de Toulouse, UPS-OMP, IRAP, 31028 Toulouse Cedex 4, France
[94] Universities Space Research Association, Stratospheric Observatory for Infrared Astronomy, MS 232-11, Moffett Field, CA 94035, USA
[95] University of Granada, Departamento de Física Teórica y del Cosmos, Facultad de Ciencias, 18071 Granada, Spain
[96] Warsaw University Observatory, Aleje Ujazdowskie 4, 00-478 Warszawa, Poland